NNT : 2016SACLX103

Thèse de doctorat
de
L'Université Paris-Saclay
préparée à
"L'Ecole Polytechnique"

Ecole Doctorale n° 573
Interfaces : approches interdisciplinaires, fondements, applications et innovation

Spécialité de doctorat : Chimie

Par

M. Timothy Aschl

Biochips based on silicon for detecting the interaction between aptamers and pathogens

Soutenance de thèse à Palaiseau, le 13 décembre 2016.

Composition du Jury :

Mme. Hafsa Korri-Youssoufi	Directeur de recherche, Université Paris-Sud	Présidente
M. Rabah Boukherroub	Directeur de recherche, Université Lille 1	Rapporteur
M. Jean-Louis Marty	Professeur, Université de Perpignan	Rapporteur
M. François Ozanam	Directeur de recherche, Ecole Polytechnique	Examinateur
Mme. Rosemarie Sauvage	Responsable du domaine scientifique nanotechnologies, DGA	Examinatrice
Mme. Anne Chantal Gouget-Laemmel	Chargée de recherche, Ecole Polytechnique	Directrice de thèse

Acknowledgments

Ce travail de thèse a été réalisé au laboratoire de Physique de la Matière Condensée (PMC), à l'École Polytechnique cofinancé par la Direction générale de l'Armement (DGA).

Je veux remercier d'abord les membres du jury qui ont accepté d'évaluer ce travail de thèse. Tout d'abord, je souhaite exprimer toute ma gratitude à Hafsa Korri-Youssoufi présidente du jury. J'adresse ensuite mes remerciements aux rapporteurs, Jean-Louis Marty et Rabah Boukherroub qui ont lu l'ensemble de ce manuscrit avec beaucoup d'attention. Merci enfin à Rosemarie Sauvage de la DGA pour son soutien pendant ce travail.

Je souhaite exprimer toute ma gratitude à ma directrice de thèse, Anne-Chantal Gouget, qui a dirigé ce travail et a été présente tout au long de ces trois années de thèse. Je la remercie vivement pour sa disponibilité, pour le temps qu'elle a consacré à mes sollicitations, et pour les discussions « manips » quotidiennes. J'ai beaucoup apprécié l'autonomie qu'elle m'a laissé dans la réalisation de mes expériences. C'est grâce à elle que ce travail a pu aboutir.

J'adresse aussi mes remerciements à mon co-directeur de thèse, Philippe Allongue. Au-delà de sa rigueur et de sa disponibilité, je lui suis reconnaissant de m'avoir fait profiter de ses compétences scientifiques. Sur ce point, je lui suis particulièrement reconnaissant pour ses idées et conseils pendant la rédaction du manuscrit et la préparation de soutenance.

Il est tout particulièrement important pour moi de remercier Anne-Chantal et Philippe pour leurs nombreuses relectures du manuscrit, afin de le rendre à la fois bien structuré, clair et compréhensible

François Ozanam, grâce à ses conseils et sa disponibilité, a également contribué largement à l'obtention et l'interprétation des résutats présentés ici. Je le remercie de m'avoir transmis sa passion pour la science, ainsi que certaines de ses nombreuses connaissances.

Je remercie aussi Gilles Frison de LCM, qui a lancé des calculs DFT pour l'analyse des spectres infrarouges, en dernière minute. Ses calculs ont énormément apporté à l'analyse des résultats.

Lucio Martinelli et Fouad Maroun ont également contribué au succès de cette thèse. Leurs idées, propositions et coup de mains ont souvent aidé à résoudre efficacement les problèmes qui ont régulièrement ponctués cette recherche.

Pendant la thèse j'ai partagé le bureau et plein de fou-rires avec Denis, Khalid et Patrice. Je les remercie très sincèrement pour leur bonne humeur / humour pendant le temps que l'on a passé ensemble. Toujours quelques mots gentils ou des petites blagues… on s'est bien amusé dans ce bureau. J'espère que vous allez rester la bonne équipe que vous êtes et aussi que vous aurez quelqu'un de sympa à ma place.

Je tiens à remercier très chaleureusement Anne Moraillon, sans elle cette thèse n'aurait pas été possible. C'est par elle que j'ai appris tous les détails du travail quotidien de laboratoire, notamment en passant de longues heures à m'indiquer comment faire telles ou telles. Je lui adresse un grand merci pour tous les moments de bonne humeur et d'enthousiasme que nous avons partagés. Elle est devenue une vraie amie, je ne la remercierai jamais assez pour tous les bons moments passés ensemble.

Je souhaite aussi de remercier tous les amis que j'ai eu la plaisir de rencontrer pendant ma thèse à l'X. C'est surtout grâce à leur soutien que j'ai pu réussir. Notamment je remercie pour notre amitié : Lucie Devys pour sa gentillesse ; Maxime Ardre pour son esprit ouvert et sa mentalité de « let's do it » ; Samuel Thomas, Pierre Nocerino et Léa Mazé pour les diners, soirées de jeux et des conversations excellentes ; Alizée Dubois pour tous les heures sympas passées en faisant du sport ; Godefroy Lemenager pour son soutien infaillible ; Stefan Klaes pour son humour extraordinaire ; Hongye pour les discussions enrichissants ; Isabelle Maurin pour tous les discussions sympas, mais bien sûr aussi tous les autres que je ne peux tous nommer sans exploser le cadre. Mes remerciements doivent bien sûr aussi inclure mes amis d'Autriche qui m'ont soutenu pendant ma thèse. Notamment Thomas, Lisi, Berni, Judith, Gernot, Kerstin, Christian, Fabio, Chrisi, Barbara, Mike et Tom.

Je veux aussi exprimer toute ma gratitude à Maria Castellano Sanz qui m'a soutenu énormément. On a partagé de jours à jours nos hauts et nos bas de la vie de chercheurs : que notre amitié perdure, profonde et fidèle.

Il est tout particulièrement important pour moi d'exprimer ma gratitude à la famille Ink, qui m'a accueilli très chaleureusement parmi eux et qui m'ont appris à vivre en et apprécier la France. C'est surtout grâce à Marion que j'ai trouvé la force de faire ce travail. Je la remercie, avec toute ma gratitude, pour son soutien, sa patience et sa compréhension vis-à-vis du temps que j'ai passé à travailler. Nous avons passé de très beaux moments ensemble : elle et sa famille auront toujours une place dans mon cœur.

Mes remerciements vont enfin à ma famille. Je remercie ma sœur et mes frères pour leur soutien et leur amour, et je remercie surtout mes parents qui m'ont toujours soutenu dans n'importe quelle aventure, comme faire une thèse en France. Merci, de toujours croire en moi et d'être derrière moi.

CONTENTS

RESUME 1

GENERAL INTRODUCTION 7

1 STATE OF THE ART & STRATEGY 11

1.1 Introduction 12

1.2 Pathogens 12

1.2.1 Definition and types 12

1.2.2 Ochratoxin 13

1.2.3 Methods for detecting pathogens 15

1.3 Aptamer-based biosensors 18

1.3.1 Aptamers as probes in biosensors 18

1.3.2 Aptamers for the detection of OTA 21

1.3.3 Aptamer-based biosensors for the detection of OTA 22

1.3.4 Challenges for biosensors 24

1.4 Strategy proposed for detecting the interaction aptamer-OTA 25

1.4.1 Direct detection of the interaction aptamer-OTA by ATR-FTIR 26

1.4.2 Indirect detection of the interaction aptamer-OTA by fluorescence 26

2 SURFACE FUNCTIONALIZATION OF OXIDE FREE SILICON SURFACES 29

2.1 Introduction 30

2.2 State of the Art 31

2.2.1 Functionalization of silicon surfaces 31

2.2.2 Two-step amidation of acid terminated surfaces 35

2.3 Materials and Methods 39

2.3.1 Chemicals and substrates 39

2.3.2 Hydrogenated silicon surfaces 40

2.3.3 Photochemical hydrosilylation of undecylenic acid 40

2.3.4 Activation with EDC/NHS of acid-terminated surfaces 41

2.3.5 Aminolysis of PEG 750 on activated silicon surfaces 41

2.3.6 Adsorption test of *E. coli* Katushka K12 on PEG-surfaces 42

2.4 Results and discussion 42

2.4.1 Hydrogenation of silicon surfaces 42
2.4.2 Grafting of undecylenic acid on silicon surfaces by hydrosilylation 44
2.4.3 Activation with EDC/NHS of acid-terminated surfaces 46
2.4.4 Aminolysis of an activated silicon surface with PEG 750 48
2.4.5 Adsorption test of *E. coli* Katushka K12 on PEG-surfaces 50
2.5 Conclusion 53
3 CHARACTERIZATION OF OCHRATOXIN A IN PHYSIOLOGICAL BUFFER SOLUTIONS . 55
3.1 Introduction 56
3.2 Materials and methods 58
3.2.1 Chemicals and substrates 58
3.2.2 Preparation of OTA-solutions for in-situ IR spectroscopy 58
3.2.3 Preparation of OTA-solutions for UV-vis spectroscopy 59
3.3 Results and discussion 59
3.3.1 The relation of OTA-structure with IR response and UV-vis absorption 59
3.3.2 Calibration of OTA IR-intensity and UV-vis absorption to OTA-concentration in solution 67
3.4 Conclusion 72
4 INTERACTION APTAMER – OTA 73
4.1 Introduction 74
4.2 Materials and methods 75
4.2.1 Chemicals, substrates and devices 75
4.2.2 Aminolysis with aptamers 75
4.2.3 Interaction of OTA and warfarin with aptamers 76
4.2.4 Regeneration of OTA from its aptamers 76
4.3 Results and discussion 77
4.3.1 Aminolysis of activated silicon surfaces with aptamers 77
4.3.2 Interaction of OTA with its aptamer by IR on crystalline silicon surfaces 90
4.3.3 Regeneration of aptamers 94
4.3.4 Non-specific interaction of aptamers with warfarin 98
4.4 Conclusion 101
5 FLUORESCENT BIOCHIPS FOR OTA DETECTION 103
5.1 Introduction 104

5.2 Materials and Methods 106
5.2.1 Chemicals and substrates 106
5.2.2 Transfer of protocols from crystalline silicon 107
5.2.3 Preparation of solutions for spotting 108
5.2.4 Blocking of remaining active surface sites 108
5.2.5 Hybridization with complementary oligonucleotides 108
5.2.6 Association with OTA 109
5.3 Results and discussion 110
5.3.1 PECVD-calibration 110
5.3.2 Fluorescent assays 118
5.4 Conclusion 135
6 GENERAL CONCLUSION AND OUTLOOK 137
LIST OF ABBREVIATIONS AND ACRONYMS 141
ANNEX 142
A.I. ATR-FTIR spectroscopy 143
A.II. Scanning electron microscopy 148
A.III. Thermal vapor deposition 149
A.IV. Plasma enhanced chemical vapor deposition 149
A.V. Robotic spotter 150
A.VI. Fluorescence imaging 151
REFERENCES 154

RESUME

La détection et l'identification des pathogènes est un enjeu crucial pour la biosécurité des pays, en particulier dans la lutte contre le bioterrorisme.[1] Les biocapteurs sont une méthode de détection optimale, car ils permettent une détection facile et sensible des cibles.[2] Ils ont un potentiel fort car ils peuvent être conçus pour être compacts et portables, tout en permettant la détection en temps réel d'agents pathogènes ou de produits chimiques dangereux.

Il y a plus de cinquante ans[3], les premiers biocapteur pour la surveillance en continue de la composition du sang ont été testés lors d'interventions chirurgicales. Depuis, les biocapteurs ont été au centre des intérêts de la recherche et ont aussi démontré une utilité dans une grande gamme d'applications (médicale, pharmaceutique, biosécurité…).[1,4,5] Généralement les biocapteurs sont constitués d'un élément de reconnaissance biologique (biorécepteur) et d'un transducteur qui convertit une réaction biochimique à un signal mesurable.[2] Les biopuces sont généralement constituées d'une matrice de biosenseurs, ce qui permet une analyse simultanée (multiplexée) de différentes réactions biochimiques. Les biorécepteurs peuvent être des systèmes ou des espèces biologiques, ainsi que des matériaux biomimétiques. Ils sont formés à partir de molécules biologiques, telles que des séquences d'acide nucléique,[6] de protéines (anticorps, antigènes, enzymes, ...),[7,8] de cellules entières ou de fragments subcellulaires.[9,10] En particulier les aptamères, qui sont des brins simples d'acides nucléiques (ARN et ADN), sont particulièrement intéressant. Ils sont une excellentes sondes alternatives, car ils peuvent présenter une affinité et une sélectivité élevées vers une large gamme de cibles spécifiques (des petites molécules chimiques à des cellules entières).[11] Les aptamères présentent également l'avantage d'être modifiables à façon, et sont comparativement plus faciles et moins à produire.

Une des questions les plus importantes dans la technologie des biocapteurs est la fiabilité et la reproductibilité, en particulier l'immobilisation des sondes peut poser des limitations sérieuses.[12] Un grand nombre de techniques présentent des inconvénients

sérieux pour une immobilisation fiable des sondes, mais aussi pour la passivation des surfaces et pour éviter l'adsorption non spécifique.

Dans le laboratoire PMC, le greffage bien contrôlé de 1-alcènes sur des surfaces de silicium exemptes d'oxygène a été étudié pour une immobilisation fiable par des liaisons stables et covalentes Si-C.[13–16] En particulier, l'hydrosilylation photochimique de l'acide undécylénique entraîne une monocouche organique terminée d'acide carboxylique sur des surfaces de silicium hydrogénées.[17] Les groupes d'acides permettent une modification chimique supplémentaire de la surface avec des biomolécules par une stratégie d'amidation en deux étapes dans des conditions douces et en utilisant des réactifs de couplage de peptides de carbodiimide bien connus.[18,19] Cette chimie a été utilisée pour développer des micro-arrays, où une couche mince d'un alliage de carbone de silicium amorphe hydrogéné (a-$Si_{1-x}C_x$:H) est déposée sur des couches métalliques ou des nanostructures métalliques. Cela permet d'optimiser la fluorescence des fluorophores greffés sur ces couches.[14,20–22] Les propriétés optiques de la couche a-$Si_{1-x}C_x$:H déposée par dépôt chimique en phase vapeur assisté par plasma (PECVD) ont été réglées et optimisées, ce qui a donné une sensibilité extrêmement élevée de 5 fM pour l'interaction ADN-ADN.[23]

L'objectif de cette thèse est d'étudier l'interaction des agents pathogènes avec les aptamères sur une architecture de biopuces stable et reproductible basée sur un alliage de carbone de silicium amorphe hydrogéné (a-$Si_{1-x}C_x$:H) déposé sur un rétroréflecteur en aluminium pour une détection fiable et sensible d'agents pathogènes par fluorescence. La surface de silicium permet le greffage de monocouches organiques à terminaison acide avec des liaisons Si-C robustes. Les couches terminées par des groups acides sont des candidats excellents pour une immobilisation fiable de sondes à terminaison amine par des liaisons peptidiques covalentes. Le substrat de silicium est non seulement la base d'une immobilisation fiable mais fournit également une plateforme d'analyse et de quantification par spectroscopie infrarouge, ainsi qu'une analyse avec fluorescence pour une sensibilité augmentée. Sur cette architecture, nous introduisons l'interaction de la toxine ochratoxine A (OTA) avec son ADN-aptamère 36mer comme système modèle.

Le procédé de modification multi-étapes que nous effectuons sur le silicium sera expliqué plus en détail au chapitre 2. Des surfaces de silicium à terminaison d'hydrogène sont utilisées comme base pour le greffage d'une monocouche d'acide organique par hydrosilylation photochimique. Il en résulte une monocouche très stable liée par des liaisons Si-C covalentes. La couche stable terminée par un acide constitue alors la base de l'étape suivante, dans laquelle les aptamères à terminaison amine sont immobilisés sur la surface par un processus d'amidation en deux étapes. L'amidation en deux étapes consiste d'abord d'une réaction d'activation de la surface avec le carbodiimide EDC en présence de NHS. Ceci est suivi d'une réaction d'aminolyse, conduisant à des aptamères immobilisés sur la monocouche organique par des liaisons peptidiques stables. Cette stratégie d'immobilisation donne au substrat une haute stabilité chimique par rapport au vieillissement et à une longue exposition dans des milieux physiologiques. Une fois les aptamères immobilisés sur la surface, l'interaction aptamère-OTA est réalisée.

Le manuscrit est conçu comme suit :

Le premier chapitre présente le concept des agents pathogènes, leurs classifications et leurs méthodes de détection. Le concept d'aptamères est discuté, avant d'expliquer plus en détail la stratégie de détection de l'interaction entre la toxine alimentaire ochratoxine A (OTA) et son aptamère.

Le deuxième chapitre présente en détail la fonctionnalisation des surfaces de silicium pour l'immobilisation des groupes fonctionnels à terminaison NH_2. Les modifications contrôlées sont étudiées quantitativement par spectroscopie infrarouge à transformée de Fourier en géométrie de réflexion totale atténuée (ATR-FTIR). En particulier, comme exemple, le PEG-NH_2 a été immobilisé pour créer une surface anti-bio-fouling. La couche d'oxyde de substrats de silicium a été enlevée par gravure HF. Ceci a permis le greffage de l'acide undécylénique par hydrosilylation photochimique, conduisant à une monocouche organique à terminaison carboxyle, fixée par des liaisons covalentes Si-C possédant une densité surfacique dense de $N_{CO} = 2.5 \cdot 10^{14} cm^{-2}$ et ayant une couverture de surface de $\theta = 32\%$. L'étape suivante consiste à activer la surface avec EDC / NHS, ce qui conduit à des groupes ester-NHS sur la surface, qui à leur tour subissent une réaction d'aminolyse et sont ainsi remplacés par des (bio) molécules à

terminaison amine, comme des PEGs ou aptamères. Les molécules de PEG sont immobilisées avec succès sur des monocouches à terminaison ester-NHS. Une analyse quantitative de l'acide restant sur la surface permet de calculer la densité surfacique des chaînes de PEG sur la surface de $\mathrm{N_{PEG}} = 1.7 \cdot 10^{14}\ \mathrm{cm}^2$, avec un rendement de réaction de $\eta = 64\%$. Les propriétés anti-biofouling vis à vis E. coli Katushka K12 a été montrée qualitativement par fluorescence et microscopie optique pour trois surfaces PEG différentes (PEG 750, PEG 2000 et PEG 5000). Les trois surfaces PEG ont montré un comportement prometteur anti-biofouling.

Le troisième chapitre décrit la caractérisation de l'OTA dans différents milieux physiologiques par spectroscopie in-situ ATR-IR et UV-vis. Ce chapitre présente en détail l'étude de la relation de la structure d'OTA avec sa réponse infrarouge et UV-vis dans différents milieux. Cette relation a été d'abord étudiée pour l'OTA dans différents milieux (méthanol et H_2O) et à différents pH par infrarouge in-situ. Les mesures in situ de l'OTA dans l'eau ont été effectuées dans des conditions de travail similaire à ceux qui prévalent lors de l'interaction de l'OTA avec son aptamère. On a trouvé que dans le méthanol, l'OTA est sous sa forme déprotonée, alors que dans H_2O à pH 7 il est sous une forme une fois déprotonée. A pH 8.5 et 11, la forme ouverte et la forme deux fois déprotonée coexiste probablement. Des mesures de spectroscopie UV-vis ont été effectuées et le comportement similaire pour les différentes valeurs de pH a été observé, comme par IR, on ne peut pas différencier entre les structures protonée est une fois déprotonée, ainsi qu'entre les formes deux fois déprotonée est ouverte. Une mesure de calibration d'IR in-situ a été effectuée avec succès dans H_2O, pH 8.5 afin de pouvoir quantifier l'OTA sur les surfaces après interaction avec les aptamères. Ceci a été suivi par une mesure de calibration UV-vis qui permet la quantification de l'OTA dans un tampon de régénération.

Le quatrième chapitre est l'étude de l'interaction de l'OTA avec son aptamère immobilisé sur des surfaces de silicium cristallin. Nous présenterons au début la stratégie d'immobilisation des aptamères à terminaison NH_2 sur des surfaces de silicium fonctionnalisées. Le rendement de la réaction d'aminolyse a été augmenté en optimisant la composition du tampon et le pH, ainsi que la concentration en aptamère. Une fois qu'un tampon idéal a été trouvé pour la réaction d'aminolyse, le rendement a

été encore augmenté en répétant les réactions d'activation et d'aminolyse jusqu'à ce qu'aucune autre immobilisation d'aptamères n'ait lieu sur les surfaces. Après cette optimisation nous avons obtenu une densité surfacique d'aptamère de $N_{apta} = 1.6 \cdot 10^{14}\ cm^{-2}$. L'interaction de l'OTA avec son aptamère sur les surfaces a été démontrée avec succès et quantifiée pour la première fois par ATR-FTIR, donnant une densité surfacique OTA de $N_{OTA} = 1.9 \cdot 10^{13}\ cm^{-2}$ sur les aptamères. La régénération des aptamères (élimination de l'OTA) a été étudiée avec deux méthodes. La quantification des surfaces par ATR-FTIR a montré que 63% (ou $1.2 \cdot 10^{13}\ cm^{-2}$) de l'OTA ont été enlevé, tandis que la quantification de la solution tampon de régénération par spectroscopie UV-vis a donné un densité inférieure par un facteur 3. Finalement, la spécificité de l'aptamère vis-à-vis de l'OTA a été démontrée en utilisant une molécule chimiquement similaire (warfarine), vers laquelle l'aptamère n'a montré aucune affinité.

Après avoir vu l'interaction de l'OTA avec ses aptamères directement par spectroscopie infrarouge, nous avons observé l'interaction OTA-aptamère indirectement par fluorescence sur l'architecture des biopuces. Le dernier chapitre est donc consacré au transfert des protocoles du système du silicium cristallin à l'architecture de biopuces a-$Si_{1-x}C_x$:H pour la détection indirecte de l'interaction OTA-aptamère par spectroscopie de fluorescence. L'architecture des biopuces est basée sur un film de 44 nm a-$Si_{1-x}C_x$:H déposé sur un rétroréflecteur en aluminium. Dans une première étape, le dépôt PECVD de a-$Si_{1-x}C_x$:H a été étalonné pour assurer une bonne augmentation de signal de fluorescence. Le taux de dépôt pour un $Si_{0.85}C_{0.15}$:H a été trouvé à 1.10 µm / h Deux méthodes de détection par fluorescence (signal OFF et signal ON) ont été étudiées avec des brins complémentaires de longueur 13 mer (13 base nucléique). Les résultats obtenu étaient prometteurs, avec un changement relatif de signal de 75% et 64% par l'association pour "signal OFF" et "signal ON", respectivement. Néanmoins, une sévérité accrue conduit à des résultats faussement positifs, où aucune différence n'a été trouvée entre une association « blanc » et une association avec l'OTA. La forte diminution de l'intensité de fluorescence des spots témoins a conduit à l'étude de la qualité de l'immobilisation des oligonucléotides, qui se sont révélé être stables et bien contrôlées. Enfin, deux directions différentes d'immobilisation d'aptamère (par la côté 3' et 5') ont été comparées vis-à-vis de trois

brins complémentaires différents. Les trois brins complémentaires étaient deux 18 mer, un à chaque extrémité, et un 36mer. La meilleure combinaison trouvait, fut l'aptamère immobilisé sur le 5' avec un brin complémentaire d'une longueur 18 mer marqué sur le 5', et qui présentait une perte de signal relative de 40,9% avec OTA et 23,9% sans OTA.

GENERAL INTRODUCTION

The detection and identification of pathogenic targets is a critical issue for national biosecurity, especially in the fight against bioterrorism.[1] Biosensors are an optimal method of detection as they allow easy and sensitive detection of targets.[2] They have a high potential for in-field use as they can be designed to be compact and portable, while enabling real time detection of pathogens or dangerous chemicals.

Over fifty years ago the first biosensor for the continuous monitoring of the chemical composition of blood during surgery was reported.[3] Ever since biosensors have been in the centre of research interests and have shown rapid growth in a wide range of applications such as medical, pharmaceutical or biosecurity.[1,4,5] Biosensors generally consist of a biological recognition element (bioreceptor) and a transducer which converts a biochemical reaction into a measurable signal.[2] Biochips are usually composed of large arrays of biosensors, which allow simultaneous (multiplex) analysis of different biochemical reactions. The bioreceptors are either biological systems or species, or biomimetic materials, and are formed from biological molecules, such as nucleic acid sequences,[6] proteins (antibodies, antigens, enzymes,…),[7,8] whole cells and sub-cellular fragments.[9,10] Especially aptamers, which are ligand-binding single strands of nucleic acids (RNA and DNA), have moved into the centre of interest.[5] They are a great alternative as probes as they can be engineered to exhibit a high affinity and selectivity towards a wide range of specific targets (from small chemical molecules to whole cells).[11] Aptamers also display the advantage of being site specifically modifiable as well as comparably easy and cheap to produce.

One of the most important issues in biosensor technology is the reliability and reproducibility, especially the immobilization of probes can impose serious limitations.[12] Many techniques display serious drawbacks for reliable probe immobilization, but also towards surface passivation and avoidance of non-specific adsorption.

In the laboratory PMC the well-controlled grafting of 1-alkenes on oxygen-free silicon surfaces for a reliable immobilization by covalent Si-C bonds has been studied

extensively.[13–16] Especially the photochemical hydrosilylation of undecylenic acid results in a carboxylic acid-terminated organic monolayer grafted on hydrogenated silicon surfaces.[17] The acid groups allow further chemical modification of the surface with biomolecules by a two-step amidation strategy in mild conditions, using well-known carbodiimide peptide coupling reagents.[18,19]

This well mastered chemistry was used to develop microarrays, where a layer of an hydrogenated amorphous silicon carbon alloy (a-$Si_{1-X}C_X$:H) is deposited on metal thin films or metallic nanostructures for enhanced fluorescence.[14,20–22] The optical properties of the a-$Si_{1-X}C_X$:H-layer deposited by plasma enhanced chemical vapor deposition (PECVD) were tuned and optimized, resulting in an extremely high sensitivity of 5 fM for DNA-DNA interaction.[23]

The goal of this thesis is to develop a stable and reproducible chemistry for biochips, for a reliable and sensitive detection of pathogens by fluorescence. For this amino-terminated aptamers are immobilized by peptide bonds on carboxyl-terminated monolayers. These organic monolayers are grafted on an a-$Si_{1-X}C_X$:H-layer which is deposited on an aluminium back reflector. The interaction of the food and feed toxin Ochratoxin A (OTA) with its 36-base (or 36mer) DNA-aptamer is introduced as model system on our biochip architecture.

The first chapter introduces the concept of pathogens, their classifications and methods of detection. The concept of aptamers is discussed, before explaining in more detail the strategy for detecting the interaction between the food and feed toxin Ochratoxin A (OTA) and its aptamer.

The second chapter is dedicated towards the surface functionalization of oxide free crystalline silicon surfaces. The state of the art is compared with the methods we applied for a stable multi-step functionalization by covalent bonds, for the immobilization of amino-terminated functional groups. The well-controlled modifications are studied quantitatively by Fourier-transform infrared spectroscopy in attenuated total reflection geometry (ATR-FTIR).

The third chapter describes the characterization of OTA in different physiological media by *in-situ* ATR-IR and UV-vis spectroscopy. Calibration measurements for the quantification of OTA on surfaces will be discussed.

The fourth chapter is the study of the interaction of OTA with its immobilized aptamer on crystalline silicon surfaces. Quantitative ATR-IR and UV-vis spectroscopy allow to determine the density of OTA on surfaces. The specificity of the aptamer towards OTA is demonstrated by studying its affinity towards a chemically similar molecule.

The last chapter is dedicated to the transfer of the system from crystalline silicon to the a-$Si_{1-X}C_X$:H biochip architecture for indirect detection of the interaction OTA-aptamer by fluorescence spectroscopy.

1 State of the Art & Strategy

1.1 Introduction

Pathogens pose a crucial risk for a country's biosecurity, in the fight against bioterrorism, but also for the protection against infectious diseases. They pose danger to living beings and include bacteria, viruses, fungi and toxins. Biochips offer a way of rapidly detecting a wide range of pathogens and can be designed to be compact and be used by semi-skilled personnel in emergency situations.[1]

As the subject of pathogens is very wide, this chapter provides an introduction into the concept of pathogens, the ways they are classified, and an overview over methods for their detection, especially biosensors. Aptasensors are a subgroup of biosensors which use single strands of DNA (aptamers) as probes. They will be discussed towards the detection of ochratoxin, which we introduce as a model system for studying the interaction of pathogens with aptamers with our biochip architecture. Therefore both aptamers and ochratoxins will be addressed. Finally the strategy for detecting directly and indirectly the interaction between OTA and its aptamer will be discussed.

1.2 Pathogens

1.2.1 Definition and types

Pathogens, or more specifically bio-threat agents, generally include bacteria, viruses, fungi and toxins that harm or kill people, animals and plants, and which can deliberately be used as a weapon.[1] Lists of potential agents are created by the NIAID (National Institute of Allergy and Infectious Diseases, USA) or the ECDC (European Centre for Disease Prevention and Control) and include a large number of agents, reflecting the fact that many common pathogens have the capacity of causing harm to humans or economic damage.[1] The classification of biological agents is either done operationally (lethal vs. incapacitating), legally (limited possession and transportation rights) or regulatory. The regulatory classification by the NIAID differs between three priority categories: Category A, Category B, Category C.[24] The Category A agents pose a

national security risk, as they have high morbidity and mortality rates and furthermore can disseminate and be transmitted easily. Most of these agents require biosafety level 4 for laboratories. The Category B agents disseminate with moderate ease but have a low mortality rate and can be contained relatively easily. Category C agents are emerging pathogens which might be engineered for mass dissemination. This can be because they are easily available, easy to produce and easy to spread, and/or because they have potential for high morbidity and mortality rates.[1,24,25] Examples of pathogens in these categories are listed in Table 1.

Table 1: Examples of pathogens of the NIAID priority categories A-C.

Category	**Examples**
A	*Anthracis*, smallpox, bubonic plague
B	*Brucellosis*, *Typhus*, *Escherichia coli*, *Salmonella* and ricin toxin
C	*Tuberculosis*, rabies virus and prions

1.2.2 Ochratoxin

Ochratoxins are a group of mycotoxins which are produced by secondary metabolism by several species of fungi. It was first found in Aspergillus ochraceus by Scott[26] in 1965 and then isolated by the group of van der Merwe[27,28] in the same year. Other ochratoxin producing fungi are Penicillium,[29] and other members of Aspergillus.[30–32] Ochratoxins contaminate food and feed sources,[33] but meat can also contain ochratoxin through secondary contamination.[34,35] The group of the ochratoxins includes several related metabolites. While ochratoxin A is the most harmful, there are also other ones like the dechloro analog ochratoxin B, or its methyl ester ochratoxin C (the chemical structures are displayed in Figure 1).[36]

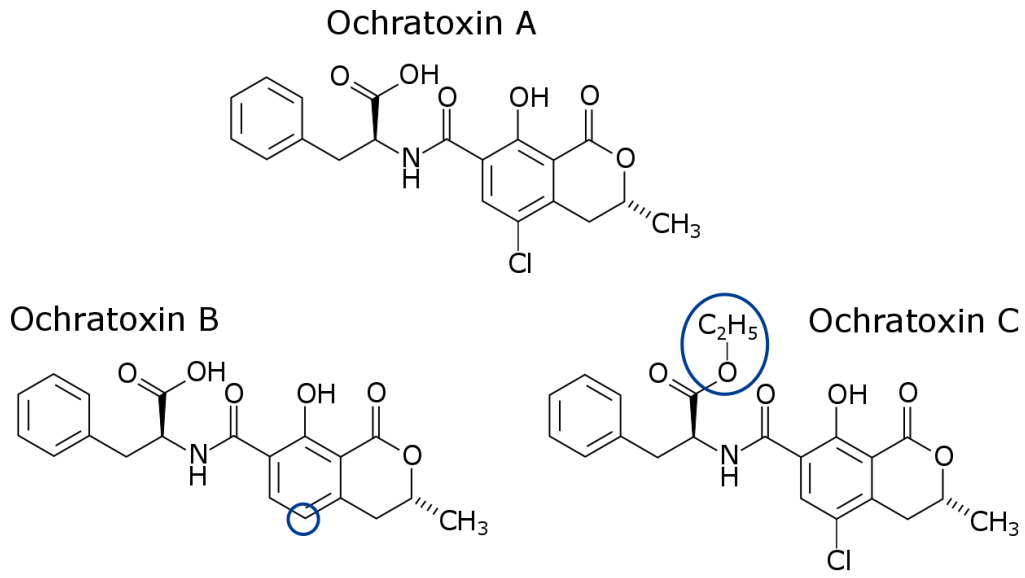


Figure 1: Chemical structure of ochratoxin A, ochratoxin B and ochratoxin C. Blue circles highlight the differences.

OTA is severely toxic for humans and animals, displaying nephrotoxic[37,38], hepatotoxic,[39,40] neurotoxic,[41,42] teratogenic,[43,44] immunotoxic,[45,46] and potentially carcinogenic[47,48] effects on organisms.

The tolerable weekly intake of OTA has been set at 120 ng/kg by the European Food Safety Authority (EFSA).[49] More restrictive regulations have been established by other agencies, for example the US Food and Drug Administration (FDA) considers the tolerable daily intake to be 5 ng/kg.[50]

Since OTA has hazardous effects on the human health the testing of real food samples for it has been regulated by the European Union. While several possibilities for measuring the OTA content in food samples exist, the most commonly used is high-performance liquid-chromatography (HPLC) combined with fluorescence detection systems (FD).[51] HPLC-FD returns results quickly, and allows relatively precise quantification with a limit of detection (LOD) of 0.55 ng/mL,[52] but extensive sample pretreatment is necessary, and parallel analysis for multiple targets is cumbersome. Other rather traditional methods of detection are:

- Liquid chromatography – mass spectrometry (LC-MS/MS), LOD: 0.01 ng/mL [53]
- Enzyme-linked immunosorbent assays (ELISA), LOD: 0.3 ng/mL [54]
- Fluorescence-based immunoassays, LOD: 0.012 ng/mL [55]

1.2.3 Methods for detecting pathogens

The conventional methods for detecting pathogens can be very time-consuming and labor intensive. For example pathogenic bacteria are traditionally cultured on agar plates with subsequent standard biochemical identification.[56] More recently developed methods are faster and can provide higher sensitivity and specificity. They include nucleic acid-based methods, immunology-based methods and biosensors.

Nucleic acid-based methods

The principle of the nucleic acid-based methods is based on the detection of bacteria-specific DNA or RNA by hybridizing it with artificial complementary oligonucleotides.[57] These methods include the probably most commonly used polymerase chain reaction (PCR), but also newer developments like quantitative PCR (qPCR), multiplex PCR (mPCR) and other strategies like microarray technology. PCR is a method for amplifying nucleic acids, which was developed in the 80s by Mullis et al.[58] The PCR process generally consists of 20-50 cycles as displayed in Figure 2. In the first step (denaturation) the double-stranded DNA is heated to separate the strands. For the next step specific primers are added and anneal with the single strands of DNA. In the last step of the cycle the DNA-polymerase fills up the missing strands with free nucleotides, starting from the 3'-side of the primer and following the strand. The two new double strands can then be used for the next cycle, resulting in exponential amplification.[58–60]

The main advantages of PCR lie in its high sensitivity and high specificity, but it can also be automated and yield reliable results. Nevertheless the results can be affected by PCR inhibitors and the DNA requires purification.

qPCR improves on normal PCR as in addition to PCRs advantages it allows rapid cycling, no post-amplification products are necessary and real-time monitoring is possible. At the same time it has to cope with the same disadvantages of PCR and being rather expensive and multiplex measurements are difficult.

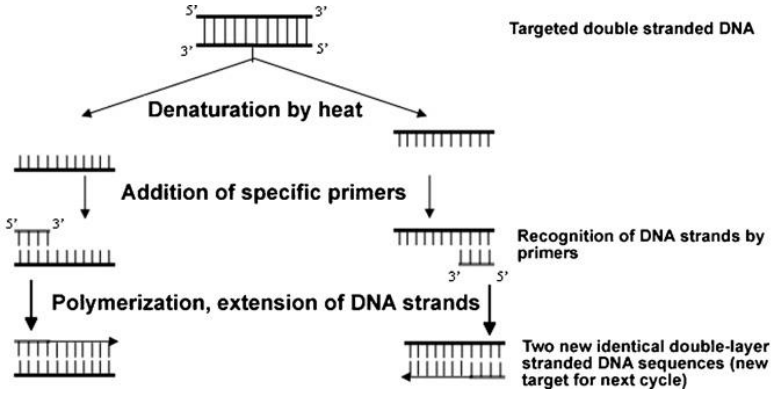


Figure 2: Schema of one PCR cycle for the amplification of DNA.[60]

Immunology based methods

These methods rely on high specificity and affinity of antibodies towards their antigen. It is one of the few methods which has been successfully applied for the detection of bacteria, viruses, spores and toxins.[61] Some of the better known methods applied are enzyme-linked immunosorbent assay (ELISA)[62], magnetic immunoassay (MIA)[63] and lateral flow immunoassay (LFIA)[64,65]. ELISA is a very popular method, with the sandwich method (see Figure 3) being its most effective form.[57] For this method in the first step (1) antibodies are immobilized before the targets are added (2). In the next step (3) an antigen detecting antibody binds to the target. Then an enzyme-labelled antibody binds to the detecting antibody (4). Finally (5), the enzyme's substrate is added, which reacts to a detectable product.

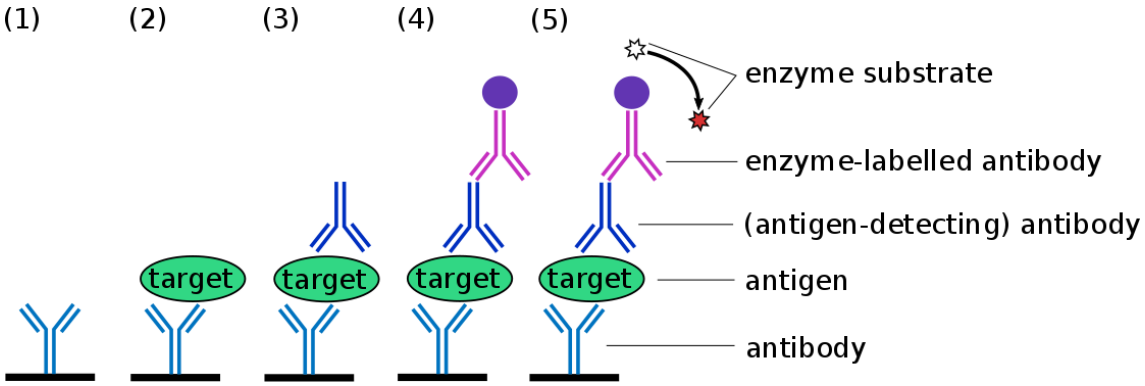


Figure 3: Schema of sandwich ELISA process.

ELISA can be applied for a wide range of targets, is very specific and can be automated to reduce time and labor needs. Nevertheless it struggles with low sensitivity, the risk

of false high-positive results and especially the fact, that the antibody might interact with similar antigens.[66] Further challenges are posed by the controlled immobilization of antibodies and the denaturation of the antibodies on surfaces.[66]

Biosensors

Biosensors are analytical devices with a biological component. They are used in many different applications, including environmental, electrochemical, clinical and security.[1,4,67,68] The analysis is based rather on function than on structure, and they can be used to detect against a wide range of targets:

- Toxins (food and feed stock contamination, security…)[54,69]
- Carcinogens (food contamination, released by industrial processes…)[70]
- Human vitals (blood glucose level, cancer…)[71,72]
- Pesticides (food contamination, detection in environment, e.g. DDT)[73,74]
- Drug detection (low level detection in environment or in pharmaceuticals)[75,76]
- Microbial contamination (food, environmental hazards, security)[77–79]

Biosensors combine a biological recognition component (or bioreceptor) with a physico-chemical transducer and possibly an (electronic) amplifier, as displayed in Figure 4. The bioreceptor uses biological probes to interact with the analyte and directly converts its presence or concentration from a biological reaction into a physico-chemical effect, which is measurable by the transducer.

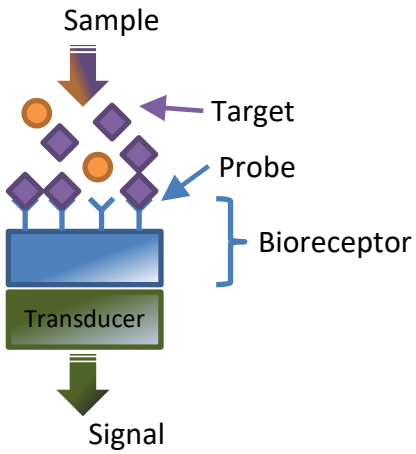


Figure 4: General structure of biosensors.

The bioreceptors of biosensors can be separated into five different main types:

(i) Biological polymers including nucleic acids[80,81], aptamers[82–84] and peptides[85]

(ii) Proteins such as antibodies and antigens[77,86]

(iii) Enzymes[67,87,88],abzymes (catalytic antibodies)[89,90] and other proteins[91,92]

(iv) Whole cells and cellular fragments using plant or animal cells[93,94], microorganisms[95], organelles[96], cell receptors[97,98], and tissue slices[99]

(v) Biomimetic materials[100,101]

There are various types of transducers, which convert different kinds of reactions into measurable signals and which depend on the intrinsic properties of the substrate. Electrochemical transducers detect an electrochemical reaction by monitoring the change of an electrical signal at an electrode.[102] Optical transducers detect the change of refractive index,[103] light interference,[104] changes in local surface plasmon resonance frequencies (LSPR)[105] and other properties.[106] Acoustic transducers are based on wave propagation in solids. They exploit, for example, resonance-frequencies[77] of piezoelectric materials[107,108] to detect surface interactions. There are also other technologies which are used as transducers, among others gravimetric,[109] thermal[110] and magnetic.[111]

Biochips, in comparison to biosensors, allow the detection of multiple analytes in parallel. One well known and widely used example is the microarray, which allows the detection of a wide range of analytes on one slide. The two most common methods of detection with microarrays are fluorescence and SPR.

1.3 Aptamer-based biosensors

1.3.1 Aptamers as probes in biosensors

Aptamers are single stranded DNA or RNA molecules, which have been specifically selected to bind with high specificity and affinity to a certain target by a process called **S**ystematic **E**volution of **L**igands by **EX**ponential enrichment (SELEX). They are

becoming increasingly popular as alternative probes for biosensors, immunoassays and other analytical devices. Aptamers display several advantages over antibodies when used as probes:

(i) *In-vitro* selection and synthesis is faster, lowers the cost and can be conducted without animals, facilitating its use for toxic compounds and increasing flexibility in selection conditions[112–115]

(ii) Synthesis can be conducted with high purity and reproducibility[116]

(iii) Smaller size enables higher surface densities[117]

(iv) Chemical modifications which don't affect the affinity are relatively easy to conduct to enhance specificity, detection, stability and allow immobilization[11,118]

(v) Higher thermal stability (reversible denaturation) and higher shelf live[11,119]

(vi) High versatility due to wider range of targets (cells, toxins, viruses, proteins, even small molecules and metal ions)[6,120–122]

(vii) Low immunogenicity and low-toxicity[123]

(viii) Can show higher affinity and specificity towards target than antibodies[115,120]

Despite all these advantages, aptamers also have some limitations:

(i) Degradation by nucleases in biological media of RNA-aptamers limits the therapeutic applications. One of the propositions to avoid this degradation include the performance of SELEX with modified stability-enhanced nucleotides[124]

(ii) Cross-reactivity with molecules of similar structure can be problematic, but binding can be avoided with negative SELEX, where aptamers that bind with similar molecules are discarded[125]

(iii) Time and labor consuming generation, despite being easier and faster to produce than antibodies. Automated SELEX has been proposed by Cox et al., which allows the generation of aptamers in several days[126]

The SELEX process which is used to find aptamers was developed in 1990 by the groups of Gold and Ellington.[112,113] The standard SELEX strategy is shown in Figure 5. The

process starts with a large library of randomized sequences (up to 10^{16}) with lengths usually around 30-50mer, but up to 100mer.[115,121] In the first step (1), the sequences are incubated with an immobilized target molecule. In the second step (2), the unbound oligonucleotides are removed from the target-bound ones. Then the oligonucleotides which were bound to the target are eluted (3) and amplified (4). The amplification is usually done with polymerase chain reaction (PCR) or real-time PCR (RT-PCR).[121] These amplified strands form the new library for the next round of this cycle, where the stringency is increased (5) to raise the competition between the remaining oligonucleotides. The cycle is repeated 10-15 times, resulting in aptamers which recognize the target molecule. The stringency is set by the selection parameters (temperature, pH, buffer composition) and can be adapted to a small or broad range of working conditions for the aptamers.

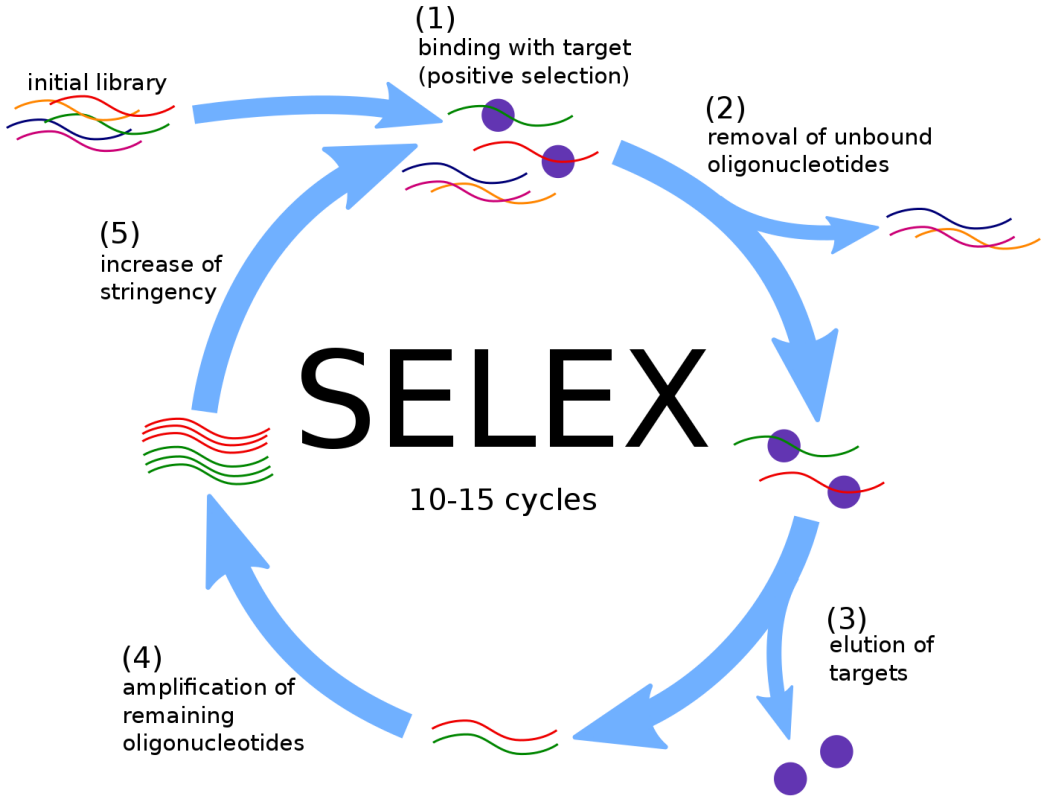


Figure 5: Standard SELEX strategy. Starting with initial library of random sequences, the binding sequences (1) are isolated (2 -> 3) and amplified (4), before the cycle reiterates at more stringent conditions (5 -> 1).

Aptamers are mainly unstructured in solution, but form well-defined 3D-structures when binding their ligands.[127] The molecular architectures which are formed include the ligand as an intrinsic part of its structure. Aptamers are also highly reusable, as they can preserve their structure when being subjected to repeated cycles of regeneration. The aptamers can be regenerated with heat, salt concentration, medium pH and chelating agents, while remaining undamaged if extreme limits are not exceeded.[11] The interaction of an aptamer with its target depends on the presence of salts and the pH of the physiological media.[128] The recognition of targets by an aptamer is characterized by any combination of: hydrogen bonding (which can result in a pseudo-base pair involving the ligand), electrostatic interactions, intermolecular bonding, general acid-base interactions, shape complementarity, and folding of the aptamer around the target, resulting in numerous intermolecular interactions.[127]

Aptamers as probes have shown a wide range of usability while being comparatively easy and cheap to produce. As the research on aptamer-based sensors advances they display more and more their competitiveness with alternative approaches.

1.3.2 Aptamers for the detection of OTA

The first aptamer towards OTA was published by Cruz-Aguado and Penner in 2008.[128] The aptamer which they isolated contains 36 nucleotides with the sequence GAT-CGG-GTG-TGG-GTG-GCG-TAA-AGG-GAG-CAT-CGG-ACA, and displays an affinity K_d of 49 nM towards OTA. They also showed that the aptamer does not bind with chemically similar molecules like warfarin and N-acetyl-L-phenylalanine and has a strongly reduced affinity towards ochratoxin B. Upon binding with OTA this aptamer takes the structure G-quadruplex, as depicted in Figure 6.[82]

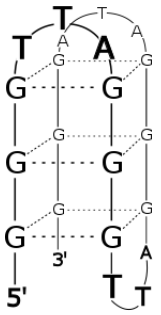


Figure 6: G-quadruplex structure of OTA-aptamer.

More recently, Barthelmebs et al. isolated two new 30mer aptamers against OTA with dissociation constants of 96 nM and 130 nM.[83] The specificity of the aptamers was also tested towards ochratoxin B and phenylalanine. Despite this alternative, the more commonly used aptamer in literature is the first one found by Cruz-Aguado and Penner.

1.3.3 Aptamer-based biosensors for the detection of OTA

There is a large number of different aptamer based methods for the detection of OTA with electrochemical or optical detection methods. An overview of the methods and their sensitivities is given in Table 2. The different detection methods show a wide range of limit of detection (LOD). Depending on the underlying method the fluorescent and luminescent methods show high sensitivities with very low LODs (fM – pM range). Electrochemical methods also show relatively high sensitivities (pM – nM range), while the colorimetric methods are less sensitive (nM range). The response range of sensors is the range in which they show a linear response with the concentration of the target, and is therefore also an important characteristic of sensors.

Table 2: Examples of aptamer-based assays for OTA detection.

Detection method	Method	Response range	LOD	Ref.
Colorimetric	Propagated chain reaction of hybridization events of DNAzymes (catalytic DNA) in solution	0.01 - 0.32 nM	0.01 nM	[129]
Colorimetric	Gold particles as indicator in solution	20 - 625 nM	20 nM	[82]
Fluorescent (FRET)	Au-nanoparticle (NP) coated with complementary, biotin-terminated strand (energy acceptor), Cy3-streptavidin (energy donor); in presence of OTA aptamer detaches and biotin and streptavidin interact resulting in signal decrease (in solution)	6.2 pM - 2.5 µM	3.7 pM	[130]
Fluorescent	Fluorophore labelled aptamer hybridized with quencher modified complementary strand; presence of OTA releases modified strand resulting in signal increase (in solution)	0.1 - 150 nM	5 fM	[131]
Luminescent	Aptamer immobilized on magnetic NP hybridizes with complementary strand on upconversion-NPs; OTA causes separation of strands and NPs, magnetic separation results in signal decrease (in solution)	0.25 fM - 2.5 nM	0.25 fM	[132]
LSPR	Localised surface plasmon resonance (LSPR)-shift of gold nanorods with immobilized aptamers (solution)	1 nM - 1 µM	1 nM	[105]
SERS	Surface-enhanced Raman spectroscopy, aptamers immobilized on Au-nanotriangles (on surface)	0.05 - 4 µM	0.05 µM	[133]
PCR-amplification signal	RT-PCR of DNA strands complementary to aptamer after dehybridization in presence of OTA in solution	12.5 pM - 12.5 nM	2.5 fM	[134]
Electrochemical	Amplified electrochemical sandwich detection and methylene blue as redox indicator, aptamers immobilized on Au-NPs (in solution)	2.5 pM - 2.5 nM	0.75 pM	[135]
Electrochemical	Either OTA or Aptamers immobilized on superparamagnetic NPs, reduced activity in presence of free OTA in solution	0.27 - 22.2 nM	0.27 nM	[136]
Electrochemical	Voltammetry: Biotin labeled and free OTA compete to bind with immobilized aptamers (in solution)	0.37 - 12.4 nM	0.17 nM	[137]

1.3.4 Challenges for biosensors

The performance of biosensors regarding sensitivity, selectivity, speed, stability, complexity, and processing depends strongly on the nature of the chosen bioreceptor and transducer. The substrate for the bioreceptor plays a major role, as its intrinsic properties define the possible measurement methods, which in turn also determine the biosensors speed, ease-of-use and possible miniaturization for portable devices. The need of high stability and reproducibility demands a reliable and well-controlled chemistry. This ensures dependable probe immobilization but also institutes the possibility of applying (antifouling) layers to avoid non-specific adsorption from targets such as proteins and bacteria. A reliable probe immobilization is also crucial for the dependability of the biosensor. The biosensors specificity and selectivity are mainly defined by the probes which are used. Another point to consider is that the probes are biological components and their production can be complex and their shelf life has to be considered before choosing a biosensor system.

1.4 Strategy proposed for detecting the interaction aptamer-OTA

The goal of this thesis is to study the interaction of pathogens with aptamers on a stable and reproducible biochip architecture based on an hydrogenated amorphous silicon carbon alloy (a-$Si_{1-x}C_x$:H) deposited on an aluminium back-reflector for reliable and sensitive detection of pathogens by fluorescence. The silicon surface enables the grafting of acid-terminated organic monolayers with robust Si-C bounds. The acid-terminated layers are excellent candidates for a reliable immobilization of amine-terminated probes by covalent peptide bonds. The silicon substrate is not only the basis for a reliable immobilization but also provides a platform for analysis and quantification by infrared spectroscopy, as well as analysis with fluorescence for an increased sensitivity. On this architecture we introduce the interaction of the toxin ochratoxin A (OTA) with its 36mer DNA-aptamer as a model system.

The well-controlled multi-step modification process which we carry out on silicon is displayed in Figure 7, and will be explained in more detail in chapter 2. Hydrogen terminated silicon surfaces (1) are used as a basis for the grafting of an acid-terminated organic monolayer by photochemical hydrosilylation (2). This results in a very stable monolayer attached by covalent Si-C bonds. The stable acid-terminated layer is then the basis for the next step (3), where the amino-terminated aptamers are immobilized on the surface by a two-step amidation process. The two-step amidation consists first of an activation reaction of the surface with the carbodiimide EDC in presence of NHS. This is followed by a subsequent aminolysis reaction, leading to aptamers immobilized on the organic monolayer by stable peptide bonds. This immobilization strategy provides the substrate with a high chemical stability with respect to ageing and long exposure in physiological media. Once the aptamers are immobilized on the surface the interaction aptamer-OTA is carried out (4).

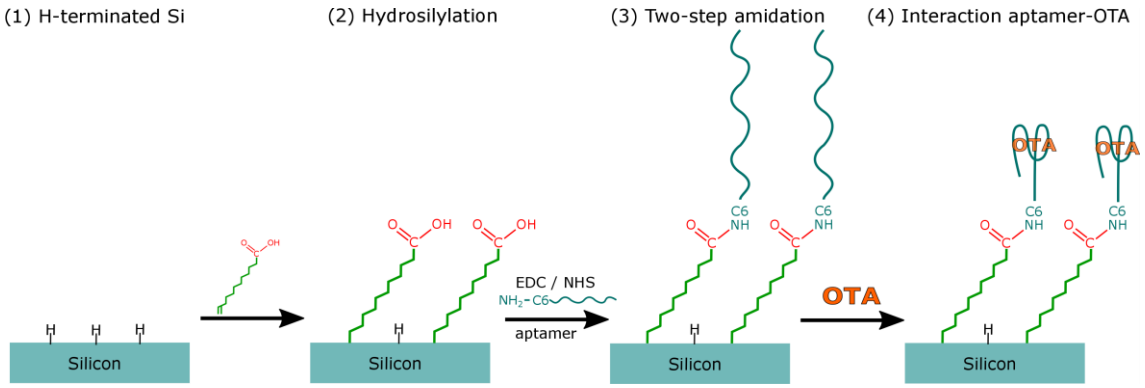


Figure 7: Strategy for direct detection of the interaction aptamer-OTA on crystalline silicon surfaces.

Two detection methods were envisaged:

1.4.1 Direct detection of the interaction aptamer-OTA by ATR-FTIR

Carrying out the surface modifications on crystalline silicon (111) allows studying of all steps by Fourier-transform infrared spectroscopy in attenuated total reflexion geometry (ATR-FTIR). This enables the study and quantification of the surface functionalization, the probe immobilization and the interaction of OTA with its aptamer without any labelling.

1.4.2 Indirect detection of the interaction aptamer-OTA by fluorescence

The chemistry is transferred to the biochip architecture. While the chemistry remains largely the same (HF-etching, hydrosilylation, 2-step amidation), it is now conducted on a thin layer of an amorphous silicon-carbon alloy (a-$Si_{0.85}C_{0.15}$:H) on an aluminium back reflector. The role of the back reflector is to increase the fluorescence sensitivity by constructive interference at the a-$Si_{1-x}C_x$:H layer.[20]

The local and defined deposition of different aptamers and oligonucleotides is carried out with a robotic spotter, giving it its biochip (multiplex) capabilities.

The biochips are based on an indirect detection of the interaction aptamer-OTA by fluorescence. Two different methods of detection on surfaces are proposed in

literature, “signal OFF” and “signal ON”. In the “signal OFF” detection method (Figure 8, left) short complementary oligonucleotides labelled with fluorophores are hybridized to the aptamers. Successful association with OTA removes the complementary strands, resulting in a decrease of fluorescence intensity. For the “signal ON” method (Figure 8 right), the attached aptamers have a fluorophore at their extremity, while the short complementary oligonucleotide has a quencher, which suppresses fluorescence of nearby fluorophores. Successful association of OTA will remove the quenchers and therefore increase the fluorescence signal.

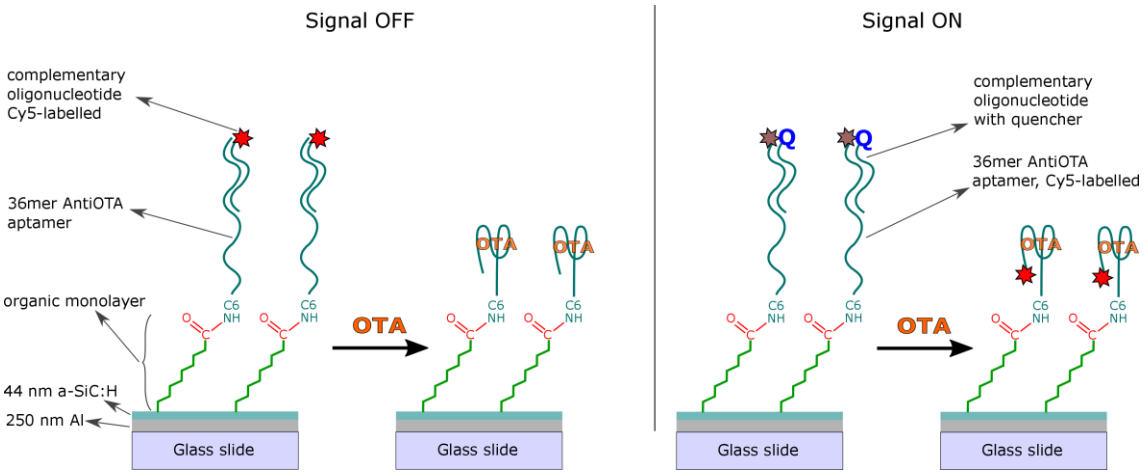


Figure 8: Strategy for indirect detection of the interaction aptamer-OTA on crystalline silicon surfaces. Left side: "signal OFF", right side: "signal ON".

2 SURFACE FUNCTIONALIZATION OF OXIDE FREE SILICON SURFACES

2.1 Introduction

Silicon and its derivatives (e.g.: silicon dioxide, silicon carbide, silicon nitride)[4,21,138,139] is of interest as a substrate for biosensors because of the chemical and physical capacities (e.g.: surface reactivity, luminescence properties), and as it comes in various forms (monocrystalline, polycrystalline, amorphous, porous, as nanoparticles)[21,140–143]. This enables its use for a wide range of different detection methods, like optical,[106,144] electronical,[2,145] electrochemical,[102,146] piezoelectrical,[108,147] and gravimetrical.[148,149] Silicon is to a certain degree biocompatible and can easily be miniaturized permitting the implementation as *in vivo* devices.[150] Furthermore, silicon surfaces can be readily functionalized with a bio-recognition layer for probe immobilization and allows modular change of its physico-chemical properties for the development of patterned or antifouling surfaces to avoid unspecific adsorption.[151–153]

The reliability, efficiency and sensitivity of biosensors strongly depends on the robustness of the chemistry between the surface and the bio-recognition layer.[106,154] Chemical stability and good reproducibility can be achieved by a well-controlled anchoring of the bio-receptive layer. Secondly, for the same reasons of reliability, efficiency and sensitivity, it also depends on the stability of further modifications of the bio-recognition layer which might be performed. These modifications are often the immobilization of probes and/or antifouling molecules. The applied chemistry must be dependable enough to guarantee stable binding, even when carrying out assay protocols in physiological media. Unreliable immobilization can impair the quality of the biosensors in terms of reproducibility and sensitivity, causing for instance reduced sensitivity due to probe loss. The immobilization of antifouling molecules is carried out to avoid unwanted non-specific adsorption on surfaces of for example proteins and bacteria. This is done to ensure that the detection is only dependent on the interaction of the probe with its target and is not affected by non-specific adsorption of the targets on the surface.

In this work we propose a multi-step process for well-controlled silicon surface modification for reliable biomolecular aptamer-target interaction. Our strategy (see Figure 9) consists of: Hydrogenation of silicon surfaces (1), to enable the grafting of carboxyl-terminated organic monolayers via stable Si-C bonds (2). This is followed by a 2-step amidation process (3 and 4), allowing the covalent immobilization of NH_2-terminated functional groups (as biological probes) in mild conditions. This chapter will start with the "state of the art" of surface functionalization, explaining in detail our method, while also pointing out some of the alternatives. In the final part the experimental results of the functionalization of oxide-free silicon surfaces will be discussed. The immobilization of the antifouling molecule poly(ethylene glycol) (PEG) was chosen as a proof of concept for the covalent binding of amine-terminated molecules on acid-terminated silicon surfaces. Its anti-biofouling properties towards bacteria are verified.

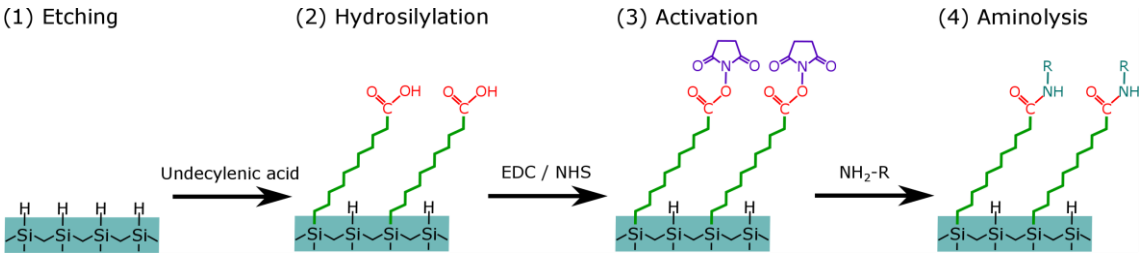


Figure 9: Strategy for silicon surface functionalization.

2.2 State of the Art

2.2.1 Functionalization of silicon surfaces

The functionalization of silicon surfaces generally follows two principle strategies, either directly on the native oxidized silicon surfaces (SiO_X), or on hydrogen-terminated silicon surfaces (SiH_X):

(a) Functionalization of native oxidized silicon surfaces

Two main methods are used for functionalizing the native silicon surface with organic molecules. The first one developed was silanization, where alkoxysilane (R_m-Si-$(OH)_n$) or chlorosilane (R_m-Si-Cl) molecules are attached through covalent Si-O-Si bonds.[155] Despite the fact that the silanization is relatively simple to carry out, it suffers under major disadvantages. Not only is the formation of reproducible and well-defined monolayers difficult, but also the Si-O bonds near the surface are easily hydrolyzed in physiological buffers.[156,157] The second method often used is the attachment of phosphonate molecules where Si-O-P bonds are formed.[158] Layers formed in this way are easily reproducible, have higher surface coverages and don't have the intrinsic risk of multilayer formation.[158,159] Despite resulting in organic layers which are more stable than those obtained by silanization, it is still relatively easily hydrolyzed from the SiO_X surface.[160] Another drawback is that the sample preparation requires heating and a relatively long processing time (more than 48 h).[161]

(b) Functionalization of hydrogenated silicon surfaces

The removal of the native oxide layer from silicon surfaces by wet chemical etching opens up other pathways of stable and reliable surface modifications via stable covalent Si-C bonds which are not subject to hydrolysis. Hydrogenated surfaces are relatively easy to prepare and can be achieved by wet chemical etching in fluoride-containing solutions at different pH.[162,163] Despite the native oxide layer re-growing relatively fast, these surfaces remain to some extent stable in air (at least one hour at room temperature and 40% ambient humidity)[164] and brief watering[165] procedures. Etching of Si (111) in basic NH_4F results in atomically flat hydrogenated SiH surfaces[163], while etching in acidic HF yields atomically rough SiH_X surfaces.[165] Porous silicon can be formed by different pathways, the first method found was stain etching, where the silicon is etched with HF, nitric acid and water.[166–168] Figure 10 shows the mechanism which leads to the formation of hydrogenated silicon by HF etching on atomically rough surfaces. In the first step the removal of oxygen leads to Si-F at the interface. This causes the Si-Si back bond to be weakened by the highly electronegative fluoride.

The fluorinated silicon can then be removed by further HF attack in form of SiF_X, leaving as a consequence an H-terminated silicon surface.[169,170]

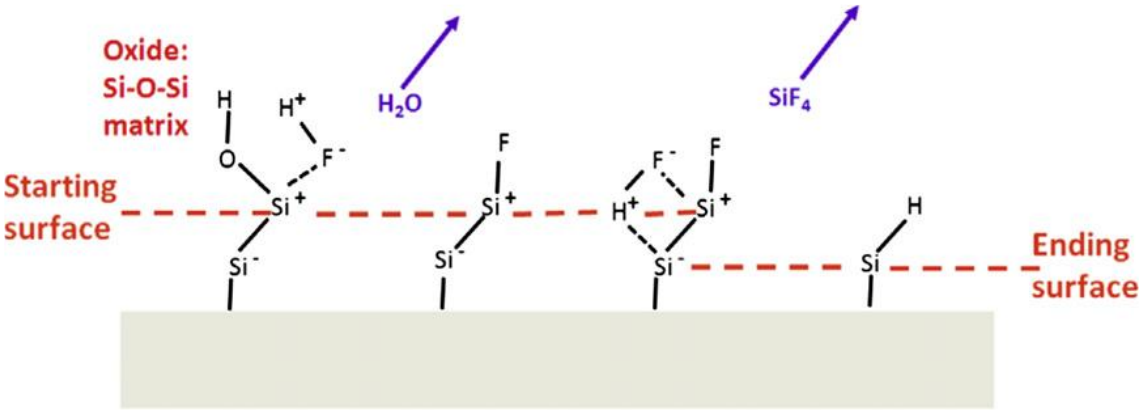


Figure 10: Mechanism of HF etching on silicon.[171]

In 1993 Linford and Chidsey reported the first formation of alkyl monolayers on non-oxidized silicon surfaces by covalent Si-C bonds, which were prepared by the pyrolysis of diacyl peroxides ($[CH_3(CH_2)_nCO]_2O_2$).[172] Since then a wide range of different methods have been developed to graft organic monolayers via stable Si-C bonds on different morphologies of hydrogenated silicon surfaces. The reaction can be conducted in two ways: (i) electrochemically with Grignard reagents[173,174], diazonium[175] and other onium salts (ammoniums and phosphoniums)[176]; or (ii) chemical hydrosilylation mediated thermally[172,177], photochemically[17,151,178,179], or catalytically[180,181].

The photochemical grafting of 1-alkenes is especially of interest because the reaction is comparably fast and easy to handle and produces densely packed and stable monolayers with low surface oxidation. It also allows grafting of alkenes with different functional groups, which can then be used to link other molecular structures to silicon surfaces.[19,182,183] The choice of functional end groups R (see Figure 11) is limited by their reactivity towards the hydrogenated silicon surface. This excludes the hydroxyl (R-OH), amine ($R-NH_2$) and aldehyde (R-CHO) groups, which would be of interest for further functionalization. One way of grafting with functional end groups is by protecting them, then grafting the alkene chains, followed by the removal of the protection. In this context in the laboratory PMC the one-step and two-step grafting of

alkyl chains with the functional group COOH via stable Si-C bonds was studied in (without or with protection, respectively).[17] This method allows the grafting of 1-alkenes with the functional group carboxyl (R-COOH). In particular the direct photochemical grafting of undecylenic acid at 312 nm was studied, resulting in carboxylic acid (COOH) terminated monolayers. The obtained surfaces showed no formation of siloxane (Si-O-C=O), confirming that the carboxyl group does not react with the surface. The surfaces exhibited fairly dense organic monolayers (surface densities up to $2.7 \cdot 10^{14}$ cm^{-2}). The grafting also displayed no surface oxidation, yielding excellent electronic properties of the interface.[17]

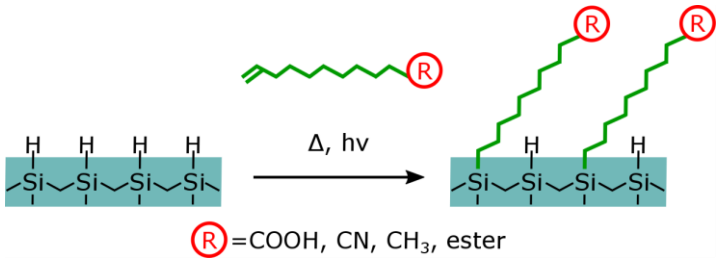


Figure 11: Scheme of the formation of organic monolayers through covalent Si-C bonds.

Linford et al. proposed a chain propagation reaction mechanism (see Figure 12) for the UV-induced grafting.[172] The UV light cleaves the Si-H and thereby creates a surface radical. This surface radical will attack the terminally unsaturated alkene, with the binding of the alkene by its α-carbon to the Si atom. This results in a radical on the grafted molecule on the β-carbon, which then removes a hydrogen atom at a neighboring SiH site, resulting in a new surface radical for further alkene attachment.[172]

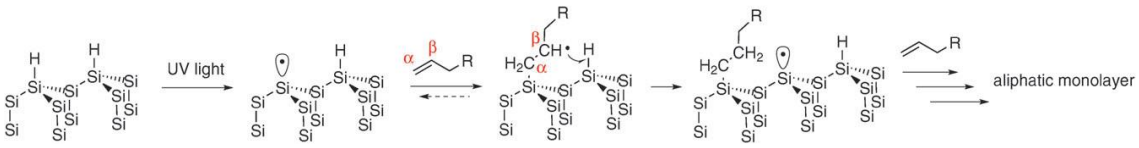


Figure 12: Reaction mechanism of UV-induced grafting of 1-alkenes on hydrogen terminated surfaces proposed by Linford and Chidsey.[177,184]

The grafting of organic monolayers on silicon surfaces is also possible by visible light. Stewart and Buriak introduced an alternative route for grafting on porous hydrogen terminated silicon under mild reaction conditions using white light.[185] They proposed a grafting mechanism, where the illumination with white light at moderate intensity creates relatively long-lived surface-localised excitons (electron-hole pairs).[186] The electron-hole pair is separated and results in a positive localised surface charge. The unsaturated alkene can then undergo a nucleophilic attack by the hole, yielding a carbon centred radical nucleophilic. This radical can bond a hydride, and neutralize the charge.[186,187] Later on Hamers found a way of grafting on crystalline silicon surfaces by temporarily terminating the silicon surface with iodine by exposure to 514 nm light.[188] The group of Zuilhof then found a method of grafting alkyl monolayers directly on crystalline silicon with visible light (447 nm) at room temperature.[189,190]

Wang et al. proposed that the reactions involved in grafting are based on the creation of a valence-band hole, which can be either created by an exciton mechanism or photoemission. In the exciton mechanism the light creates an electron-hole pair.[191,192] The valence-band hole can also be created by a photoemission reaction initiated by UV light, where an electron from the silicon surface is excited to an acceptor level of electron acceptors (which can include the reactant molecules), leaving a valence-band hole. The valence-band hole, created by either mechanism, can then induce a nucleophilic attack by the alkenes, resulting in a stable Si-C bond. The reaction mechanism is dependent on the wavelength of the light. At short wavelengths the photons excite the electrons to the electron-acceptor levels of the alkenes, resulting in more efficient photoemission despite the fact that both are possible.[192] At longer wavelengths the valence-band hole creation is likely limited to the exciton mechanism. Therefore the grafting mechanism is defined by the wavelength and the electronic structure of the molecules.

2.2.2 Two-step amidation of acid terminated surfaces

The acid-terminated surfaces are good candidates for the attachment of biomolecules in mild conditions by amide bonds. They can be immobilized on acid terminated

surfaces by first “activating” the acid groups on the surface with peptide coupling agents like carbodiimides[193], uronium[194,195] salts or phosphonium[196,197] salts. This activation then allows immobilization of functional groups with primary amines in “soft conditions” resulting in their stable immobilization.[198,199]

In the laboratory PMC the carbodiimide EDC was studied as a coupling agent, as it is water soluble (and therefore easy to handle and remove), non-toxic and relatively inexpensive. It is generally used with the succinimide NHS (N-hydroxysuccinimide) to form a stable intermediary, the ester of succinimidyl, which can react with amine groups to form stable amide bonds. The reaction mechanism has been extensively studied in solution.[193,200–202] The reaction mechanism on carboxylic acid-terminated surfaces is displayed in Figure 13.[18,19,203] In the first step the OH group of the surface acid reacts with one of the double bonds of EDC, resulting in the formation of O-acylurea (reaction 1). The O-acylurea will further react following three competitive reaction pathways: (i) direct reaction with NHS to form the ester-NHS product (reaction 2); (ii) reaction with a neighboring carboxyl group can form an anhydride product (reaction 3) which can then undergo further reaction with NHS resulting in an ester-NHS group on the surface (reaction 4); (iii) rearrangement of the O-acylurea via an intramolecular acyl transfer results in the formation of N-acylurea on the surface (reaction 5).

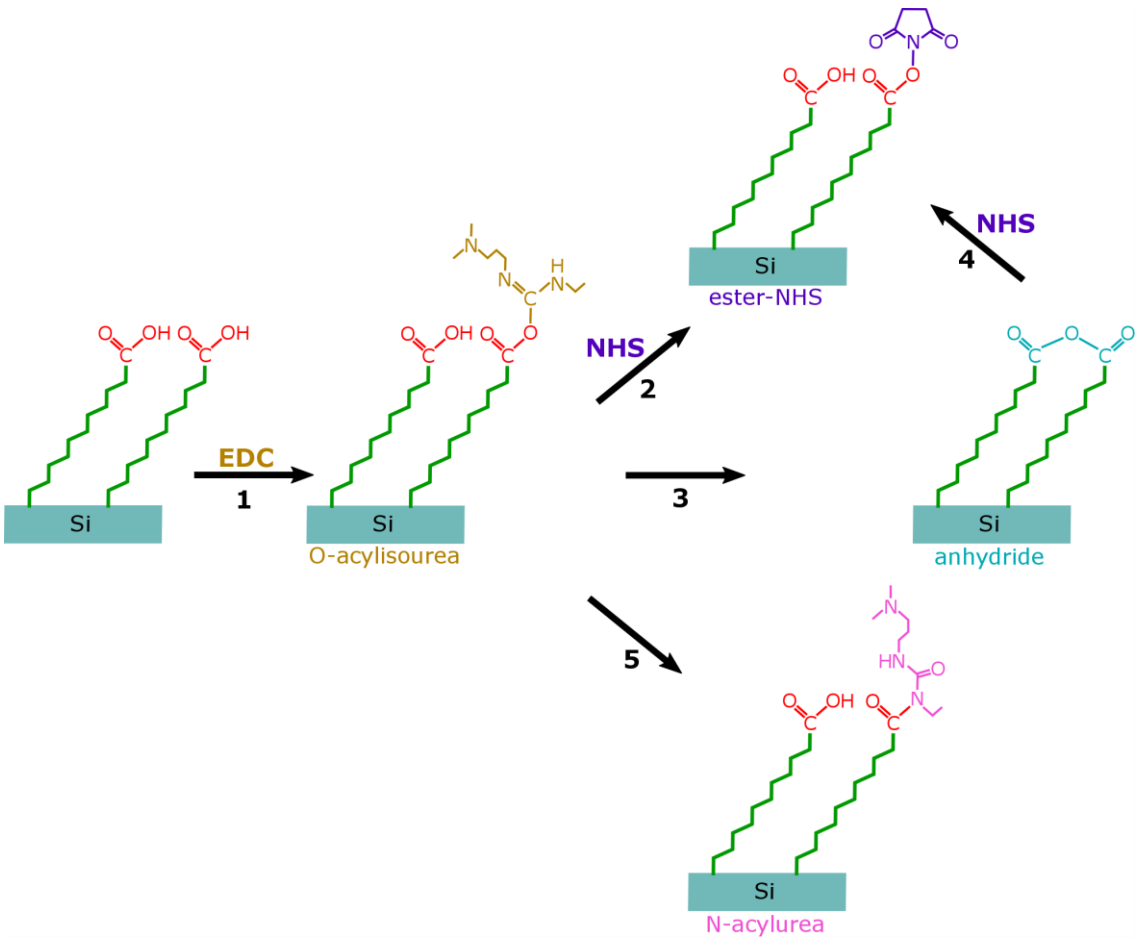


Figure 13: Scheme of the elementary activation reactions on carboxyl-terminated surfaces. In the first step (1) EDC reacts with surface acid groups to form O-acylisourea. Subsequently the two main pathways (reaction 2 and 3 or reaction 4) result in ester-NHS terminated surfaces, or alternatively (reaction 5) in N-acylurea groups on the surface.

Sam et al. showed that the concentration of EDC and NHS determines which of the three competitive reactions dominates, by testing a large series of concentrations and also by varying the ratio of EDC to NHS, including strong excess concentrations of either compound.[18] A strongly reduced activation yield with unreacted surface acid groups occurs, when large excess of NHS is used. Large excess of EDC on the other hand results in N-acylurea on the surface. When the concentrations of EDC and NHS are equal but higher than 10 mM the reaction also results in N-urea on the surface, while concentrations below 5 mM lead to anhydride on the surfaces. Therefore all activation reactions are carried out at 5 mM EDC and NHS. The reaction temperature

was also found to play a vital role. For temperatures under 5°C the reaction yield drops, while high temperatures (room temperature, 25°C) lead to urea forming on the surface. Touahir et al. reported activation yields of $\eta = 85 - 95\%$ in kinetic studies on atomically rough silicon surfaces.[203] The activation yield on atomically flat surfaces drops to $\eta = 60 - 80\%$. This difference is presumably due to steric hindrance because the acid layer exhibits a higher density on atomically flat SiH then on atomically rough SiH_X.

Ester-NHS activated silicon surfaces enable the immobilization of NH_2-terminated functional groups, by an aminolysis reaction.[193] During the aminolysis reaction the amine-terminated (bio)molecules react with the ester-NHS, forming an amide bond (see Figure 14). The molecule is then covalently bound to the organic layer, resulting in a strong and reliable immobilization. Moraillon et al. found that the pH of the amine solution plays a crucial role during the aminolysis reaction.[19] The pH of the amine solution must be lower than the pKa of the corresponding amine (<10) for the reaction to take place.

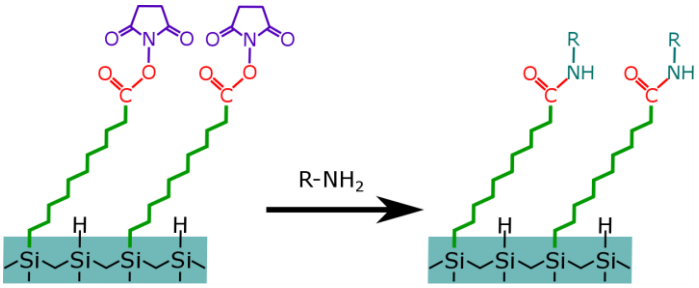


Figure 14: Schematic representation of aminolysis reaction on activated silicon surfaces.

This aminolysis reaction allows for example the stable immobilization of biological probes for sensors or the attachment of antifouling layers which can avoid unwanted non-specific adsorption (or fouling) of for example proteins and bacteria on surfaces, which are known for their strong tendency to adsorb on many surfaces.[182,204–206] We have chosen the well-known PEG (poly(ethylene glycol)) molecules as an example for

an anti-biofouling layer because of their excellent antifouling properties towards bacteria and proteins.[207] These layers can be immobilized by aminolysis. Unlike many other antifouling molecules it is commercially available and inexpensive, and is also non-toxic, non-immunogenic and non-antigenic. Specifically, the antifouling properties of methoxypoly(ethylene glycol)-amine (CH_3O-PEG-NH_2, Figure 15) with different chain lengths were compared.

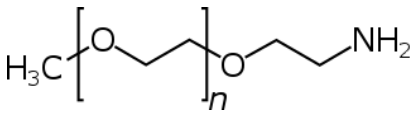


Figure 15: Chemical structure of Methoxy-PEG-amine.

2.3 Materials and Methods

2.3.1 Chemicals and substrates

In our experiments all chemicals were of reagent grade or higher and if not mentioned explicitly used without further purification. The cleaning agents (hydrogen peroxide, H_2O_2, 30%; sulfuric acid, H_2SO_4 96%; glacial acetic acid, CH_3COOH_2; absolute ethanol anhydrous EtOH) and etching agent (hydrofluoric acid, HF, 50%) were of RS grade and supplied by Carlo-Erba. Undecylenic acid (CH_2=CH(CH_2)$_8$COOH, 99%) was purchased from Acros Organics. The coupling agent EDC (N-(3-Dimethylaminopropyl)-N'-ethylcarbodiimide 98%) and the activating reagent NHS (N-Hydroxysuccinimide commercial grade) were purchased from Sigma Aldrich. PEG 750 methoxypoly(ethyleneglycol)-amine, (M_N = 750, n ≈ 15), PEG 2000 (M_N = 2000, n ≈ 44), and PEG 5000 (M_N = 5000, n ≈ 112) were supplied by Fluka Analytical. PBS 10X (Phosphate Buffered Saline) was supplied by Ambion, and SDS (Sodium dodecyl sulfate, 99%, molecular biology grade) by Sigma. Ultrapure water (MilliQ, 18.2 MΩ·cm, at 25°C) was used to prepare solutions and for rinsing.

The bacteria Escherichia coli Katushka (*E. coli*) K12 was kindly supplied by Julie Bouckaert and Sabine Szunerits of the Université de Lille 1.[208] It contains plasmids

which harbour three genes. One of the genes is for the production of the fluorescent protein Katushka (TurboFP635: excitation/emission maxima at 588/635 nm). The two other genes are for antibiotic resistance (towards kanamycin and chloramphenicol), to ensure plasmid replication.

The silicon samples were cleaved from double-side polished n-type silicon ((111), FZ, 30-40 Ωcm, Siltronix, France). To prepare the prisms for ATR-FTIR, the silicon pieces were polished on two opposite sites to have a bevel around 45°-47°.[209] The prism size was generally around 20x16x0.5 mm, resulting in up to 30 internal reflections.

The optical microscopy images were obtained with an Olympus BX51WI.

2.3.2 Hydrogenated silicon surfaces

The etching is conducted in two steps:

- Preliminary cleaning: the silicon wafer is immersed in Piranha solution at 100°C. The solution consists of a 1:3 mixture of H_2O_2 with H_2SO_4. This procedure is applied because Piranha solution is a strong oxidizing agent and removes all organic pollutions on the surface. Afterwards the wafer is very carefully rinsed with ultra-pure water to avoid any possible contaminations during the etching.
- HF-etching: Removal of oxide layer on silicon surfaces is done by immersing the sample for 5 seconds in a polytetrafluoroethylene (PTFE) beaker filled with 50% hydrofluoric acid solution. Afterwards the wafer is cleaned with ultra-pure water and dried in a flow of N_2 before further handling.

2.3.3 Photochemical hydrosilylation of undecylenic acid

Undecylenic acid is outgassed under argon in a Schlenk tube at 100°C for 30 minutes and then cooled to room temperature. The freshly HF-etched silicon sample is then transferred into the Schlenk tube with continuous argon bubbling for 15 min. The Schlenk is closed hermetically and irradiated for 3 h in a UV reactor (6 mW cm^{-2},

312 nm). The functionalized surface is finally cleaned twice with glacial acetic acid under argon bubbling at 75°C for 15 min in a Schlenk tube and subsequently in a beaker with acetic acid for 5 min. The rinse is continued for 10 min with PBS 1X/0.1% SDS, before the sample is rinsed with ultrapure MilliQ water and dried under N_2.

2.3.4 Activation with EDC/NHS of acid-terminated surfaces

Two solutions of 10 mM EDC and NHS are separately prepared in ultrapure MilliQ water at 0°C. A Schlenk tube is immersed in a water bath with a temperature between 15 and 18°C. An equal volume of EDC and NHS are added into the Schlenk and flushed with argon for 10 min before adding the acid terminated silicon surface. For 90 min the Schlenk tube with the sample is bubbled with argon, while the temperature is controlled to remain in the range mentioned above. Next the sample is cleaned for 5 min in a beaker with MilliQ water, then rinsed copiously with MilliQ water and dried under a nitrogen flow.

2.3.5 Aminolysis of PEG 750 on activated silicon surfaces

PEG 750 is dissolved at a concentration of 20 mM in PBS 1X, the pH is adjusted to 8.5. The solution is then bubbled in a Schlenk with argon for 5 min, before the freshly activated sample is added. The argon bubbling is continued for 10 more minutes before the valves of the Schlenk are closed. After 16 h (overnight) the sample is cleaned 1 min with PBS 1X, 10 min with PBS 1X/0.1% SDS, 1 min PBS 0.2X, 1 min PBS 0.1X. A final short rinse in ultrapure water is conducted to remove the buffer solution before drying the sample under a flow of nitrogen.

2.3.6 Adsorption test of *E. coli* Katushka K12 on PEG-surfaces

The support used for the adsorption-studies of *E. coli* on PEG-surfaces was a glass slide with a 250 nm layer of aluminium and a 44 nm layer of amorphous silicon carbon (a-$Si_{1-X}C_X$:H) deposited by PVD and PECVD, respectively. The a-$Si_{1-X}C_X$:H-layer is used as a basis for photochemical hydrosilylation and activation with EDC/NHS. Further details on these supports are described in chapter 5. Three zones are subjected to a treatment with drops (V = 175 µl) of 50 mM PEG solutions (PEG 750, PEG 2000 and PEG 5000) in ultrapure water at pH 8.5. After one hour the three drops of PEG are removed and carefully rinsed with 3 x 1 ml PBS 1X, followed by a quick rinse in ultrapure water. The slide is dried in a centrifuge before further handling. Then 250 µl of *E. coli* Katushka K12 in PBS 1X ($6.93 \cdot 10^8$ cfu/ml) are added per zone (zones are separated by adhesive incubation chambers), and let for 2 hours. The zones are carefully rinsed three times with PBS 1X, before drying in a centrifuge.

2.4 Results and discussion

2.4.1 Hydrogenation of silicon surfaces

The removal of the native oxide layer of Si (111) by HF-etching was observed by ATR-FTIR. Figure 16 shows the infrared spectra of an H-terminated silicon surface after HF-etching in p- and s-polarization, with the reference being the clean oxidized silicon surface before etching. There are several overlapping negative peaks visible in the region 900 – 1350 cm^{-1}. A triplet of small positive peaks is also visible in the region 2050 – 2150 cm^{-1}. Negative peaks correspond to a loss, while positive peaks indicate a gain of compounds on the surface.

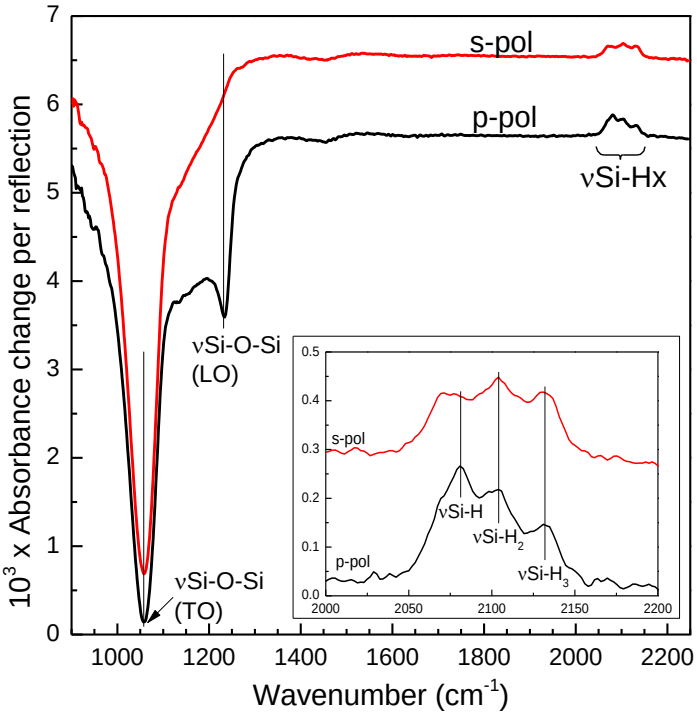


Figure 16: ATR-FTIR spectra of H-terminated silicon surface in s-polarization (red) and p-polarization (black). The inset shows enlarged the region of $\nu Si\text{-}H_X$. The reference spectra are the oxidized silicon surfaces (SiO_X) before etching.

The negative bands (900 – 1350 cm^{-1}) correspond to the vibrational modes of $Si\text{-}O_X$. The transverse optical (TO) Si-O-Si vibration is clearly visible for both polarisations at 1060 cm^{-1}, while the longitudinal phonon optical (LO) vibration is only visible in the p-polarization.[210,211] The triplet of positive bands in the region 2050 – 2150 cm^{-1} corresponds to hydride bonds ($Si\text{-}H_X$) formation. Three forms of hydrogenated silicon are visible: monohydride Si-H at ~2080 cm^{-1}, dihydride $Si\text{-}H_2$ at 2105 cm^{-1} and trihydride $Si\text{-}H_3$ at 2130 cm^{-1}.[212]

The intense negative $Si\text{-}O_X$ and the positive SiH_X bands show that the HF-etching removed oxidized silicon, and formed a hydrogenated silicon surface. The fact that all three hydrides are visible in both polarizations indicates a rough hydrogenated surface.

2.4.2 Grafting of undecylenic acid on silicon surfaces by hydrosilylation

The hydrogenated surface was modified by photochemical hydrosilylation of undecylenic acid. The corresponding ATR-FTIR spectra in p- and s-polarization are displayed on the left in Figure 17, the reference spectra being the hydrogenated silicon surfaces. Three negative peaks are visible in the region 2050 – 2150 cm^{-1}, which correspond to the loss of SiH_X bonds. The bands at 2930 and 2850 cm^{-1} can be associated with antisymmetric CH_2 (ν_a) and symmetric CH_2 (ν_s) modes, respectively. The large peak at 1715 cm^{-1} (peak height 0.7 mAbs) arises from the stretching mode vibration of the carboxyl C=O bond. The small peak at 1465 cm^{-1} is assigned to the deformation of CH_2 in the H-C-H plane, while the peak at 1410 cm^{-1} stems from the vibrations of the C-OH group. [17] The presence of the vibrations which are associated with the different bonds of undecylenic acid confirms the surface functionalization.

The region between 1000 and 1300 cm^{-1} is characteristic for the oxide bonds of silicon, like Si-O-Si. The low oxidation of the sample by the process of photochemical hydrosilylation is displayed by the low intensity of the oxide bands, which can be seen more clearly when compared with the intensity of the oxide bands removed after HF-etching (5.5 mAbs at 1050 cm^{-1} in Figure 16). By integrating and comparing the spectrum of HF-etching and hydrosilylation in the region 900 – 1350 cm^{-2} in s-polarization, one can estimate that the sample's oxidation after hydrosilylation is about 5% of what had been removed by etching.[19]

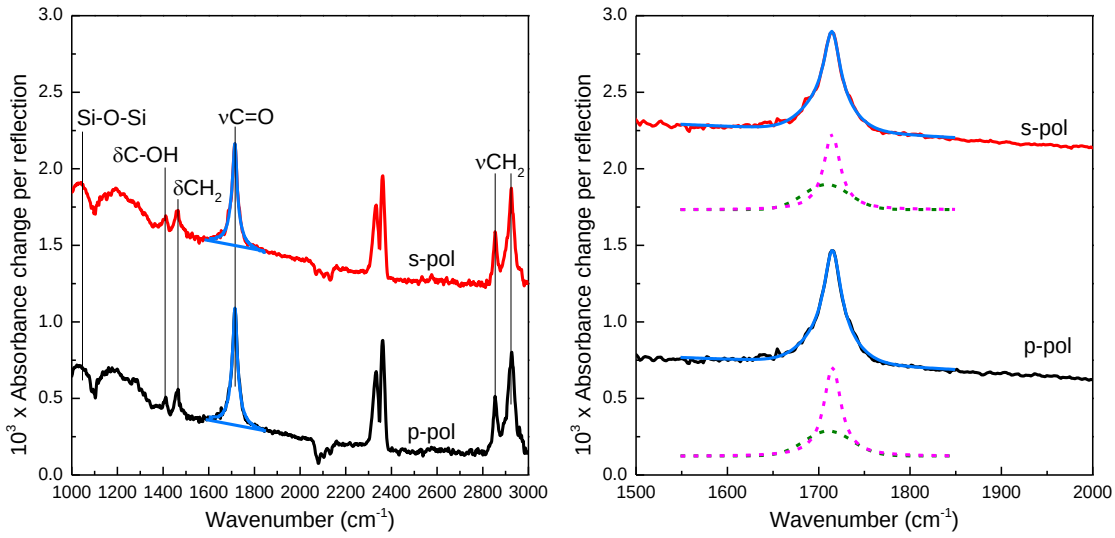


Figure 17: Left side: ATR-FTIR spectra of silicon surface functionalized with undecylenic acid, in s-polarization (red) and p-polarization (black). The blue curves show the fits for quantitative analysis. The reference spectra are H-terminated silicon surfaces (SiH_X). Right side: deconvolution of the fits.

A quantitative determination of the surface coverage has been conducted from the analysis of the C=O band, as shown by Faucheux et al. (cf. Annex I).[17] For this the IR-spectra are fitted (right side in Figure 17) with a Gauss (~1705 cm^{-1}, FWHM ~ 70 cm^{-1}) and a Lorentz (~1715 cm^{-1}, FWHM ~ 25 cm^{-1}) curve. The peak which is fitted at 1715 cm^{-1} has only one vibrating contribution (C=O), therefore normally a single peak would be fitted for the quantitative analysis. Nevertheless the method of fitting two peaks with different profiles was established, as using the sum of the two integrated absorbances yields the best results.[17] The sum of the integrated intensities of the fitted curves in s- and p-polarization ($A_S = 2.7 \cdot 10^{-3} cm^{-1}$ and $A_P = 3.1 \cdot 10^{-3} cm^{-1}$) then yields the surface density of $N_{CO} = 2.5 \cdot 10^{14} cm^{-2}$. In order to calculate the surface coverage the number of hydrogenated atoms on flat SiH surfaces ($N_{Si} = 7.83 \cdot 10^{14} cm^{-2}$) is taken as reference for the maximum number of possible binding sites. Our experiments are carried out on atomically rough SiH_X surfaces which exhibit a higher number of possible binding sites, but a reliable number cannot be given due to its relative inhomogeneity. With this we obtained a surface coverage of $\theta = \frac{N_{CO}}{N_{Si}} = \frac{2.5 \cdot 10^{14} cm^{-2}}{7.8 \cdot 10^{14} cm^{-2}} = 32\%$. During all the experiments conducted, the surface density

generally varied from 1.6 – 2.5·10^{14} cm^{-2} ($\theta = 20 - 32\%$), indicating relatively reliable and reproducible grafting of 1-alkenes. The group of Sieval showed that a 100% surface coverage with alkyl chains is not possible due to steric hindrance from the tilt angle and the diameter of the chain. They calculated that about 50% of the surface silicon SiH sites can be used for the binding.[213] Experimentally, Faucheux showed that the achievable surface density on atomically flat silicon surfaces (prepared by etching in NH_4F) is 2.7·10^{14} cm^{-2}, corresponding to a relatively dense surface coverage of $\theta = 35\%$.[17] The reduced surface density on our surfaces probably stems from the atomic roughness of the sample.

2.4.3 Activation with EDC/NHS of acid-terminated surfaces

The activation reaction of the carboxyl-terminated alkyl chains grafted on silicon was conducted with EDC/NHS and was characterized and quantified by ATR-FTIR. The infrared spectrum in s- and p-polarization of such a surface is displayed on the left in Figure 18. The reference spectra are again the hydrogenated silicon surfaces. As before, a triplet of negative peaks is visible in the region of 2050 – 2150 cm^{-1}, confirming the loss of SiH_X bands. The two positive bands at 2930 and 2850 cm^{-1} are associated with the CH_2 modes of the alkyl chain. Compared with the acid terminated surface the two characteristic bands of the alkyl chain (2930 and 2850 cm^{-1}) remain at the same intensity, indicating neither addition nor removal of the acid layer.

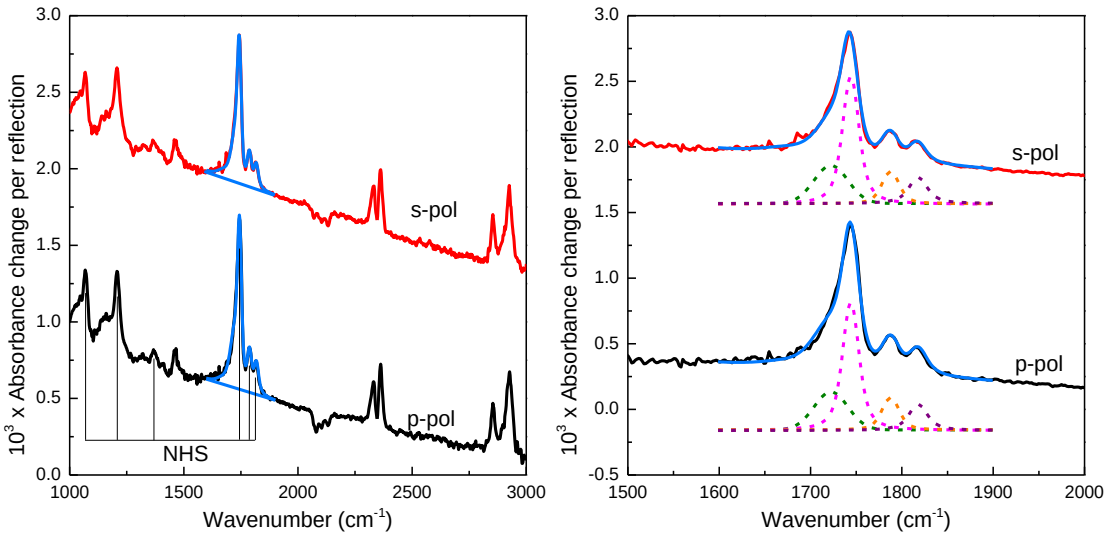


Figure 18: Left side: ATR-FTIR spectra of silicon surface activated with EDC/NHS, in s-polarization (red) and p-polarization (black). The blue curves show the fits for quantitative analysis. The reference spectra are the H-terminated silicon surfaces (SiH_X). Right side: deconvolution of the fits.

The triplet of peaks at 1819, 1788 and 1745 cm^{-1} is characteristic for the carbonyl of the ester-NHS. The mode at 1819 cm^{-1} corresponds to the νC=O stretch of the ester, while the 1788 and 1745 cm^{-1} modes are associated with the symmetric and antisymmetric vibrational modes νC=O of the carbonyl groups of the succinimidyl cycle. The peaks at 1370 and 1208 cm^{-1} are associated with the succinimidyl cycle's symmetric and antisymmetric νC-N-C modes. The band at 1065 is assigned to the succinimidyl's νC-N-O mode.[203,214] The bands found in the spectrum agree with the peaks expected by the formation of ester-NHS on the surface.

The surface density of the ester-NHS groups on the surface was determined by the quantitative analysis of the fits of the two peaks at 1788 and 1819 cm^{-1} with a procedure described by Moraillon et al. (cf. Annex I).[19] In this procedure the remaining acid peak at 1725 cm^{-1} is fitted with a Gauss curve (FWHM ≈ 45 cm^{-1}), while the three ester-NHS peak peaks at 1740 (FWHM ≈ 20 cm^{-1}), 1788 (FWHM ≈ 21 cm^{-1}) and 1818 cm^{-1} (FWHM ≈ 23 cm^{-1}) are fitted with a Voigt profile (convolution of Gaussian and Lorentzian profile). The integrated intensities of these fits are displayed in Table 3. With these values the ester-NHS surface density of the sample shown in Figure 18 was

calculated to be $N_{NHS} = 2.1 \cdot 10^{14}\ cm^{-2}$. As the surface density of the carboxyl groups was determined before to be $N_{CO} = 2.5 \cdot 10^{14}\ cm^{-2}$, this corresponds to a yield $\eta = \frac{N_{NHS}}{N_{CO}} = \frac{2.1 \cdot 10^{14}}{2.5 \cdot 10^{14}} = 84\%$ of activated carboxyl groups, or a surface coverage of $\theta = 27\%$. From this we can also calculate the surface density of the unreacted remaining acid groups to be $N_{CO,remaining} = N_{CO} - N_{NHS} = 0.4 \cdot 10^{14}\ cm^{-2}$. The ester-NHS surface density varied from 1.7 – 2.1·10^{14} cm^{-2} during the conducted experiments, depending mainly on the surface density of grafted undecylenic acid. This indicates a reliable and reproducible activation process of carboxyl terminated alkene chains on silicon surfaces.

Table 3: Integrated intensities (cm^{-1}) of the fits in Figure 18 for quantification of ester-NHS surface density.

Remaining acid vC=O stretching		**Ester-NHS** vC=O antisymmetric vibration		**Ester-NHS** vC=O symmetric vibration		**Ester-NHS** vC=O stretching	
$A_{1725,P}$	$A_{1725,S}$	$A_{1740,P}$	$A_{1740,S}$	$A_{1788,P}$	$A_{1788,S}$	$A_{1819,P}$	$A_{1819,S}$
0.0076	0.0072	0.0234	0.0205	0.0045	0.0036	0.0044	0.0037

2.4.4 Aminolysis of an activated silicon surface with PEG 750

PEG was chosen as a proof of principle for the immobilization of NH_2-terminated molecules on activated surfaces. CH_3O-PEG750-NH_2 (with n=15 ethyleneglycol moieties) was immobilized on an ester-NHS activated silicon surface by an aminolysis reaction. The infrared spectra after aminolysis are displayed in Figure 19, the reference spectra being the SiH_X surfaces.

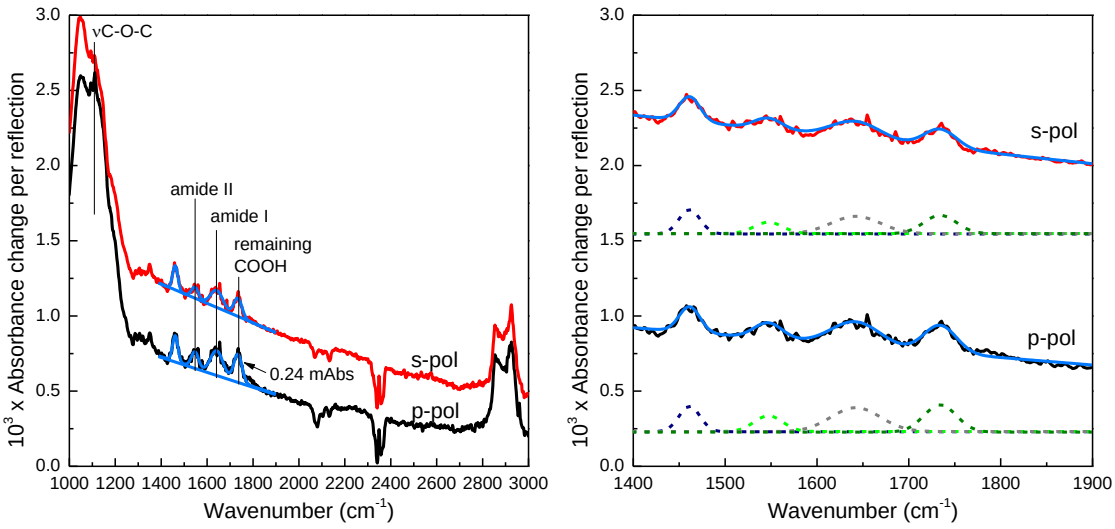


Figure 19: Left side: ATR-FTIR spectra of silicon surface after aminolysis with PEG750, in s-polarization (red) and p-polarization (black). The blue curves show the fits that were used for quantitative analysis. The reference spectra are the H-terminated silicon surfaces (SiH_X). Right side: deconvolution of the fits.

Compared to the spectra after the activation reaction the ester-NHS triplet disappears. Two new bands at 1640 and 1545 cm^{-1} appear, corresponding to vCO (amide I) and vCNH (amide II), respectively. The appearance of these two bands confirms the successful aminolysis of the activated surface with PEG. The peaks in the region 2860 – 2925 cm^{-1} are associated with the $vOCH_X$ and vCH_X modes of the alkyl and the PEG chains. The bands in the region 1000 – 1200 cm^{-1} can be associated to the vC-O-C mode, which also stem from the PEG chain.

Some acid remains visible in the spectrum with the carboxyl C=O bond at 1735 cm^{-1}. The shift of the acid peak, in comparison to the carboxyl-terminated surface, stems from the reduced interaction between the carboxyl groups. The remaining acid already visually indicates that the aminolysis reaction probably did not take place on all available ester-NHS sites and that unreacted ester-NHS was hydrolysed into acid.

The fits for quantitative analysis are displayed on the right side. All peaks are fitted with a Gaussian profile. The acid peak is fitted at 1735 cm^{-1} (FWHM ~ 40 cm^{-1}), and the amide I and amide II are fitted at 1643 cm^{-1} (FWHM ~ 60 cm^{-1}) and 1547 cm^{-1} (FWHM ~ 40 cm^{-1}), respectively. The calculated intensities for the remaining acid peaks in s- and

p-polarization are $A_S = 4.7 \cdot 10^{-3}\,cm^1$ and $A_P = 8.1 \cdot 10^{-3}\,cm^1$. With these intensities the surface density of the remaining acid was determined to be $N'_{CO} = 0.8 \cdot 10^{14}\,cm^2$. After the activation reaction, the surface density of remaining acid was $N_{CO,remaining} = 0.4 \cdot 10^{14}\,cm^{-2}$. Comparing the surface densities of remaining acid after activation and after aminolysis shows that $0.4 \cdot 10^{14}\,cm^{-2}$ (= $N'_{CO} - N_{CO,remaining}$) of the ester-NHS was removed by hydrolysis during the aminolysis reaction. The surface density of the PEG 750 is calculated with $N_{PEG} = N_{CO} - N'_{CO} = 1.7 \cdot 10^{14}\,cm^2$, and corresponds to a surface coverage $\theta = 21\%$ with a yield of $\eta = \frac{N_{PEG}}{N_{CO}} = \frac{1.6 \cdot 10^{14}}{2.5 \cdot 10^{14}} = 64\%$. The surface density varied from 0.8 – 1.6·10^{14} cm^{-2} during the conducted experiments, depending strongly on the surface density of grafted undecylenic acid and ester-NHS, but also on the reaction conditions (buffer solution and reaction time).

2.4.5 Adsorption test of *E. coli* Katushka K12 on PEG-surfaces

PEG is often used in order to avoid bio-adhesion. The anti-biofouling behavior of PEG stems from its hydrophilicity, resulting in a remaining thin layer of water between the PEG and the potential adsorbent.[207] The anti-biofouling properties of PEG on surfaces depends mainly on chain length and surface density.[153,207] Longer PEG chains and denser surfaces resist bacterial adsorption better. Therefore we decided to qualitatively study the anti-biofouling behavior of three different PEG chain lengths (PEG 750, PEG 2000 and PEG 5000) immobilized on silicon surfaces. For this the adsorption of the *E. coli* Katushka strand K12 on the PEG surfaces was examined with a fluorescence scanner and an optical microscope.

The surfaces for PEG immobilization are based on an amorphous silicon carbon alloy deposited on an aluminium back-reflector on glass slides for fluorescence measurements, as described in more detail in chapter 5. The surface functionalization of these slides is carried out in the same way as on crystalline silicon, except for the HF-etching which is done with HF-vapor instead of HF-solution. The PEG chains are

immobilized locally on the ester-NHS surface by applying drops (V = 175 µl) of 50 mM PEG solutions for one hour with subsequent rinsing.

The images of the interaction of the bacteria with three different PEG-surfaces (PEG 750, PEG 2000 and PEG 5000) are displayed in Figure 20. The areas where PEG is immobilized on the surface are marked with “P”, the areas where adsorption of bacteria is visible is marked with “B”. Both types of images (fluorescence and regular optical microscopy) show distinctive differences between the area where PEG was and was not immobilized. The optical microscopy shows no adsorption of bacteria on PEG, while fluorescence images display a few bacteria on PEG. The cross-section of the fluorescence images shows a very flat baseline in the region where PEG was attached, except for some small peaks indicating very few adsorbed bacteria. A preliminary qualitative analysis of the images suggested better antifouling properties for the longer PEG chains. Nevertheless PEG 750 displays adequate antifouling behavior. These results show a promising behavior of the PEG surfaces to avoid non-specific adsorption of bacteria, and for their application in biosensors for the detection of bacteria.

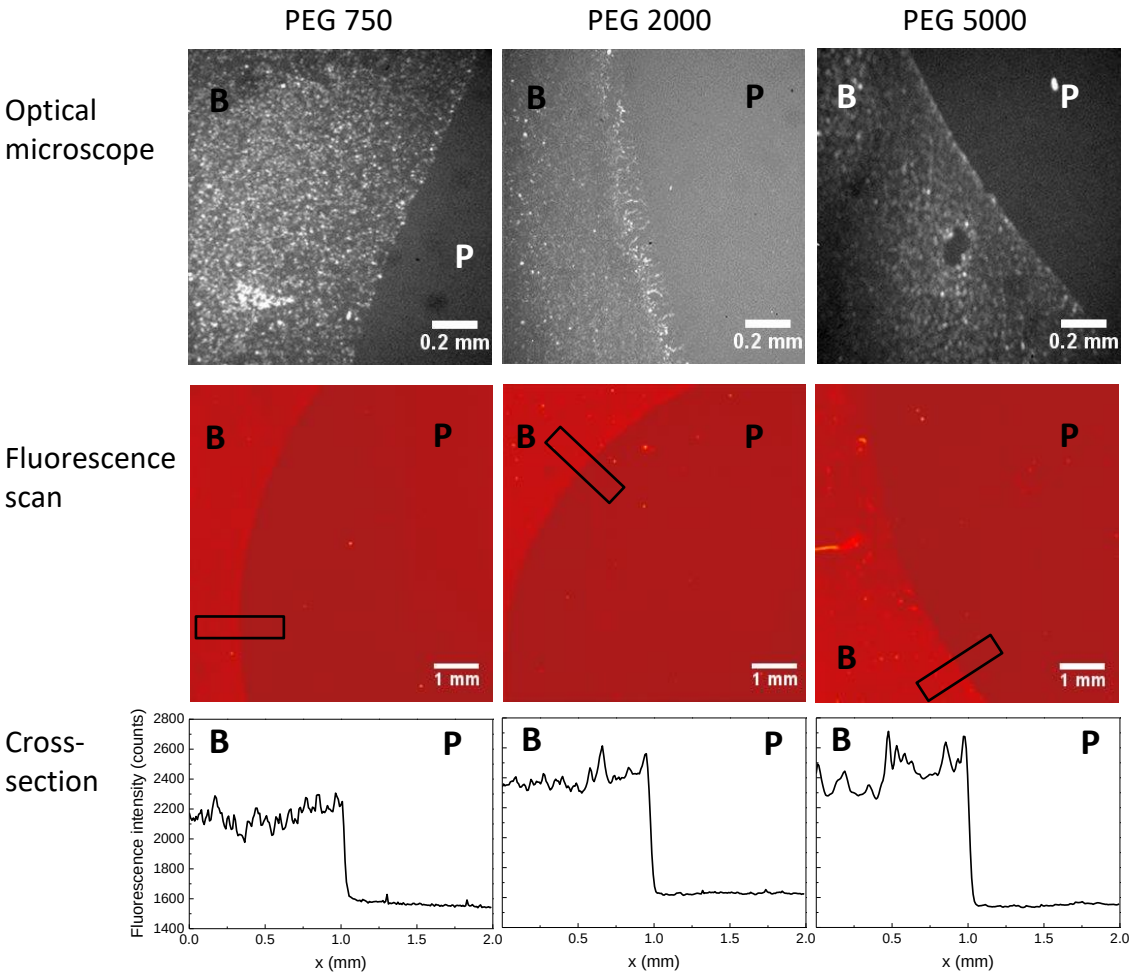


Figure 20: Microscopy and fluorescence images (5x) of bacteria on different PEG surfaces. The letter "B" marks the area where the bacteria are adsorbed, "P" shows the area where PEG was immobilized. Cross-section shows fluorescence intensity of the black square.

2.5 Conclusion

In this chapter we presented in detail the step-by-step functionalization of silicon surfaces for the immobilization of NH_2-terminated functional groups, in particular as an example PEG-NH_2 was immobilized to create an anti-biofouling surface. The oxide layer of silicon substrates was removed by HF etching. This enabled the grafting of undecylenic acid by photochemical hydrosilylation, leading to an organic carboxyl-terminated organic monolayer, attached by covalent Si-C bounds with a fairly dense surface density of $N_{CO} = 2.5 \cdot 10^{14} cm^{-2}$ and a surface coverage of $\theta = 32\%$. The next step consisted of activating the surface with EDC/NHS, which resulted in ester-NHS groups on the surface, which in turn undergo an aminolysis reaction and are thereby replaced by amine-terminated (bio)molecules, like PEG or aptamers. PEG-molecules were successfully immobilized on ester-NHS terminated monolayers. A quantitative analysis of the remaining acid on the surface allows calculating the surface density of PEG-chains on the surface of $\mathrm{N_{PEG}} = 1.7 \cdot 10^{14}\ \mathrm{cm}^2$, with a reaction yield of $\eta = 64\%$. The anti-biofouling property of three different PEG-surfaces (PEG 750, PEG 2000 and PEG 5000), towards *E. coli* Katushka K12 was shown qualitatively by fluorescence and regular optical microscopy. All three PEG- surfaces showed promising anti-biofouling behavior.

This well-controlled chemistry will be used for the elaboration of a bioassay based on immobilized aptamers for the detection of the toxin OTA. Nevertheless, before looking closer at the amidation of aptamers and the interaction of the aptamer with its target, it is necessary to better understand the nature of OTA.

3 Characterization of Ochratoxin A in Physiological Buffer Solutions

3.1 Introduction

The toxin OTA is a relatively small molecule with a surprisingly complex structure consisting of a chlorinated dihydroisocoumarin group linked on its 7-carboxyl with an amide to L-β-phenylalanine. Figure 21 shows the chemical structure of OTA in various states, which is known to change when the pH of the medium changes.[215,216] OTA is a colorless to white crystalline compound and possesses two pKa from the carbonyl group (pKa = 4.2 - 4.4) and the phenol hydroxyl group (pKa = 7.0 - 7.3).[217,218] The expected deprotonation by increasing pH is also accompanied by a ring-opening of the lactone group in alkaline conditions (pH>8).[215] OTA is fluorescent under UV light, and the pH of the solution also influences strongly its fluorescent characteristics. Moreover a shift of the absorbance peak is observed when the structure changes with the pH from 333 nm at pH 4 to 385 nm at pH 12.[216]

The solubility of OTA depends strongly on the solvent solution and its pH. It is readily soluble in polar organic solvents. In aqueous solutions it is only slightly soluble at acid and neutral pH, while being generally soluble in alkaline conditions.[219] Normally OTA is provided as a powder which is dissolved in a polar solvent like methanol, ethanol, etc. before further processing.[54,118,130,220]

Before studying the interaction of OTA with its aptamer grafted on silicon, we studied OTA in physiological buffer solutions in order to see the influence of the buffer solutions on the IR-spectrum of OTA, and thereby be able to identify OTA on surfaces after interacting with its aptamer. In-situ IR-calibration measurements enable the quantification of OTA on surfaces.

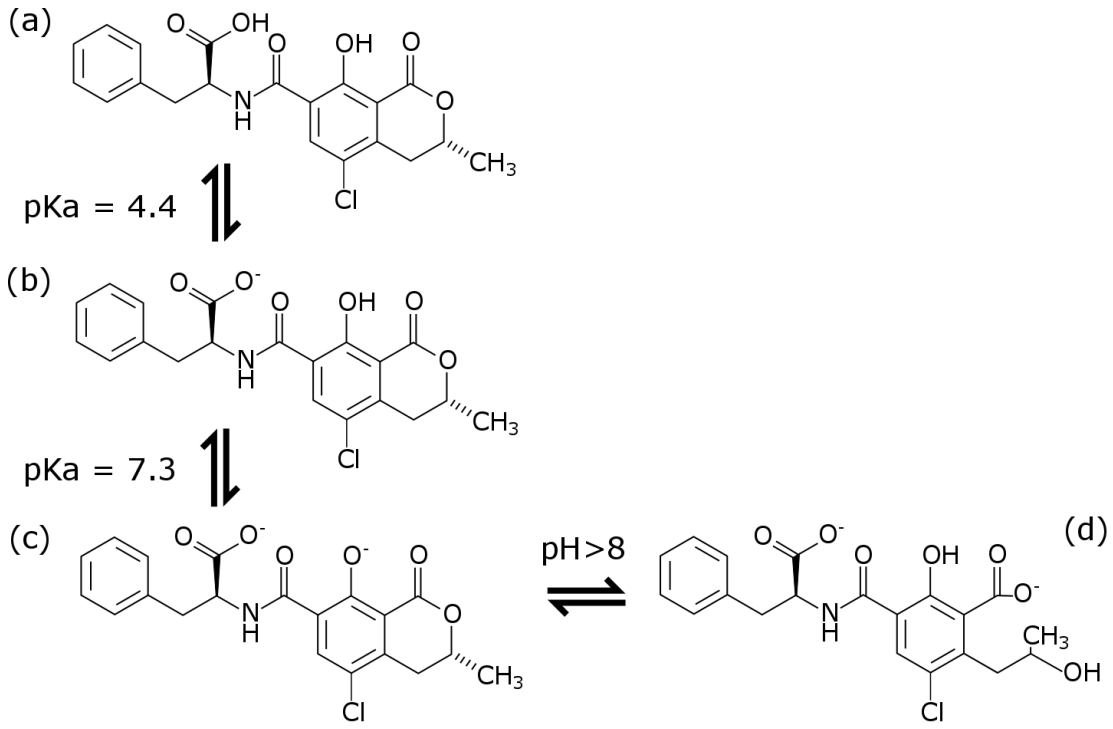


Figure 21: Chemical structure of OTA, dependent on pH; (a) acidic or dry conditions; (b) slightly basic conditions; (c) basic conditions; (d) strong basic conditions.

In order to identify OTA on surfaces after the interaction with its aptamer, we analyze the relation of OTA-structure to infrared response and to UV-vis absorption. Therefore, in a first approach the IR-in-situ measurement is conducted in methanol, where OTA is readily soluble and easy to handle. Subsequently the medium is changed to 35% ethanol in water at pH 8.5, approaching the buffer used during the interaction of OTA with its aptamer. The final IR-studies are conducted in aqueous media at different pH, which is physiologically closest to the buffer solution used for the interaction of OTA - aptamer. An IR in-situ-measurement will be carried out to calibrate the effective OTA IR-cross section to OTA concentration in solutions. The analysis of the IR-spectra is partially based on preliminary DFT calculations conducted by Professor Gilles Frison of the Laboratoire de Chimie Moléculaire (LCM), Ecole Polytechnique.

The influence of different physiological (methanol, H_2O at different pH) solutions on the structure is also studied by UV-vis spectroscopy. A calibration study is carried out with UV-vis spectroscopy, relating the OTA UV-vis absorption to its concentration in a physiological buffer solution.

3.2 Materials and methods

3.2.1 Chemicals and substrates

In our experiments all chemicals were reagent grade or higher and used without further purification. OTA ($C_{20}H_{18}ClNO_6$) from *Aspergillus ochraceus* was purchased from Sigma Aldrich in reference grade. The solvents (absolute ethanol anhydrous RS grade; methanol RE grade) were supplied by Sigma Aldrich. TRIS (Tris(hydroxymethyl)aminomethane, $NH_2C(CH_2HO)_3$, molecular biology grade) was purchased from Research Organics; EDTA (Ethylenediaminetetraacetic acid, 99% titration) was supplied by Sigma Aldrich. PBS 10X (Phosphate Buffered Saline) was supplied by Ambion, and SDS (Sodium dodecyl sulfate, 99%, molecular biology grade) by Sigma. Ultrapure water (MilliQ, 18.2 MΩ·cm, at 25°C) was used to prepare solutions and for rinsing.

3.2.2 Preparation of OTA-solutions for in-situ IR spectroscopy

In-situ infrared spectroscopy was performed with an in-house built PTFE in-situ cell (V_{min} = 0.5 ml; cf. annex).

OTA in methanol: A solution of 20 mM OTA in methanol was prepared.

OTA in 35% EtOH, pH 8.5: A solution of 34.7 mM OTA in ethanol was prepared, before dilution to 8 mM OTA in 35% ethanol in ultrapure water and the pH was then adjusted with 1 M NaOH until a value of 8.5 was reached.

OTA in water, pH 8.5: An OTA solution in ultrapure water was prepared at a concentration of 25 mM, and the pH was adjusted until 8.5 with 1 M NaOH. The in-situ IR measurements were conducted with dilutions in cascade steps of 5 mM down to a concentration of 5 mM.

OTA in water, pH 7 and pH 11: The solution was prepared at an OTA concentration of 20 mM in ultrapure water and the pH was adjusted with 1 M NaOH to the value 7 and afterwards to pH 11.

3.2.3 Preparation of OTA-solutions for UV-vis spectroscopy

The spectrometry was conducted with a glass reservoir containing 1 ml of each solution, the reference spectra were identical solutions without OTA in the same reservoirs.

OTA in methanol, water pH 7, pH 8.5, pH 11: OTA solutions were prepared at a concentration of 5 µM OTA in methanol or ultrapure water. In case of water, the pH was adjusted with 1 M NaOH, until the wanted pH was reached.

OTA in regeneration buffer: The OTA solutions were diluted from OTA stock solution (25 mM in H_2O, pH8.5) for concentrations between 1 µM and 0.05 µM in regeneration buffer (methanol/(10 mM TRIS, 1 mM EDTA, pH 9) (20:80, v/v)).

3.3 Results and discussion

3.3.1 The relation of OTA-structure with IR response and UV-vis absorption

3.3.1.1 In-situ IR spectroscopy of OTA in different media

(A) OTA in methanol

The in-situ IR-measurement of 20 mM OTA in methanol is displayed in Figure 22 (dark green), with the reference spectrum being the in-situ spectrum of pure methanol. There are a number of bands visible in the region 1200 – 1800 cm^{-1} which constitute the IR-fingerprint of OTA in methanol. The light green curve in the figure displays the DFT calculation of OTA in its form (a), implicitly taking into account the effect of Methanol as a solvent.

Bredenkamp et al. discuss in their publication from 1989 the assignment of IR-peaks for the region 1500 – 1800 cm^{-1}.[221] They associate the peak at 1725 cm^{-1} with the vibrations of OTAs carboxylic acid group, while the intense peak at 1680 cm^{-1} stems from the lactone (cyclic ester of hydroxycarboxylic acid). The peak at 1645 cm^{-1} can be associated with the amide I vibrations of the amide bond. The last contribution in this

band of peaks at 1610 cm^{-1} stems from aromatic breathing of the benzene rings. The peak at 1540 cm^{-1} is associated with the amide II.

The DFT calculation for OTA shows a strong resemblance to the spectra obtained by in-situ IR. Further comparison also shows strong agreement for the peak assignments. The carboxylic acid peak is slightly shifted in the calculation. In contrary to the IR spectrum the amide I and lactone bands overlap in the calculation. Furthermore the peak at 1610 cm^{-1} is found to be rather from the CC and COH of the phenol group than from aromatic breathing. The DFT calculation also enables the assignment for the bands at wavelengths under 1500 cm^{-1}. The band at 1425 cm^{-1} is from a decoupled phenol mode (CC, βCH, COH, HCH), and the peak at 1392 cm^{-1} is assigned to the symmetric deformation (umbrella) mode of CH_3. The band at 1216 cm^{-1} stems from the deformation mode of phenol and lactone and amide III modes.

OTA in methanol is in its structure (a) (see Figure 21), as the COOH modes are clearly visible in the IR-spectrum.

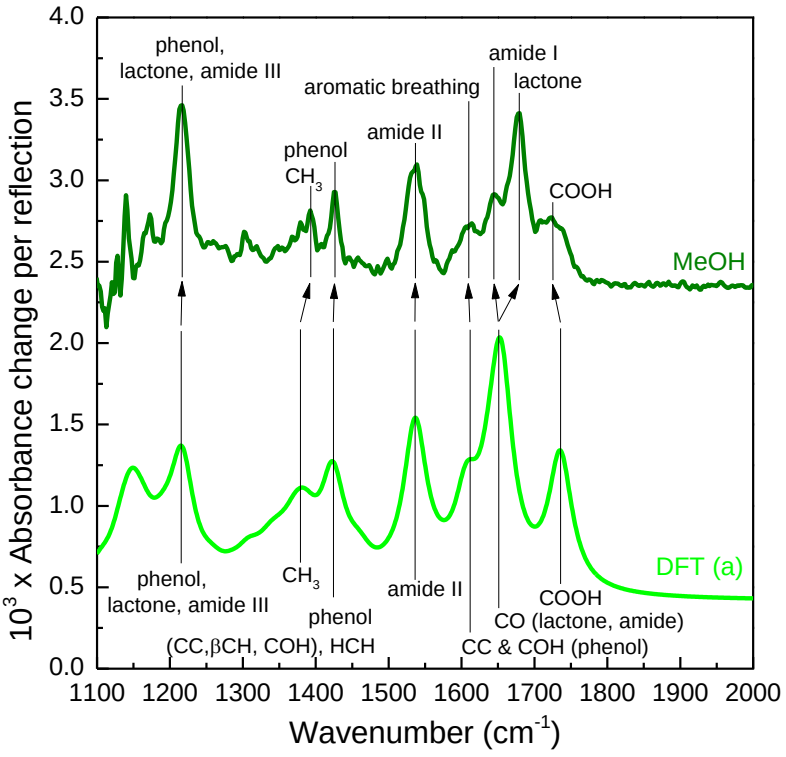


Figure 22: Dark green: in-situ IR-spectra (s-polarization) of 20 mM OTA dissolved in methanol in s-polarization, the reference spectrum being pure methanol. Light green: DFT calculation of OTA in its form (a) in Methanol.

(B) OTA in aqueous solution at different pH

OTA can be dissolved in water if the pH is adjusted accordingly to alkaline conditions. As already mentioned, the chemical structure of OTA changes with the pH. In order to be as close as possible to the interaction conditions (interaction OTA-aptamer) and to study the structural changes which OTA undergoes with a changing pH, the pH was first adjusted to pH 7 (Figure 23), and in a next step to pH 8.5 and pH 11 (Figure 24).

The in-situ IR spectra in Figure 23 show OTA at a concentration of 20 mM in water at pH 7 (black line) and 20 mM in methanol (green line, as in Figure 22). The reference spectra are the in-situ spectra of water, pH 7 or pure methanol, respectively. The light gray curve in the figure displays the DFT calculation of OTA in the form (b), implicitly taking into account the effect of water as a solvent.

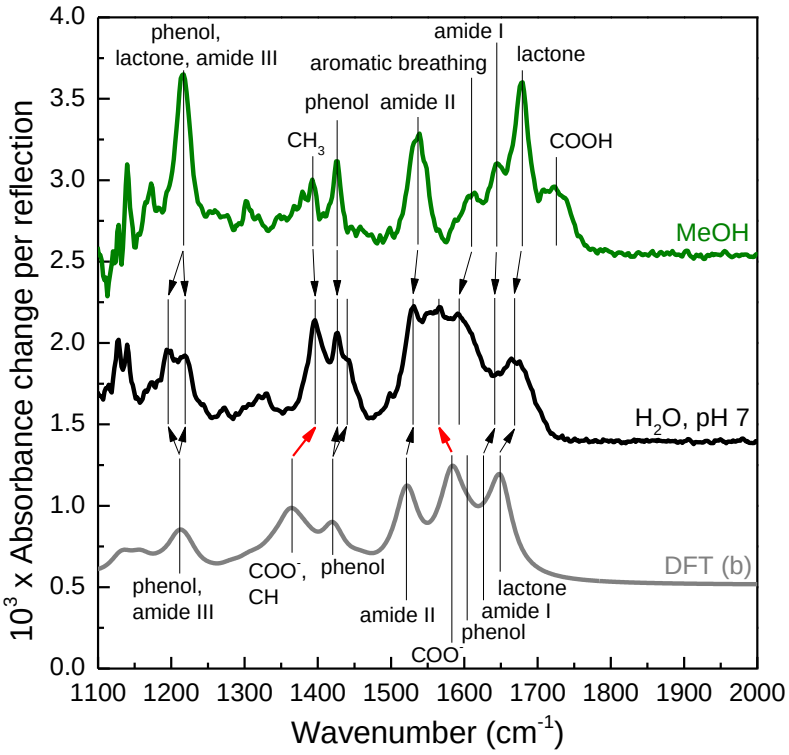


Figure 23: In-situ IR-spectra in s-polarization of 20 mM OTA dissolved in methanol (green) and in water pH 7 (black). The reference spectra are the in-situ IR-spectra of methanol and water pH 7, respectively. Arrows indicate peak-assignments. DFT calculation (dark grey) of OTA in its form (b) in H_2O.

Comparing in a first step quickly the spectra of OTA in water and OTA in methanol, it can be seen that the spectra roughly resemble each other, but the peaks shift in position and intensity. The COOH-peak at 1715 cm^{-1} completely disappears when water is used as solvent at pH 7, indicating a deprotonation of this group in basic solvents. The DFT calculation shows a relatively good agreement with the spectra obtained by in-situ IR, but less well than was observed before with OTA in methanol.

Using both the DFT calculation and the IR spectrum of OTA in methanol the peaks can be assigned. The band at 1669 cm^{-1} can be assigned to the lactone group of OTA, having undergone a slight shift from OTA in methanol. The peak at 1641 cm^{-1} is associated with the amide I vibrations of the amide bond and is in relatively good agreement for both the DFT calculation and the OTA in methanol. The peak at 1593 cm^{-1} stems from aromatic breathing of the benzene rings. The peak at 1565 cm^{-1} arises from the COO^- group and could not be observed in the IR spectra of OTA in methanol. Amide II vibrations can be observed at 1530 cm^{-1} and are also in good agreement with the DFT calculations and the IR measurements of OTA in methanol. The two peaks at 1440 cm^{-1} and 1426 cm^{-1} underwent a splitting from the single phenol peak observed in methanol, and can be associated with phenolate and phenol, respectively. The peak at 1396 cm^{-1} is an overlap of COO^- modes and CH_3 deformation. The double peaks at 1219 and 1195 cm^{-1} stem from the phenol deformation and amide III, according to DFT calculations. These two peaks might not be linked with OTA as can be seen in the calibration measurements in chapter 3.3.2.1.

When comparing in more detail the two spectra of OTA in methanol and in water at pH 7, it can be seen that the COOH peak disappears, while two COO^- peaks appear. Furthermore a splitting of the phenol peak can be observed due to the presence of phenolate. This indicates that OTA is mainly in its form (b) but that there is also the form (c) present in a small concentration.

The strong shifts in peak position and intensity can be explained by the change of solvent, which also changes the hydrogen bonds and van der Waals interactions. This is especially visible for the peaks of lactone (shift from 1680 to 1669 cm^{-1}), aromatic

breathing (from 1610 to 1593 cm^{-1}), amide II (from 1540 to 1530 cm^{-1}) and phenol (from 1425 to 1440 cm^{-1}).

In Figure 24 the in-situ IR spectra in s-polarization of 20 mM OTA in methanol (green) and water at pH 7 (black), pH 8.5 (red) and pH 11 (blue) are displayed. The reference spectra are the in-situ spectra of pure methanol or water, with the same pH as the OTA solutions. The peak assignments remain as for OTA in water at pH 7, except for a peak which becomes visible at 1686 cm^{-1} and which probably stems from a peak shift of the lactone group in presence of phenolate, indicating OTA in its completely deprotonated form (c). An increase in intensity can be observed for the COO^- peak at 1565 cm^{-1}, which indicates the presence of OTA in its open-ring form (d). The phenolate peak at 1440 cm^{-1} also increases, but since the phenol peak remains visible, the presence of both forms (c) and (d) can be assumed.

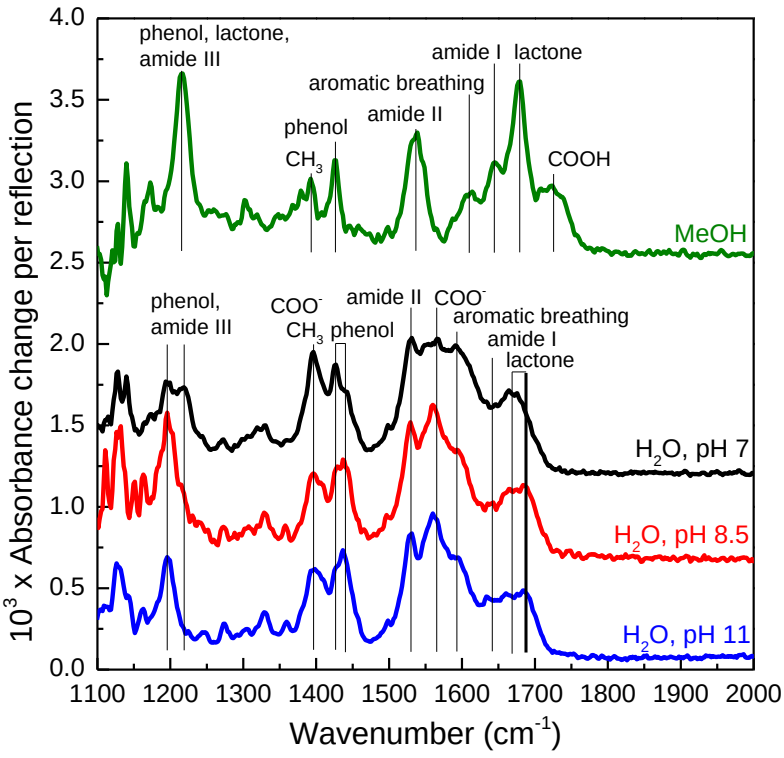


Figure 24: In-situ IR-spectra in s-polarization of 20 mM OTA dissolved in methanol (green) and in water pH 7 (black), pH 8.5 (red), pH 11 (blue). The reference spectra are the in-situ IR-spectra of methanol and water with the same pH, respectively. Arrows indicate peak-shifts.

The spectra of OTA in water at pH 8.5 and pH 11 are very similar concerning peak positions and intensities. A slight increase of intensity can be noticed for the phenolate peak at 1440 cm^{-1}, the COO^- band at 1686 cm^{-1} and the amide I band at 1641 cm^{-1} for pH 11. The main difference between the two spectra of OTA at pH 8.5 and pH 11 is the double-peak at 1219 cm^{-1} and 1195 cm^{-1}, but further analysis is difficult, as these two peaks might not be linked with OTA as can be seen in the calibration measurements.

In H_2O, pH 7 OTA seems to be in its partially deprotonated but closed form, structure (b). For pH 8.5 and pH 11 in water OTA seems to show a coexistence of its fully deprotonated (c) and open-ring form (d).

The DFT calculations of OTA for all forms (a) - (d) are displayed in Figure 25. Here the influence of the solvent becomes more visible, as the calculations diverge more and more from the observed IR spectra. Further calculations are being undertaken to ameliorate the results at the moment of the writing of this thesis.

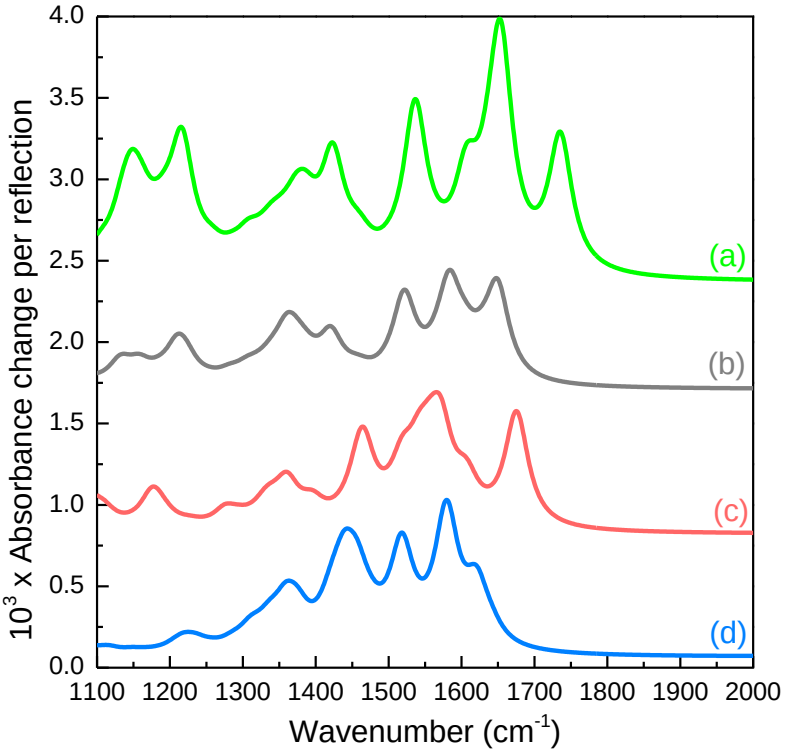


Figure 25: DFT calculations of OTA in all forms. Green curve: OTA form (a) in methanol; Grey curve: OTA form (b) in H_2O; Red curve: OTA form (c) in H_2O; Blue curve: OTA form (d) in H_2O;

(C) OTA in 35 % EtOH, pH 8.5

Before the measurements of OTA in H_2O (see above) were conducted, multiple different in-situ experiments were carried out in 35% EtOH to retrieve the infrared spectrum in conditions more similar to the conditions of the interaction of OTA with its aptamer (cf. chapter 4).

The main difficulty herein is that methanol and ethanol both have very intense infrared spectra. Already a small difference of concentration between the recorded spectrum and its reference spectrum (less than 0.3%) render the result useless, as only ethanol or methanol can be seen in the resulting absorbance spectrum. The best result of these measurements, where no ethanol can be seen, is displayed in Figure 26, where the infrared spectrum of OTA in 35% EtOH in water, pH 8.5 (orange line) is displayed. When comparing this spectrum with the spectrum of OTA in H_2O, pH 8.5 (red spectrum), it can be seen that the height of the bands around 1600 cm^{-1} are similar despite the different OTA-concentrations (8 and 25 mM) in the solutions. It seems that there is a large band between 1500 and 1700 cm^{-1} which might be from water and which is impeding a reliable analysis. This finally led to the idea of preparing OTA solutions solely in water while adapting the pH to assure solubility, leading to the results displayed before.

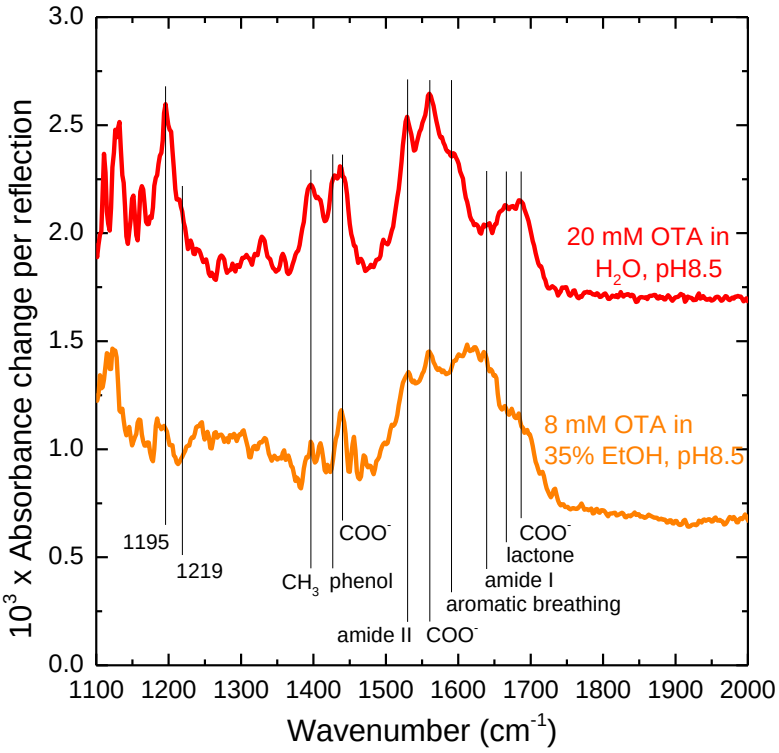


Figure 26: In-situ IR-spectra in s-polarization of 8 mM OTA in 35% EtOH, pH 8.5 (orange) and 20 mM OTA dissolved in H_2O, pH 8.5 (red). The reference spectra are the in-situ IR-spectra of 35% EtOH, pH 8.5 and methanol, respectively.

A precise analysis of the spectrum is difficult, but it seems to also show the coexistence of OTA in its structure (c) and (d) since all three COO^- peaks are visible.

3.3.1.2 UV-vis spectrometry of OTA in different media

A comparison of OTA dissolved in different media at different pH was undertaken. As for the IR-measurements the solvents were methanol, water at pH 7, pH 8.5 and pH 11. The UV-vis spectra of 5 µM OTA in different solvents are displayed in Figure 27. The spectra of OTA in H_2O, pH 7 exhibits a peak at 331 nm. This peak shifts to 379 nm for OTA in H_2O for both pH 8.5 and pH 11. The peak for OTA in methanol is at 331 nm. Consistent with the infrared spectra above, the UV-vis spectra of OTA in H_2O changes when increasing the pH from 7 to 8.5, and then remains nearly stable when further shifting to pH 11. OTA in methanol is expected to be in its structure (a) and in H_2O, pH

7 in structure (b). Since the peak remains at the same place we suppose that the difference between the two structures (fully protonated and simple deprotonation) cannot be identified by UV-vis spectroscopy. The same is the case for the structures (c) and (d) in H_2O at pH 8.5 and pH 11, where also no peak-shift was observed.

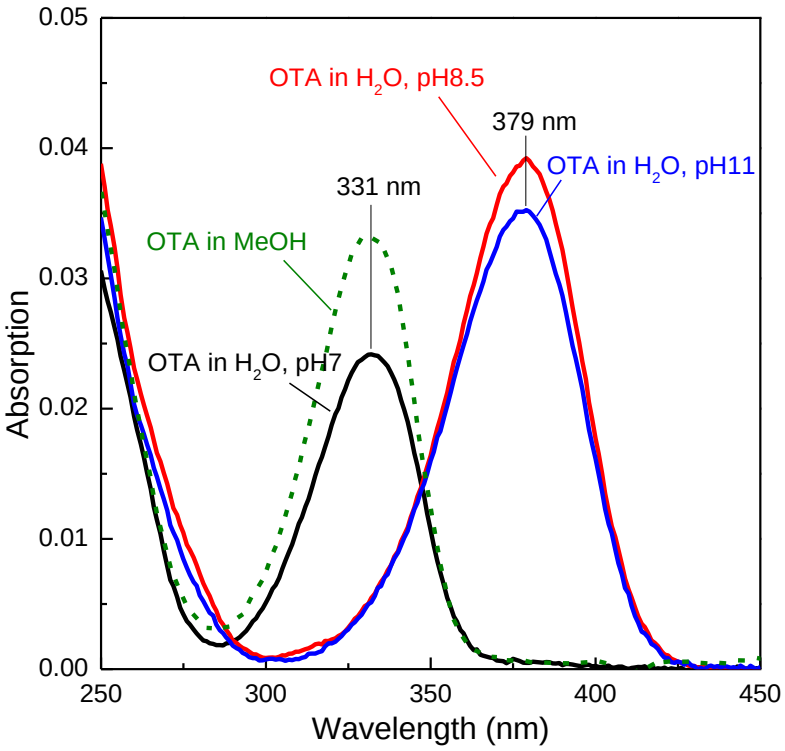


Figure 27: UV-vis spectra of 5 µM OTA in methanol (green), in H_2O pH 7 (black), in H_2O pH 8.5 (red) and in H_2O pH 11 (blue). The reference spectra are the respective solutions without OTA at corresponding pH.

3.3.2 Calibration of OTA IR-intensity and UV-vis absorption to OTA-concentration in solution

3.3.2.1 In-situ IR calibration of OTA in H_2O, pH 8.5

To be able to quantify the surface density of OTA after interaction with aptamers on the surface, a calibration experiment is necessary. For this in-situ infrared spectra are taken at different OTA concentrations. The IR-spectra of OTA in H_2O, pH 8.5 at different concentrations are displayed in Figure 28. All the peaks in the region 1300 –

1800 cm^{-1} decrease as expected with smaller concentrations of OTA. However, the change of intensity of the two peaks at 1125 and 1200 cm^{-1} does not show the same tendency. What causes this behavior is not clear, but they are inutile for the quantitative analysis of OTA.

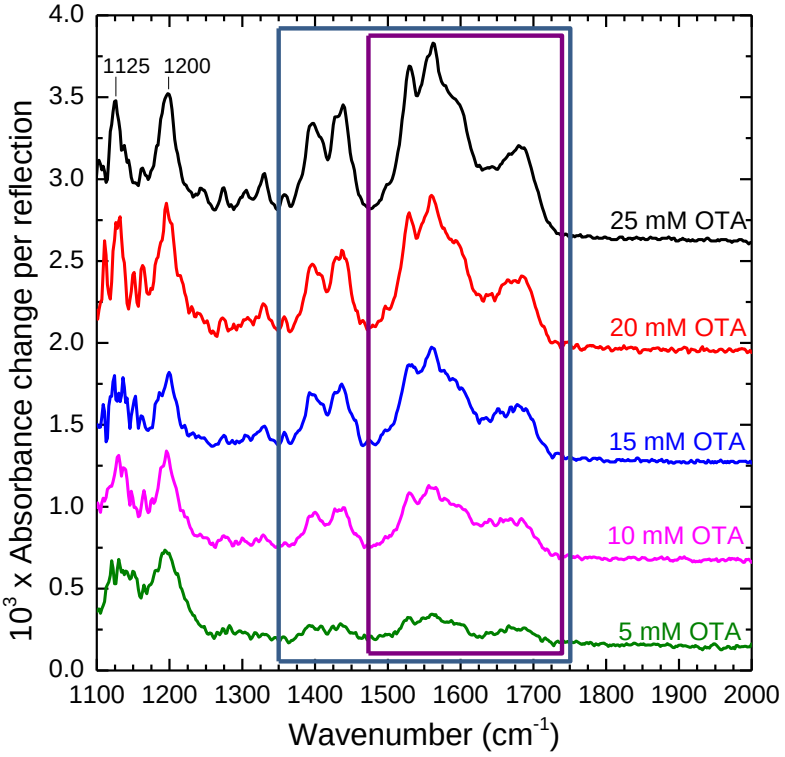


Figure 28: In-situ IR-spectra in s-polarization of OTA dissolved in water at different concentrations, with pH 8.5. The blue and purple boxes indicate the regions used for further analysis. The reference spectrum is the in-situ IR-spectrum of water at pH 8.5.

For further analysis the curves were integrated in the regions 1350-1750 cm^{-1} and 1475-1750 cm^{-1}, as indicated in Figure 28 by the blue and purple box, respectively. The results retrieved by this integration of the different OTA concentrations are displayed as a scatter plot in Figure 29. A linear fit was performed to obtain the correlation of the integrated area with the concentration of OTA, yielding the calibration curves for the two analyzed regions. Both regions show linear behavior with only small deviations from the linear fit. The y-intercept for both curves pass slightly below the origin, indicating a small error, but no physisorption during the in-situ measurements.

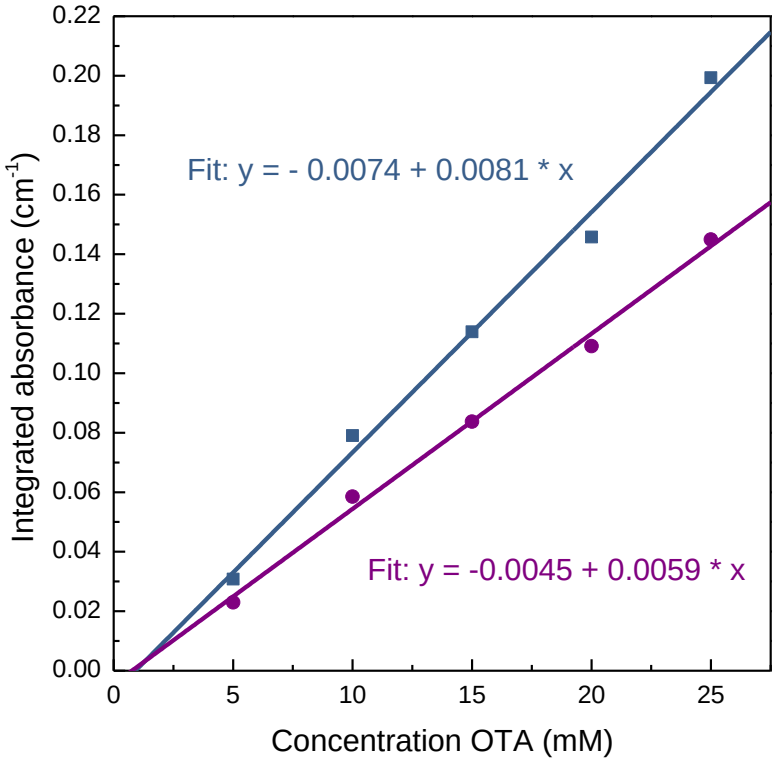


Figure 29: Scatter plots show the integrated area of the two analyzed regions of the IR-spectra for each concentration of OTA (blue: 1350-1750 cm^{-1}, purple: 1475-1750 cm^{-1}), linear fits are displayed for both analyzed regions.

The slope of the purple fit of the region 1475 – 1750 cm^{-1} will be used for the quantification of OTA on surfaces, as described in more detail in chapter 4.

3.3.2.2 Calibration of OTA in regeneration buffer, pH9 by UV-vis spectrometry

Similar to the calibration conducted for OTA by infrared, this calibration was carried out to be able to quantify OTA in regeneration buffer solutions. The UV-vis spectra of OTA at different concentrations are displayed in Figure 30. The spectra all show a peak at 380 nm, which is in agreement with the peak position in H_2O at pH 8.5 and pH 11.

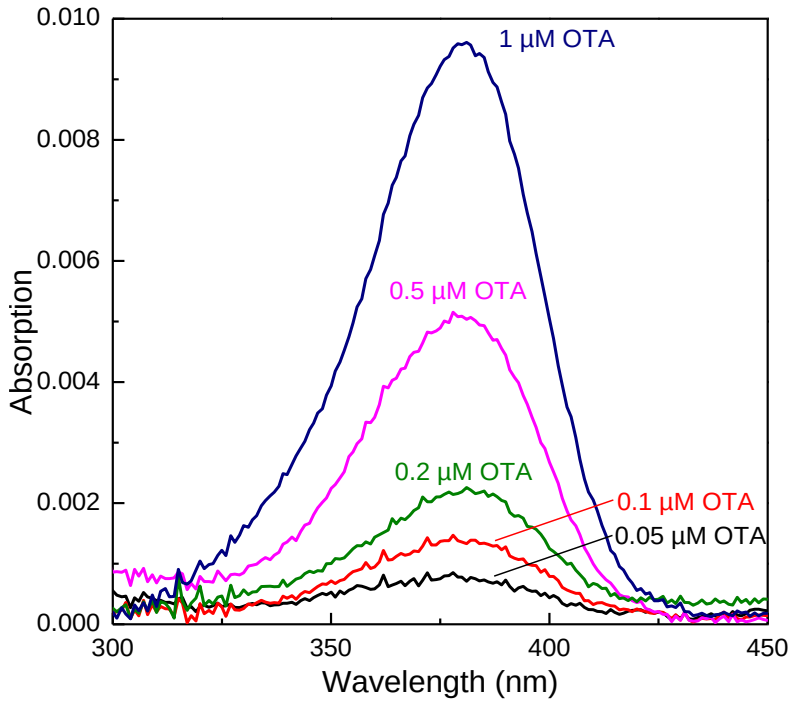


Figure 30: UV-vis spectra of OTA in regeneration buffer at 1 µM (blue), 0.5 µM (pink), 0.2 µM (green), 0.1 µM (red) and 0.05 µM (black). The reference spectrum being the regeneration buffer (pH9).

To retrieve the calibration curve the spectra were integrated in the area 320 - 430 nm. The results of the integration of different OTA concentrations are displayed as a scatter plot in Figure 31. A linear fit was performed to obtain the correlation of integrated area with the concentration of OTA, yielding the calibration curves for the analyzed region. The linear fit shows good agreement with the scatter plot. The y-intercept passes slightly over the origin. The measured points are in good agreement with the fit indicating linear absorption and therefore reliability of the calibration and quantification. The slope ($m = 0.452$ nm/µM) can be used to quantify the concentration of OTA in regeneration buffer solutions. The concentration can be retrieved by measuring the UV-vis absorption curve of the regeneration buffer of interest, integrating in the region 320 - 430 nm and multiplying the result by the slope.

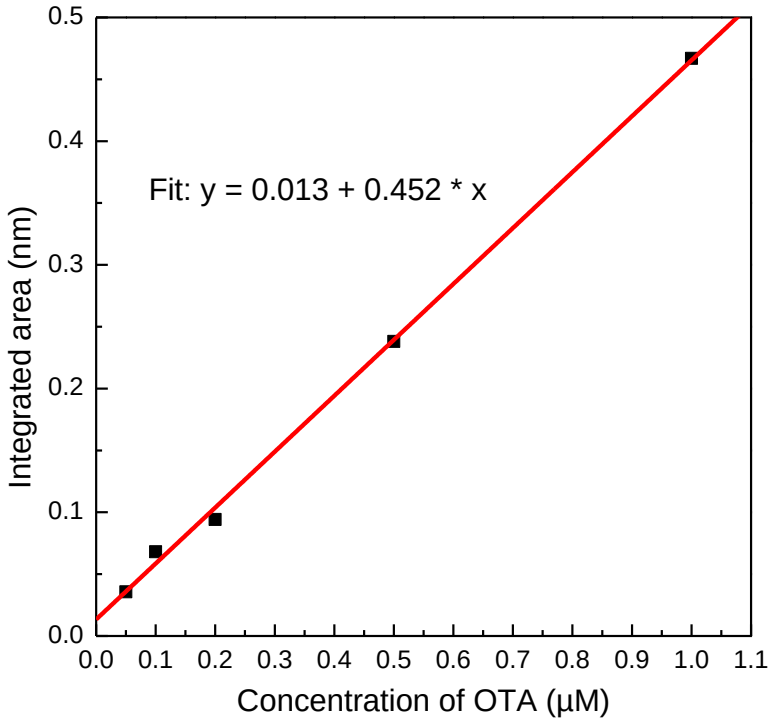


Figure 31: Scatter plot (black) shows the integrated area of the analyzed region of the UV-vis spectra for each concentration of OTA. A linear fit (red) of the scatter plot is also displayed.

3.4 Conclusion

This chapter presented in detail the study of the relation of OTA-structure with its infrared and UV-vis response in different media. This relation was first studied for OTA in different media (methanol and H_2O) and different pH by in-situ infrared experiments. The in-situ measurements of OTA in water were conducted to be close to the working conditions of OTA during the interaction with its aptamer. It was found that in methanol OTA is in its deprotonated form (a), while in H_2O at pH 7 it is in its simple deprotonated form (b). For pH 8.5 and 11 the open-ring and deprotonated form seem to coexist. UV-vis spectroscopy measurements were conducted, and the similar behavior for the different pH values was observed, as by IR, although it could not be differed between structure (a) and (b), as well as between (c) and (d). An in-situ IR calibration measurement was successfully carried out in H_2O, pH 8.5 to be able to quantify OTA on surfaces after interacting with aptamers. This was followed by a UV-vis calibration measurement which allows the quantification of OTA in a regeneration buffer solution.

Following this description of OTA and its infrared/UV-vis behavior, it is now possible to take a closer look at the interaction of OTA with its aptamer on surfaces in the next chapter.

4 INTERACTION APTAMER – OTA

4.1 Introduction

The objective of this chapter is to study and optimize the attachment of the 36mer amino-hexyl-aptamer on ester-NHS activated surfaces, and then study its interaction with OTA by ATR-FTIR. While this interaction has already been studied in solution and on surfaces with direct and indirect detection methods (cf. chapter 1), this has not yet been done by ATR-FTIR with the reliable chemistry which we proposed for our biochips.

As described in chapter 2, ester-NHS-activated surfaces are ideal for further functionalization with NH_2-terminated oligonucleotides, resulting in a strong and reliable immobilization with a covalent amide bond (reaction 1 in Figure 32). Therefore the first objective of this chapter is to optimize the aminolysis reaction of aptamers on activated crystalline silicon surfaces by tuning different reaction conditions: buffer solution, pH, salts and aptamer concentration in buffer. The optimization is carried out in order to favor the direct observation of the OTA-aptamer interaction (reaction 2) by ATR-FTIR. We will furthermore use the optical absorbance of OTA for a quantitative determination of this interaction by UV-vis absorption spectroscopy. The specificity of the aptamer towards OTA is demonstrated by using a chemically similar molecule (warfarin)[222–225], to study the aptamers affinity towards it by ATR-FTIR.

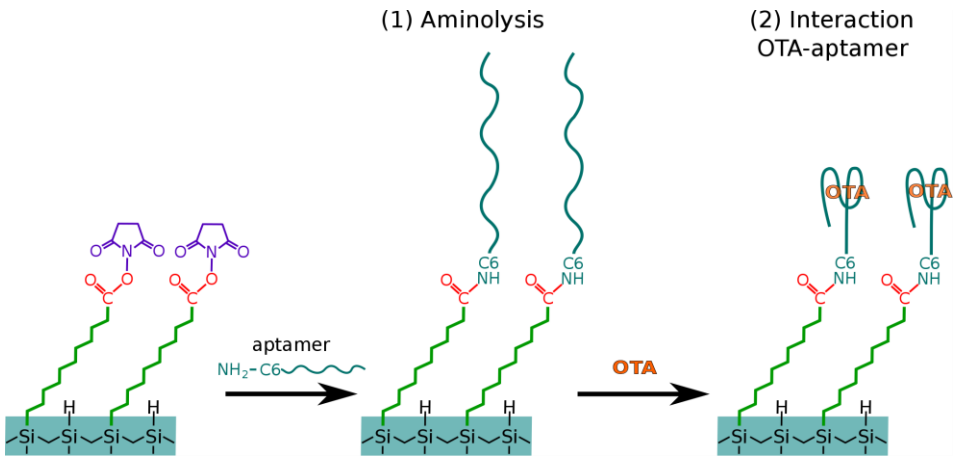


Figure 32: Schematic representation of aminolysis reaction of ester-NHS functionalized surfaces with aptamers (1) on silicon surfaces, and subsequent interaction of OTA with the aptamers (2).

4.2 Materials and methods

4.2.1 Chemicals, substrates and devices

All chemicals were of reagent grade or higher and used without further purification. OTA ($C_{20}H_{18}ClNO_6$) from *Aspergillus ochraceus* was purchased from Sigma Aldrich in reference grade. Warfarin ($C_{19}H_{16}O_4$, analytical standard) was supplied by Fluka Analytical. The solvents (absolute ethanol anhydrous RS grade; methanol RE grade) were supplied by Sigma Aldrich. TRIS (Tris(hydroxymethyl)aminomethane, $NH_2C(CH_2HO)_3$, molecular biology grade) was purchased from Research Organics, EDTA (Ethylenediaminetetraacetic acid, 99% titration) was supplied by Sigma Aldrich. PBS 10X (Phosphate Buffered Saline, 1.37 M NaCl, 27 mM KCl, 0.1 M Na_2HPO_4, 18 mM KH_2PO_4) was purchased from Ambion, and SDS (Sodium dodecyl sulfate, 99%, molecular biology grade) from Sigma. Tween20 was supplied by Calbiochem in Molecular Biology grade and sarkosyl (sodium lauroyl sarcosinate, 97%) by Sigma Chemical. Ultrapure water (MilliQ, 18.2 MΩ·cm, at 25°C) was used to prepare solutions and for rinsing.

The FTIR-ATR measurements were carried out on a Bomem MB 100 (ABB, Suisse, cf. Annex). Normal spectra are composed of 100 scans, but in certain cases 9 x 100 scans were conducted in order to improve the signal to noise ratio. In this case the purge of the sample chamber was prolonged from 40 to 60 minutes in order to further minimize the influence of water vapor and carbon dioxide. The UV-vis spectroscopy measurements are accomplished with a Varian Carry 50 UV-vis spectrophotometer. The scans are taken with a data interval of 1 nm and an average scan time of 0.5 s, in micro cells with 1 ml volume.

4.2.2 Aminolysis with aptamers

The aptamers (“Apt-3’C6” Eurogentec, France, 5’-GAT-CGG-GTG-TGG-GTG-GCG-TAA-AGG-GAG-CAT-CGG-ACA-3’-C6-NH_2) are diluted at different concentrations in various buffers. After optimization, the buffer used for further experiments was 150 mM

phosphate buffer (NaH_2PO_4/Na_2HPO_4) with 0.01% SDS, pH 8.5. The aptamers are then denaturized by heating to 95°C for 5 minutes and rapid cooling in ice for 10 minutes. The solution (1 ml) is then transferred into a Schlenk tube, which is immersed in a water bath heated to 25°C and bubbled with argon for 5 min before the freshly activated (crystalline) silicon prism is added. The Schlenk is bubbled for 5 min before it is closed and left overnight. The sample is removed from the Schlenk, then cleaned in a beaker for 1 min with PBS 1X, 10 min with PBS 1X/0.1% SDS, 1 min with PBS 0.2X, 1 min with 0.1X. Finally the sample is rinsed with ultrapure MilliQ water and dried under a flow of nitrogen.

4.2.3 Interaction of OTA and warfarin with aptamers

OTA or warfarin is pre-dissolved in ethanol (34.7 mM) from its dry state. Following this it is further diluted for a final concentration of 1 mM in the binding buffer *BB-Aguado* (10 mM TRIS, 120 mM NaCl, 20 mM $CaCl_2$, and 5 mM KCl) and the pH is adjusted to pH 8.5. 1 ml of this solution is then added into a Schlenk tube, which is immersed in a water bath at 25°C. The Schlenk is carefully bubbled with argon for 5 min, before the silicon prism is added. The Schlenk is bubbled for 5 min more before the valves are closed. After 1 hour the prism is removed from the Schlenk. The sample is then cleaned in a beaker for 2 x 5 min with BB-Aguado before it is quickly rinsed with ultrapure MilliQ water and dried under a nitrogen flow.

4.2.4 Regeneration of OTA from its aptamers

The regeneration buffer (1 ml of methanol/(10 mM TRIS, 1 mM EDTA, pH 9) (20:80, v/v))[225] is put into a Schlenk tube, which is immersed in a water bath at 25°C, and the prism is added. After 1 hour the prism is removed and rinsed with ultrapure water. The regeneration buffer is then used for further analysis by UV-vis spectroscopy.

4.3 Results and discussion

4.3.1 Aminolysis of activated silicon surfaces with aptamers

4.3.1.1 Optimization of the aminolysis reaction buffer

The aminolysis reaction with aptamers on ester-NHS terminated surfaces depends strongly on the physiological media used. The buffers' ionic strength, pH and the presence of surfactants are crucial factors to be considered when choosing its composition. The ionic strength and pH influence the aminolysis reaction, but can also have an impact on the structure of the aptamer. Aptamers often form well-defined structures before or upon binding with their targets, whereby the presence of certain bivalent salts (e.g. $CaCl_2$ or $MgCl_2$)[128] can be necessary for the structure to be able to form. In the case of OTA, its aptamer forms a G-quadruplex when binding with OTA in presence of salts.[224,226] Surfactants can aid the aminolysis reaction as they improve the wettability on surfaces to favor controlled aptamer immobilisation.[227] In the case of the amorphous silicon biochip architecture the surfactants are also applied to control the aptamer spot size during robotic spotting (Chapter 5).

Phosphate buffers at varying concentrations with different salts (KCl, NaCl, $MgCl_2$), surfactants (Tween20, sarkosyl, SDS) and pH (between pH 7.4 and pH 9.5) were used as shown in Table 4. Concentrated phosphate buffers (1 to 4) showed promising results on the amorphous silicon biochip architecture in the laboratory PMC, so we decided to adapt them for the aminolysis with aptamers on crystalline silicon.[20]

The buffers 1, 2 and 3 are variations of a buffer which has been used in the laboratory PMC for the immobilization of oligonucleotides on microarray slides, but which was not studied by ATR-FTIR before. They contain the anionic surfactant SDS. Buffer 4 (300 mM phosphate buffer) is similar to a buffer suggested by Schott for the use with their commercially available slides (Nexterion® Slide H) for microarray printing.[228] The commercial slides exhibit a very different architecture, as the surface consists of a cross-linked, multi-component polymer layer. This buffer is interesting for our

application because the Slide H and our in-house fabricated slides use the same chemistry for the immobilization of amine-terminated oligonucleotide, as the top layer of the Slide H is also ester-NHS terminated. This buffer contains the polysorbate-type nonionic surfactant Tween20 and the amphiphilic ionic surfactant sarkosyl. The last buffer (5) is sometimes used for the association of OTA with its aptamer.[229] It consists of a lower phosphate concentration and a high concentration of various salts, and exhibits a lower pH of 7.4.

Table 4: List of buffers used for the aminolysis with aptamers on surfaces.

#	Phosphate	Salts	Surfactants	pH
1[(20)]	150 mM: 146 mM Na_2HPO_4 4 mM NaH_2PO_4		0.01% SDS	8.5
2	150 mM: 146 mM Na_2HPO_4 4 mM NaH_2PO_4		0.01% SDS	9.5
3	150 mM: 146 mM Na_2HPO_4 4 mM NaH_2PO_4	1 mM $MgCl_2$	0.01% SDS	8.5
4[(228)]	300 mM: 292 mM Na_2HPO_4 8 mM NaH_2PO_4	1 mM $MgCl_2$	0.005% Tween 20, 0.001% sarkosyl	8.5
5[(229)]	2 mM: 0.2 mM K_2HPO_4, 1.8 mM KH_2PO_4	1 mM $MgCl_2$, 140 mM NaCl, 2.7 mM KCl		7.4

The impact of surfactants on the aminolysis reaction was studied by comparing the buffers 3 and 4. Sometimes salts (like $MgCl_2$) are added to buffers to favor the pre-forming of the aptamer for a better binding of the analyte, as was done for the buffers 3, 4 and 5.[230] The necessity of adding $MgCl_2$ for the aminolysis reaction is studied by comparing the buffers 1 and 3. The impact of the pH on the reaction yield was studied with the buffers 1 and 2. Buffer 5, which has very different phosphate and salt concentrations, was used to pre-form aptamers before immobilization in order to favor the interaction aptamer-OTA.

The left side of Figure 33 shows the IR-spectra of surfaces for acid-terminated surfaces and after aminolysis reaction of the ester-NHS surfaces in the buffers 1, 3 and 4. The

buffers 2 and 5 showed no indication of successful aminolysis reaction (no amide I or amide II peaks), therefore their spectra are not displayed. The reaction was carried out with an aptamer concentration of 75 µM. For all three buffers an acid peak (at ~1718 cm^{-1}) is present after the aminolysis reaction. A new band at 1650 cm^{-1} appears which corresponds to the stretching carbonyl mode vCO of the amide, called amide I. For buffer 2 and 3 there is also a small band at 1530 - 1540 cm^{-1}, which is assigned to the stretching mode of the CNH of amide, called amide II. Normally amide II exhibits an intensity which is lower, but remains comparable to the one of amide I (see for example aminolysis with NH_2-PEG in chapter 2). In this case the amide II intensity might be too low and therefore under the noise of the spectra. From the appearing amide bonds and the remaining acid peak we can already conclude that the aminolysis worked, but is not complete due to hydrolysis of ester-NHS. It also seems to have worked better for the buffers 1 and 3 than the buffer 4, as their amide I and amide II peaks are significantly larger.

A question which arises is why the infrared signature of DNA is not observable. The infrared spectra of DNA is rather complex with a multitude of peaks of similar intensity over a very wide range (700 – 1720 cm^{-1})[231,232]. This is due to the fact that DNA is chemically quite complex and consists of four nucleobases, composed of hydrogen, carbon, oxygen, nitrogen and phosphorous. Therefore the observation of DNA is difficult if the quantity is not large enough to result in strong and clear peaks. However, after the aminolysis reaction there seems to be an overlap of amide I and the carbonyl band (compared with IR-spectrum of aminolysis with NH_2-PEG in chapter 2.4.4), which might actually stem from the IR carbonyl modes of the bases of DNA.

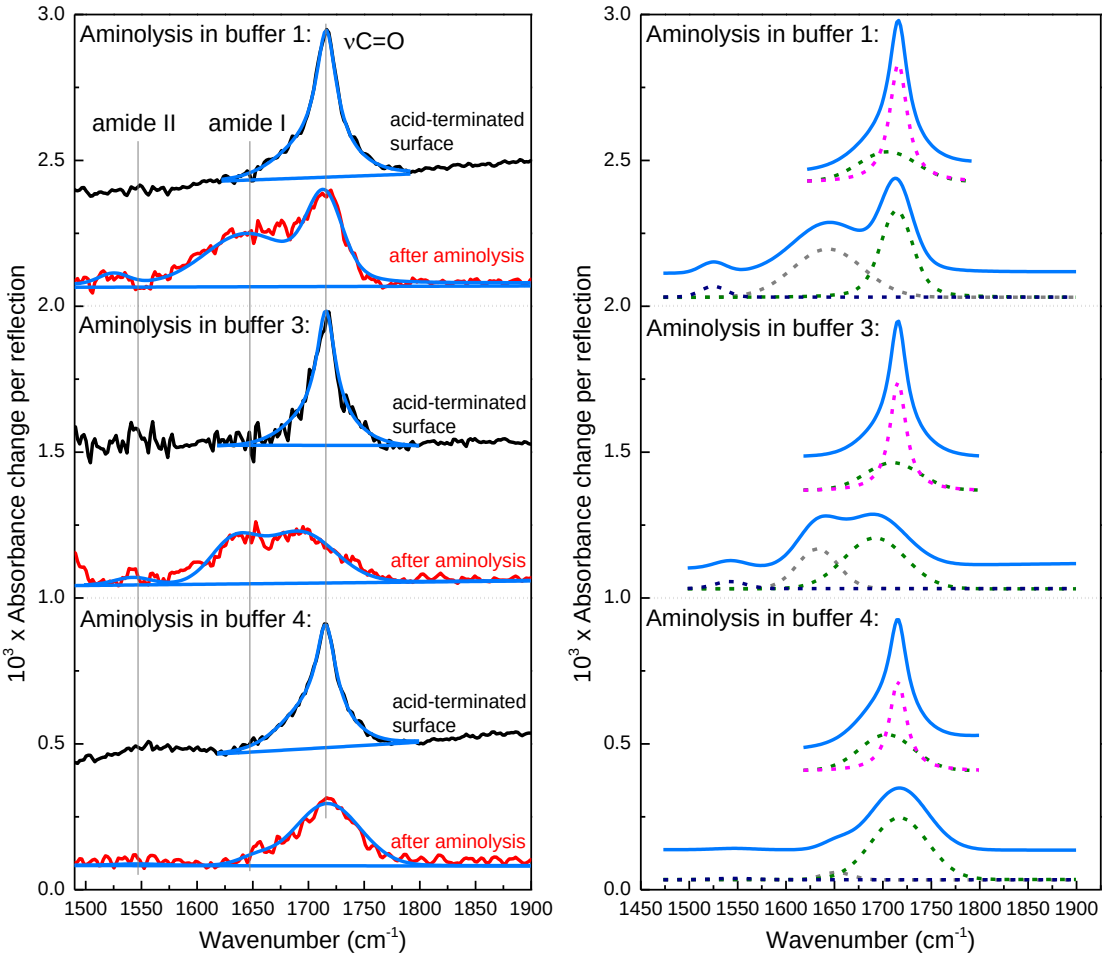


Figure 33: Left side: ATR-FTIR spectra (p-polarization) of acid surfaces and surfaces after aminolysis reactions with aptamers in three different buffer solutions, with superposed fits (blue) for quantitative analysis. The reference ATR-FTIR spectra are the H-terminated silicon surfaces (SiH_X). Right side: deconvolution of the fits of the peaks in the carbonyl region.

While it is already visible from the IR-spectra that the buffer 4 worked less sufficiently, a quantitative analysis is necessary to compare buffer 1 and 3. For the quantitative analysis the curves are fitted (Figure 33, right side) as described in chapter 2, with a Gauss and Lorentz curve for the acid peak of the acid surface. For the aptamer surface the acid, the amide I and amide II peaks are fitted with a Gaussian profile.

The integrated intensities of the fits are displayed in Table 5. All three buffers exhibit a decrease for the intensities of acid groups on the surface after the aminolysis reaction. The three buffers also display amide I and amide II peaks, but in varying intensities.

With the integrated intensities it becomes more visible how much the amide I band changes between the different buffers, as the integrated area increases strongly when comparing buffer 4 with 3, and rises even more for buffer 1.

Table 5: Integrated intensities (cm^{-1}) of fits displayed in Figure 33 of surfaces after grafting of undecylenic acid and aminolysis reaction with aptamers. Column colors correspond to colors of fits in Figure 33.

	Buffer	**Acid surfaces**		**Aptamer surfaces**					
		Acid **vC=O stretching**		Amide II **vCNH mode**		Amide I **vC=O stretching**		Remaining acid **vC=O stretching**	
		$A_{1705+1715,P}$	$A_{1705+1715,S}$	$A_{1550,P}$	$A_{1550,S}$	$A_{1650,P}$	$A_{1650,S}$	$A_{1720,P}$	$A_{1720,S}$
	1	0.0218	0.0212	0.0012	0.0011	0.0149	0.0131	0.0145	0.0116
$\eta_{apta}\uparrow$	3	0.0185	0.0156	0.0010	0.0009	0.0072	0.0104	0.0138	0.0111
	4	0.0189	0.0156	0.0002	0.0000	0.0010	0.0006	0.0154	0.0114

The success of the immobilization of aptamers, and its quantification are determined with the remaining acid and not by the amide bond because the quantification of the amide bond would demand a cumbersome calibration measurement with amide bonds in solution, while the quantification of the C=O acid bond is well established and reliable.

The values from the fits in Table 5 are used for the quantitative analysis; the results are displayed in Table 6. As was already visible in the IR-spectra the surface density of immobilized aptamers increases from buffer 4 ($N_{apta} = 0.27 \cdot 10^{14}\ cm^{-2}$) to buffer 3 ($N_{apta} = 0.36 \cdot 10^{14}\ cm^{-2}$) and even further when using buffer 1 ($N_{apta} = 0.44 \cdot 10^{14}\ cm^{-2}$). The reaction yield also increases from 17% to 26% from buffer 4 to 1. Buffer 1 and 3 barely show a difference in the reaction yield η.

Table 6: Surface densities of acid surfaces (N_{CO}), and of remaining acid (N'_{CO}) and aptamers (N_{apta}) after aminolysis reaction. Reaction yield η displays the percentage of acid sites where aptamers were immobilized. The surface densities have an uncertainty of $0.2 \cdot 10^{14}$ cm^{-2}.

Buffer	**Surface density acid** N_{CO}	**Surface density remaining acid** N'_{CO}	**Surface density aptamers** $N_{apta} = N_{CO} - N'_{CO}$	**Yield** $\eta = \frac{N_{apta}}{N_{CO}}$
1	$1.65 \cdot 10^{14}$ cm^{-2}	$1.21 \cdot 10^{14}$ cm^{-2}	$0.44 \cdot 10^{14}$ cm^{-2}	26%
3	$1.51 \cdot 10^{14}$ cm^{-2}	$1.15 \cdot 10^{14}$ cm^{-2}	$0.36 \cdot 10^{14}$ cm^{-2}	24%
4	$1.57 \cdot 10^{14}$ cm^{-2}	$1.30 \cdot 10^{14}$ cm^{-2}	$0.27 \cdot 10^{14}$ cm^{-2}	17%

The influence of adding the salt $MgCl_2$ at a concentration of 1 mM to the amidation solution can be seen with the buffers 1 and 3. The aminolysis yield remains nearly the same, showing that the immobilization of aptamers is not influenced by the salt. The impact on the aminolysis yield of the surfactant can be seen by comparing buffer 3 (0.01% SDS) and buffer 4 (0.005% Tween 20, 0.001% sarkosyl). The yield of the buffer 3 is significantly higher, therefore excluding the use of Tween 20 and sarkosyl for the amidation solution. To see the effect of the pH, buffer 1 and 2 are compared. As the buffer 2 (pH 9.5) yielded no analyzable result, the importance for the aptamer solution to have a pH 8.5 becomes clear. The buffer 5 displayed no amide bands after aminolysis reaction, therefore it was excluded from use for further aminolysis reactions. Since the buffer 1 showed the best results, it was used for the further experiments.

4.3.1.2 Optimization of the surface density of immobilized aptamers

We followed two distinct pathways in order to increase the surface density of immobilized aptamers. This was done because higher aptamer surface densities might increase the chance of observing the interaction OTA-aptamer on surfaces. The first pathway was to increase the concentration of aptamers in the aminolysis solution, and

the second was to repeat the activation / aminolysis reactions. For these experiments the previously chosen buffer (buffer 1: phosphate 150 mM, SDS 0.01%, pH 8.5) was used for the aminolysis reactions.

(A) High aptamer concentration in the aminolysis solution

Different concentrations of aptamers in the aminolysis solution were compared (Figure 34, IR spectra in the carbonyl on the left, fits and deconvolutions on the right), in order to increase the surface density. The spectra of the 600 µM reaction were acquired with 9x100 scans in order to improve the signal-noise ratio. As can be seen in the IR spectra there is a strong increase of the amide I peak (~1650 cm^{-1}) when the concentration is changed from 150 µM to 300 µM. The peak of the remaining acid is reduced with increasing aptamer concentration, and also shifts to longer wavenumbers (from 1715 cm^{-1} to 1730 cm^{-1}) due to reduced interaction between the carboxyl groups. When further increasing the aptamer concentration from 300 µM to 600 µM, the amide I peak seems similar at first look, but closer analysis shows that it slightly increases and also widens.

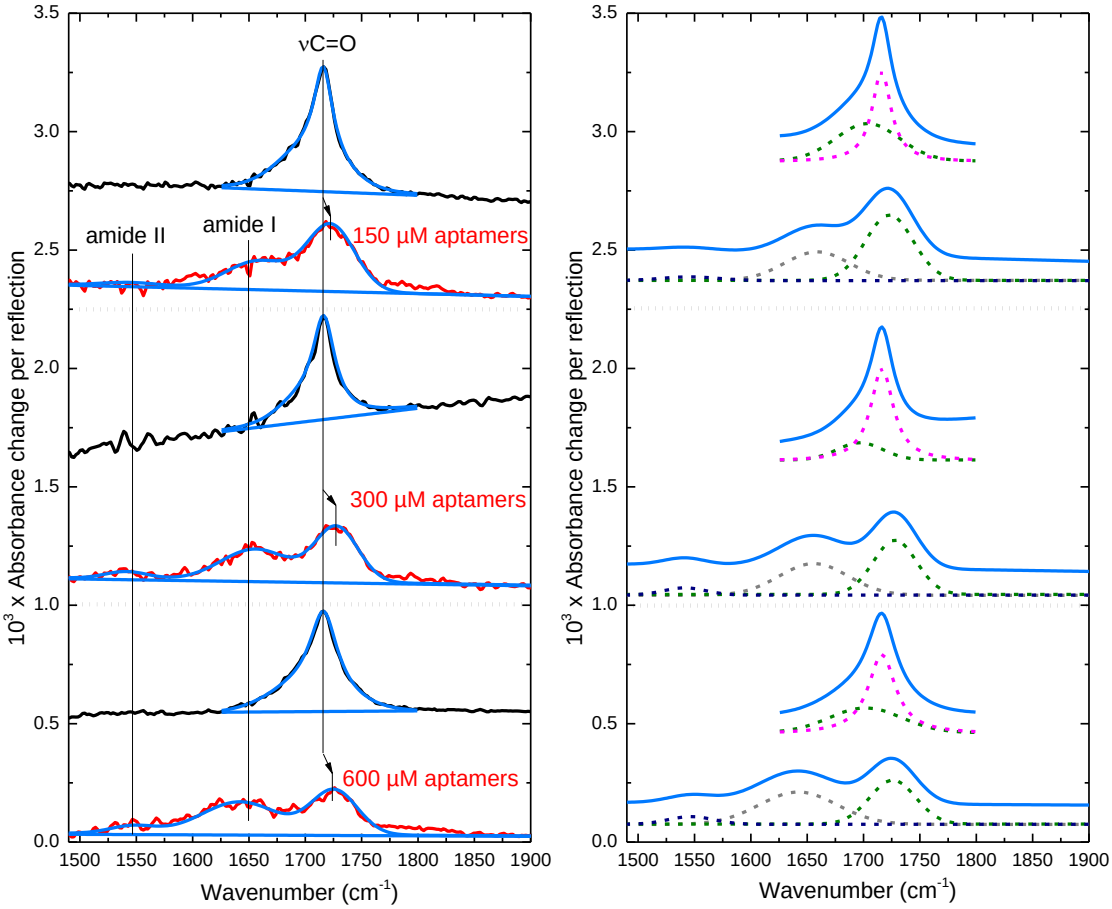


Figure 34: Left side shows ATR-FTIR (p-polarization) spectra of acid surfaces (red) and surfaces after aminolysis reactions (black) with different aptamer concentrations, with superposed fits (blue) for quantitative analysis. The reference ATR-FTIR spectra are the H-terminated silicon surfaces (SiH_X). Right side displays the deconvolution of the fits.

The fits of the infrared spectra (right side Figure 34) were conducted as above, with a Gauss curve for the acid peak, and additional Gauss curves for the amide I and amide II peaks. The integrated intensities of the fits are displayed in Table 7. The results of the quantitative analysis conducted with these values are shown in Table 8. The surface density of remaining acid decreases with increasing aptamer concentration (from $1.14 \cdot 10^{14}$ cm^{-2} to $0.77 \cdot 10^{14}$ cm^{-2}), and at the same time the aptamer surface density increases (from $0.68 \cdot 10^{14}$ cm^{-2} to $1.12 \cdot 10^{14}$ cm^{-2}). The reaction yield is the best at an aptamer concentration of 600 µM with a value of 59%, compared to 37% and 47% at the lower aptamer concentrations. For the subsequent experiments we kept the concentration 600 µM.

Table 7: Integrated intensities (cm^{-1}) of the fits (right side Figure 34) of acid and aptamer terminated surfaces in p- and s-polarization for quantitative analysis. Column colors correspond to colors of fits in Figure 34.

Experiment	Acid surfaces		Aptamer surfaces					
	Acid **vC=O stretching**		Amide II **vCNH mode**		Amide I **vCO stretching**		Remaining acid **vC=O stretching**	
	$A_{1705+1715,P}$	$A_{1705+1715,S}$	$A_{1545,P}$	$A_{1545,S}$	$A_{1650,P}$	$A_{1650,P}$	$A_{1725,P}$	$A_{1725,S}$
150 µM	0.0235	0.0209	0.0010	0.0009	0.0086	0.0078	0.0146	0.0129
300 µM	0.0186	0.0151	0.0014	0.0012	0.0103	0.0099	0.0110	0.0109
600 µM	0.0239	0.0203	0.0017	0.0013	0.0113	0.0109	0.0095	0.0077

Table 8: Surface densities of acid surfaces (N_{CO}), and of remaining acid (N'_{CO}) and aptamers (N_{apta}) after aminolysis reaction. Reaction yield η displays the percentage of acid sites where aptamers were immobilized. The surface densities have an uncertainty of $0.2 \cdot 10^{14}$ cm^{-2}.

Experiment	Surface density acid $\boldsymbol{N_{CO}}$	Surface density remaining acid $\boldsymbol{N'_{CO}}$	Surface density aptamers $\boldsymbol{N_{apta} = N_{CO} - N'_{CO}}$	Yield $\boldsymbol{\eta = \frac{N_{apta}}{N_{CO}}}$
150 µM	$1.82 \cdot 10^{14}$ cm^{-2}	$1.14 \cdot 10^{14}$ cm^{-2}	$0.68 \cdot 10^{14}$ cm^{-2}	37%
300 µM	$1.50 \cdot 10^{14}$ cm^{-2}	$0.80 \cdot 10^{14}$ cm^{-2}	$0.70 \cdot 10^{14}$ cm^{-2}	47%
600 µM	$1.89 \cdot 10^{14}$ cm^{-2}	$0.77 \cdot 10^{14}$ cm^{-2}	$1.12 \cdot 10^{14}$ cm^{-2}	59%

(B) Multiple cycles of activation/aminolysis

Further studies were conducted to determine whether repeated activation and aminolysis reactions can further increase the aptamer surface density. Unreacted

carboxyl end groups of the organic monolayer are activated again, and should then again be available for aminolysis with aptamers.

Four cycles of activation / aminolysis (with aptamers at 600 µM) were conducted on the acid surface with a starting surface density $N_{CO} = 1.89 \cdot 10^{14} cm^{-2}$. After each step the surfaces were studied with ATR-FTIR. The spectra acquired with 900 scans are displayed on the left in Figure 35, with the reference spectra being the hydrogenated silicon surfaces. The surfaces after the activation reactions are displayed in black, and after aminolysis reactions are displayed in red. The first activation of the acid monolayer shows very intense ester-NHS peaks, which was already discussed before (chapter 2.4.3). The subsequent first aminolysis with aptamers exhibits an amide I peak and a decreased CO peak, indicating successful immobilization of aptamers. The second activation shows a clear decrease of ester-NHS groups in comparison to the first activation, verifying that less acid groups were available for activation. The second aminolysis, on the other hand, compared to the first aminolysis, shows an increase of amide I bonds and a decrease of remaining acid, indicating an increase in immobilized aptamers. This behavior of decreasing ester-NHS peaks and increasing amide I peaks, with a decrease of remaining acid continues for all four cycles. Nevertheless the change is not very large between third and fourth cycle, making a fifth cycle unnecessary.

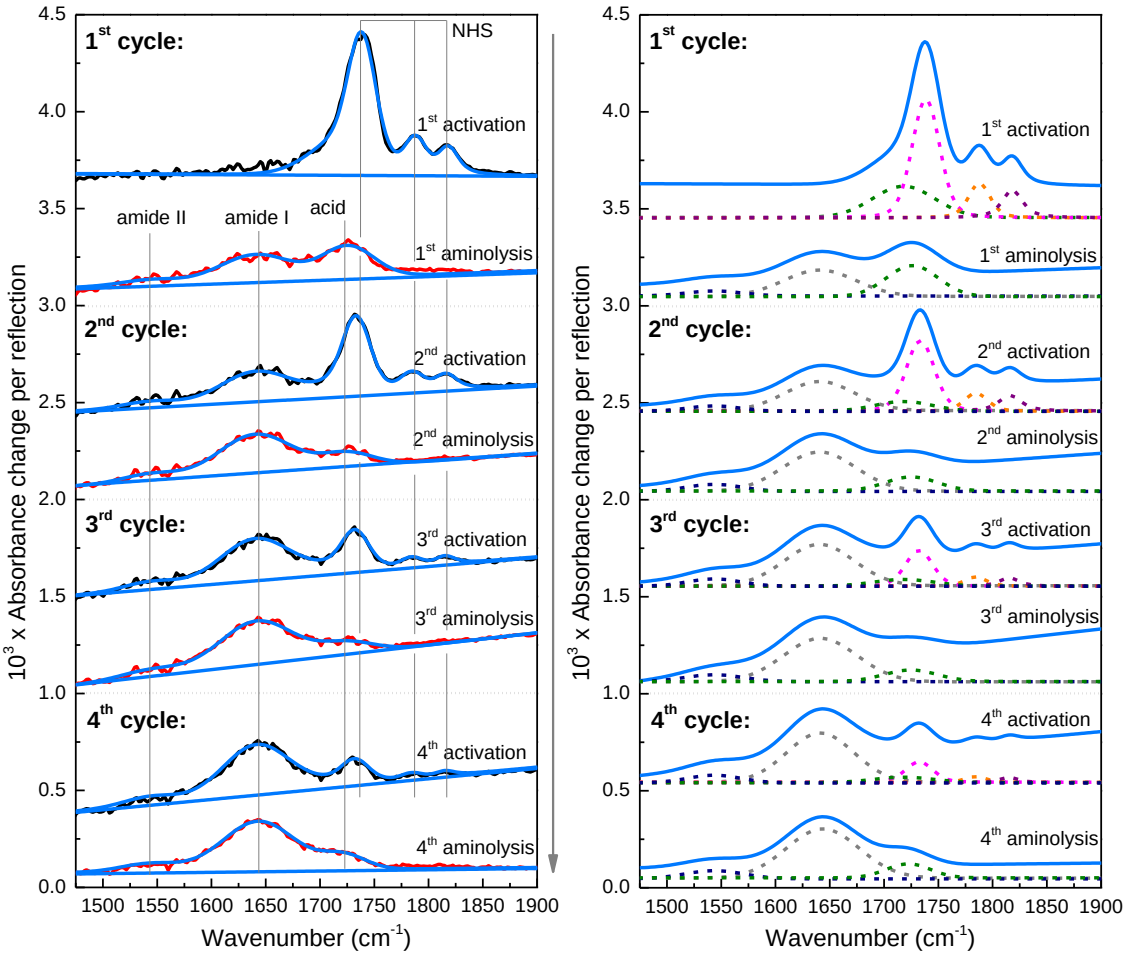


Figure 35: Left side: ATR-FTIR spectra (p-polarization) of surfaces during four cycles of activation (black) and aminolysis (red) reaction, with superposed fits (blue) for quantitative analysis. The reference spectra are the H-terminated silicon surfaces (SiH_X). Right side shows the deconvolution of the fits.

The integrated intensities of the fits (right-hand side in Figure 35) are displayed in Table 9. The surfaces after the activation reaction are fitted with a Gauss curve (FWHM = 50-70 cm^{-1}) for the acid peak at 1718 cm^{-1}, while the three remaining ester-NHS peaks at 1730 (FWHM = 20-30 cm^{-1}), 1788 (FWHM = 15-30 cm^{-1}) and 1819 cm^{-1} (FWHM = 20-35 cm^{-1}) are fitted with a Voigt profile (cf. annex I). The fitting of the curves becomes increasingly difficult for the later cycles, as the peaks continuously get smaller and wider. Therefore for cycle 3 and 4 of the activation reactions the peak positions of the small peaks (1788 and 1819 cm^{-1}) were forced during the fitting.

The spectra of surfaces after aminolysis reaction are fitted as before, with a Gauss profile for the amide I at 1650 cm^{-1} (FWHM $\approx$ 75 cm^{-1}) and the amide II at 1530-1540 cm^{-1}. The remaining acid is fitted with a Gaussian at 1725 cm^{-1}, (FWHM $\approx$ 47-58 cm^{-1}). For these fits the difficulty resides in the overlap of the amide I and the CO band, which also influences the precision of the results.

A first analysis of the results can already be conducted with the integrated intensities of the fits. With every reaction cycle the intensity of the amide I and amide II increases, while the remaining acid, as well as the ester-NHS decrease. The intensities of the amide I and amide II peaks only show minor changes between the aminolysis and following activation reaction (e.g. between 2nd aminolysis and 3rd activation reaction), indicating no change in the aptamer surface density by the activation reactions.

Table 9: Integrated intensities (cm^{-1}) of the fits (Figure 35) of surfaces after activation and aminolysis reaction in p- and s-polarization for quantitative analysis. Column colors correspond to colors of fits in Figure 35.

Cycle #	**Reaction step**	**Amide II** vCNH mode		**Amide I** vCO stretching		**Remaining acid** vC=O stretching		**Ester-NHS** vC=O vibr. antisymm.		**Ester-NHS** vC=O vibr. symmetric		**Ester-NHS** vC=O stretching	
		$A_{1540,P}$	$A_{1540,S}$	$A_{1640,P}$	$A_{1640,S}$	$A_{1720,P}$	$A_{1720,S}$	$A_{1740,P}$	$A_{1740,S}$	$A_{1788,P}$	$A_{1788,S}$	$A_{1819,P}$	$A_{1819,S}$
1	Activation	0	0	0	0	0.0115	0.0111	0.0210	0.0175	0.0051	0.0040	0.0045	0.0037
1	Aminolysis	0.0017	0.0013	0.0113	0.0109	0.0095	0.0077	0	0	0	0	0	0
2	Activation	0.0017	0.0015	0.0119	0.0110	0.0033	0.0029	0.0127	0.0107	0.0029	0.0023	0.0027	0.0023
2	Aminolysis	0.0023	0.0019	0.0170	0.0153	0.0043	0.0029	0	0	0	0	0	0
3	Activation	0.0023	0.0018	0.0171	0.0152	0.0024	0.0017	0.0063	0.0049	0.0014	0.0012	0.0013	0.0013
3	Aminolysis	0.0024	0.0020	0.0190	0.0171	0.0036	0.0027	0	0	0	0	0	0
4	Activation	0.0025	0.0020	0.0195	0.0173	0.0019	0.0013	0.0036	0.0027	0.0008	0.0008	0.0008	0.0007
4	Aminolysis	0.0029	0.0023	0.0214	0.0203	0.0036	0.0033	0	0	0	0	0	0

The results of the quantitative analysis are displayed in Table 10, and were obtained with the integrated intensities of the fits from Table 9. It can be seen that the second activation shows a higher surface density of ester-NHS than remaining acid was

available after the first aminolysis. This result is acceptable when the uncertainty of the analysis is taken into account, but nevertheless implies a high activation rate. The aptamer surface density increases with every cycle of activation/aminolysis reaction. As was already visible in the IR spectra, the surface density of aptamers does not change much anymore between the third and fourth cycle. The final surface, after four cycles of activation and aminolysis reaction, exhibits an estimated aptamer surface density of $N_{apta} = 1.6 \cdot 10^{14}\ cm^{-2}$, or a yield $\eta = \frac{N_{apta}}{N_{CO}} = 85\%$. Thus multiple cycles increase the surface density of immobilized aptamers on the surface. We decided to continue with four cycles of activation/aminolysis for the further experiments in order to be sure to have as many aptamers as possible immobilized on the surface.

Table 10: Surface coverage and reaction yield (in relation to acid-terminated surface) of activation and aminolysis reactions. The surface densities have an uncertainty of $0.2 \cdot 10^{14}$ cm^{-2}.

	Activation reaction		**Aminolysis reaction**		
Cycle #	Surface density NHS N_{NHS}	Yield η (NHS)	Surface density remaining acid N'_{CO}	Surface density aptamer $N_{apta} = N_{CO} - N'_{CO}$	Yield η (aptamer)
1	$1.42 \cdot 10^{14}$ cm^{-2}	75%	$0.77 \cdot 10^{14}$ cm^{-2}	$1.12 \cdot 10^{14}$ cm^{-2}	59%
2	$0.83 \cdot 10^{14}$ cm^{-2}	44%	$0.37 \cdot 10^{14}$ cm^{-2}	$1.52 \cdot 10^{14}$ cm^{-2}	80%
3	$0.36 \cdot 10^{14}$ cm^{-2}	19%	$0.30 \cdot 10^{14}$ cm^{-2}	$1.59 \cdot 10^{14}$ cm^{-2}	84%
4	$0.22 \cdot 10^{14}$ cm^{-2}	12%	$0.28 \cdot 10^{14}$ cm^{-2}	$1.61 \cdot 10^{14}$ cm^{-2}	85%

(C) Analysis of the aminolysis yield with aptamers on crystalline silicon

The aptamer surface densities found above incite interest in the maximum surface density on surfaces. As the aptamers form the G-quadruplex structure upon binding with OTA steric hindrance might be problematic if the surface density is too high. As the aminolysis is carried out with denaturized aptamers in their “straight” state we calculate the maximum surface density of aptamers in its denaturized state and in the G-quadruplex form.

Venta et al. found the diameter of a single strand of DNA to be 0.8 - 0.9 nm.[233] Assuming that the aptamers are perfectly circular and are closely packed with a hexagonal lattice (density factor $\frac{\pi}{2\sqrt{3}}$), the maximal surface density for straight aptamers can be between $N_{max} = 1.43 \cdot 10^{14} - 1.80 \cdot 10^{14}\ cm^{-2}$ (calculated with $N_{max} = \frac{1cm^2}{d^2\pi/4} \cdot \frac{\pi}{2\sqrt{3}}$).

When the aptamers form a G-quadruplex structure, their size has been shown to be in the range of 1.27 - 2.39 nm.[234] With the same assumptions as before, the maximal surface density under the G-quadruplex form is between $N_{max} = 0.72 \cdot 10^{14} - 0.20 \cdot 10^{14}\ cm^{-2}$.

From these results we can see that a very high surface density ($N_{apta} = 1.61 \cdot 10^{14}\ cm^{-2}$) was achieved for aptamers immobilized on the surface in their straight form. In case of the aminolysis being carried out with $MgCl_2$ (buffer 3, in order to pre-form the structure to favor OTA-binding) an aminolysis yield of $N_{apta} = 0.36 \cdot 10^{14}\ cm^{-2}$ was achieved which is still under the range of maximum surface density for aptamers with G-quadruplex structure. Carrying out the aminolysis in buffer 3 at higher concentrations and with repeated activation/aminolysis reactions would have been interesting for further investigation.

From the very high surface density of aptamers arises the question if high surface densities are desirable, as that might incite steric hindrance and prevent the formation of the G-quadruplex structure. The question if high aptamer surface densities are necessary for showing the interaction OTA-aptamer directly by infrared will be answered in the following subchapter.

4.3.2 Interaction of OTA with its aptamer by IR on crystalline silicon surfaces

In order to show the interaction of OTA with immobilized aptamers it is necessary to consider the medium in which the interaction takes place. For the aptamer to bind OTA it is necessary to form the G-quadruplex structure, for which the presence of certain salts is necessary.[235,236] We decided to use the exact binding buffer

"BB-Aguado" which was used by Cruz-Aguado et al. for the SELEX-process of the aptamer in order to ensure an optimal interaction.[128] Four cycles of activation and aminolysis reactions were conducted in order to immobilize a high quantity of aptamers on surfaces. On these surfaces the association was carried out with 1 mM OTA in BB-Aguado (10 mM TRIS, 120 mM NaCl, 20 mM $CaCl_2$, and 5 mM KCl), pH 8.5. The association was performed on multiple samples in order to study its reproducibility. The IR-spectra, which were obtained before the one discussed in this chapter, always displayed very similar behavior, but also exhibited a bad noise to signal ratio, baseline problems and incorporated a large band from 1500-1700 cm^{-1}. As the infrared response of OTA on surfaces is very low, the signal to noise ratio and thereby sensitivity were improved by raising the number of scans to 9x100 instead of just 100 scans. The ATR-FTIR spectrum of the surface after association is displayed in Figure 36, the reference spectrum being the surface with immobilized aptamers. The spectrum from the in-situ IR measurement of OTA is also displayed for comparison (green).

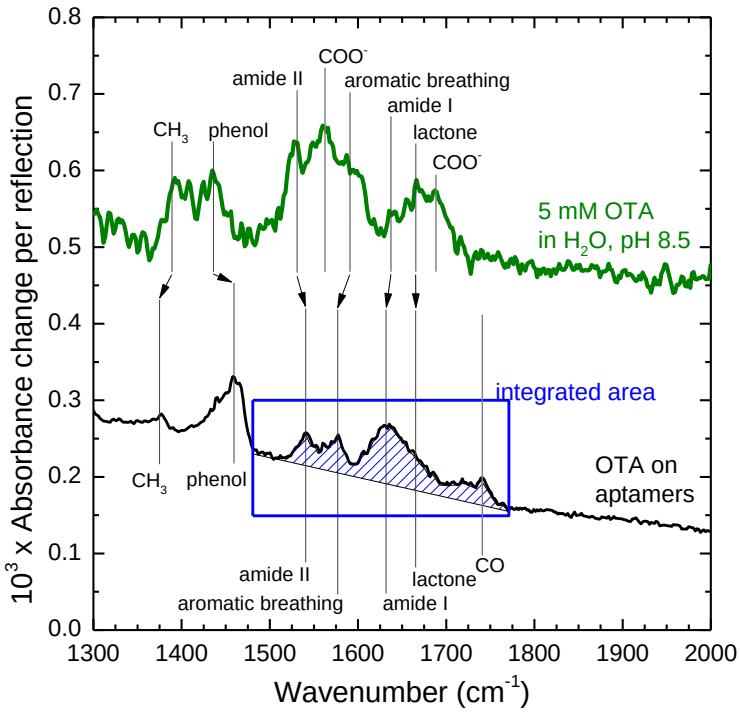


Figure 36: ATR-FTIR spectra of OTA. The black spectrum (p-polarization) is of the surface after association of 1 mM OTA with immobilized aptamers at 600 µM. The reference spectrum is the surface with immobilized aptamers. Green curve is in-situ IR of 5 mM OTA in H_2O, pH 8.5, as discussed in chapter 3. Hatched blue region was integrated for quantitative analysis.

When comparing the spectra of OTA on an aptamer-surface with OTA in solution it becomes apparent, that the spectrum changes, but retains the same general form. Two large massifs around 1550 and 1650 cm^{-1} are visible on surfaces and in solution, and some of the peaks remain at similar positions. OTA on the surface (black spectrum) exhibits a peak at 1663 cm^{-1} which can probably be assigned to lactone. The peak at 1632 cm^{-1} is from the amide I mode of OTA, while the bands at 1574 and 1540 cm^{-1} can be associated with the aromatic breathing of benzene rings and amide II, respectively. The peak at 1460 cm^{-1} is from the decoupled phenol group, and the COO^- and CH_3 mode can also be found at 1375 cm^{-1}. Unlike in solution, OTA on the surface also exhibits a peak at 1741 cm^{-1} that could not be clearly attributed, but its position suggests a carboxyl C=O mode, which might be of the re-protonated acid group of OTA.

The intensity of the lactone groups is reduced in relation to the other peaks, indicating at least partial ring-opening. The appearances of the CO bands with the disappearance of the COO^- peaks indicate a complete re-protonation of OTA upon binding with the aptamers. Therefore we suppose that the OTA bound to the aptamers is completely protonated, but partially in its open-ring and partially in its normal (closed) form.

The difference of IR-spectra (change of cross-section) of OTA in solution (green spectrum) and on aptamers (black spectrum) stems from the different media (liquid/air) and the interaction of OTA with its aptamers, due to van der Waals interactions and hydrogen bonds between the two. These interactions have an impact on the peak intensity, and can also cause peak shifts (indicated by arrows in the figure).

The quantification of molecules on surfaces by ATR-FTIR, as described more profoundly in annex I, allows the calculation of the number of molecules on the surface from IR-spectra. In order to quantify, the characteristic cross-section of a molecules absorbance A_S^0 has to be known at a certain concentration in solution. For this the IR bands which are specific for the molecule are obtained by calibration measurements at known concentrations in liquid phase. It is necessary that the molecules are homogeneously dispersed in the solution in order to retrieve a linear relationship of IR-

absorption and solution concentration. As the quantification relies on the cross-section of OTA being the same in solution and on surfaces the result of the quantification is probably inaccurate to a certain degree.

The slope ($m = 0.0059 \frac{cm^{-1}}{mM} = \frac{A_S^0}{c}$) from the fit of the calibration curve in the region 1475-1775 cm^{-1} (chapter 3.3.2.1) is used for the quantification of OTA. The infrared penetration depth is wavelength dependent and is therefore calculated in the middle of the integration range at 1612.5 cm^{-1} to be δ = 467 nm. Another factor in this calculation is the refractive index of OTA on surfaces and OTA in solution. In dry state OTA has a refractive index of n = 1.5.[105] The OTA concentration in solution is relatively low so we consider the refractive index to be close to the one of water at the wavenumber 1612 cm^{-1} (n = 1.36). The refractive index does not have a very strong impact on the final result of number N of molecules on a surface. For example changing the refractive index in solution from n = 1.36 to 1.5 results in a 9% change of N. The number of molecules on the surface N is described with the two populations $N_{\parallel}$ and $N_{\perp}$, the projection of all the dynamic dipoles onto the surface plane and surface normal, respectively. These two populations can then be calculated for OTA on surfaces from the absorption in liquid in s-polarization A_S^0 at a given concentration ($A_S^0 = c_{OTA} \cdot m = 0.14\ cm^{-1}$ with a concentration of $c_{OTA} = 25\ mM$) with:

$$N_{\parallel} = 1.73 \cdot 10^{15} A_S$$

$$N_{\perp} = 4.01 \cdot 10^{15} A_P - 3.64 \cdot 10^{15} A_S$$

where A_S and A_P are the absorption per reflection of OTA on surfaces in s- and p-polarization.

The final number of molecules on the surface is then calculated with:

$$N = N_{\parallel} + N_{\perp}$$

A quantitative analysis with the results from the calibration measurements in chapter 3 was conducted. The integrated intensities of OTA on the surface in the region 1475 – 1775 cm^{-1} are $A_{1475-1775,P} = 8.5 \cdot 10^{-3}\ cm^1$ and $A_{1475-1775,S} = 8.0 \cdot$

$10^{-3}\ cm^{1}$. With these intensities the surface density of OTA (black spectrum), is calculated to be $N_{OTA} = 1.9 \cdot 10^{13} cm^{-2}$.

Sometimes in literature pretreatments of aptamers are described before the interaction aptamer – target is conducted.[230] This is done so the aptamers favor the structure necessary for binding the analyte and usually consists of treating the aptamers with the buffer solution for a certain duration without the analyte, before adding the analyte. In our experiments no difference was observed, therefore pre-treatments were not applied.

The interaction OTA - aptamer in the black spectrum was carried out on a surface with an aptamer density of $N_{apta} = 1.61 \cdot 10^{14} cm^{-2}$. This means that $\eta = \frac{N_{OTA}}{N_{apta}} = 12\%$ of the aptamers are bound to OTA, even with the very high aptamer surface density. In order to study the impact of steric hindrance at high densities, a test was conducted to see if lower aptamer densities would also bind OTA in measurable quantities. An association with OTA was carried out on surfaces where only one activation and aminolysis reaction had been conducted. No clear indication of association with OTA could be observed with ATR-FTIR, underlining the necessity of improving the aptamer density by repeating the activation and aminolysis reactions.

4.3.3 Regeneration of aptamers

(A) Study of regeneration by IR

The regeneration buffer based on TRIS, EDTA and methanol (1 ml of methanol/(10 mM TRIS, 1 mM EDTA, pH 9) (20:80, v/v) has been proven to efficiently remove OTA bound to aptamers. It was introduced by Cruz-Aguado and Penner, who applied the SELEX procedure to find the aptamer.[128] The IR spectra in Figure 37 represent surfaces after association of OTA with its aptamers and after the subsequent regeneration of OTA.

The reference spectra are the aptamer-surface on the left, and the surface after first regeneration on the right. The black spectrum shows the surface after the first association with 1 mM OTA in BB-Aguado, pH 8.5. The red spectrum was taken after the regeneration was conducted. Then another association with 1 mM OTA in BB-Aguado, pH 8.5 (pink curve) was carried out, before the aptamers were regenerated again (green curve).

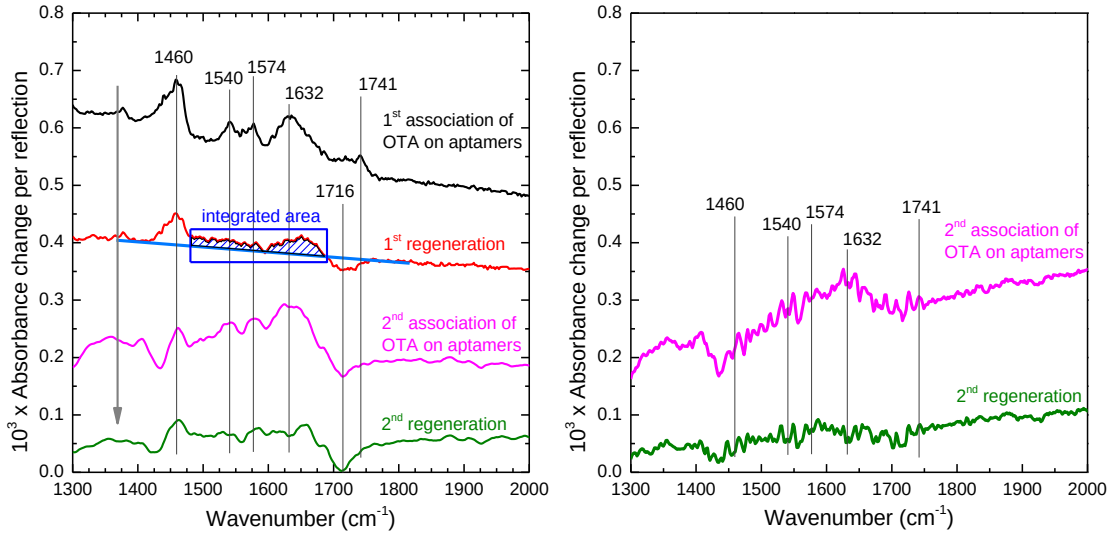


Figure 37: ATR-FTIR spectra (p-polarization) of association and regeneration of OTA with its aptamers on surfaces. Left side: the reference spectrum is the aptamer surface. Right side: the reference spectrum is the surface after the first regeneration. Black: first association of OTA with aptamers. Red: subsequent regeneration. Pink: second association with OTA. Green: succeeding regeneration. Hatched blue region was integrated for quantitative analysis with baseline indicated in light blue.

The surface after association (black) was already discussed above. After the first regeneration (red curve) a negative peak at 1716 cm^{-1} can be seen, which can be associated with the stretching mode vibration of the carboxyl C=O bond, indicating a deprotonation of the surface COOH groups by the alkaline regeneration buffer. The peak at 1460 cm^{-1}, assigned to the decoupled phenol mode of OTA, remains comparatively stronger than the other peaks (60% remaining intensity vs. 37% for the region 1475-1690 cm^{-1}). This indicates an increase in COO^- groups, strengthening the

hypothesis of deprotonation. The remaining peaks at 1632, 1574 and 1540 cm^{-1} are strongly reduced, which indicates the partial the removal of OTA from the surface.

After the second association with OTA (pink curve) the spectrum displays more noise, but the representative peaks of OTA (1632, 1574 and 1540 cm^{-1}) are nevertheless visible again over the background. When the surface after the first regeneration is taken as reference (rights side in Figure 37), the spectra exhibit a lot of noise, but nevertheless the OTA specific peaks can be supposed in the spectra. The second regeneration (green spectrum) again reduces the peaks of OTA, while further deprotonating the remaining acid groups on the surface (the negative peak at 1716 cm^{-1} increases). This is especially visible on the right side with the first regeneration as reference, where the surface nearly returns to its original state (as indicated by the nearly flat line).

A quantitative analysis of the OTA molecules removed from the surface poses the problem of the negative peak at 1716 cm^{-1}. In order to avoid this peak the integration was conducted in the region 1475 - 1690 cm^{-1} instead of 1475 - 1775 cm^{-1}. This allows a determination of the OTA molecules remaining on the surface with a certain underestimation of this value. If the same region is fitted for OTA on aptamers (black spectrum) the surface density of OTA is underestimated by 20%.

The initial OTA surface density before the regeneration was $N_{OTA} = 1.9 \cdot 10^{13} cm^{-2}$. Adjusting the quantitative analysis by 20% to counteract the underestimation, we find a surface density of remaining OTA of at least $N_{OTA-remaining} = 0.7 \cdot 10^{13} cm^{-2}$ (with $A_{1475-1690,P} = 2.7 \cdot 10^{-3} cm^{-1}$ and $A_{1475-1690,S} = 2.6 \cdot 10^{-3} cm^{-1}$). This corresponds to a removed OTA surface density of $N_{OTA-removed} = 1.2 \cdot 10^{13} cm^{-2}$ after the first regeneration, which means that around 63% of the OTA on the surface was removed.

The second regeneration is not reliably quantifiable due to elevated noise and background.

(B) Study of regeneration by UV-vis spectroscopy

The study of the regeneration of OTA from its aptamers by UV-vis spectroscopy was carried out to corroborate the results obtained by ATR-FTIR. With the calibration

conducted in chapter 3.3.2 a quantitative analysis of the regeneration buffer is conducted, after the regeneration of OTA from its aptamer has taken place in it. The UV-vis experiment was carried out after three cycles of association and regeneration had been carried out on the surface, as partially displayed above in Figure 37. As the spectra display a high noise to signal ratio quantitative analysis by IR was not possible. However, after regeneration the UV-vis spectrum of the buffer showed no OTA. To increase the intensity of OTA in the regeneration buffer, the cycle of OTA-association with its aptamers and regeneration of OTA from the aptamers was repeated five times, while reusing the same regeneration buffer. This repetition resulted in a high enough quantity of OTA for detection. The UV-vis spectrum is displayed in Figure 38. The regeneration buffer without OTA was used as reference. The figure also displays the spectrum which was obtained during the calibration measurements in chapter 3.3.2, where the regeneration buffer was spiked with different concentrations of OTA. Apart from the noise, both spectra have their maximum at 380 nm and show very similar intensity, indicating similar quantity of OTA molecules in the solution.

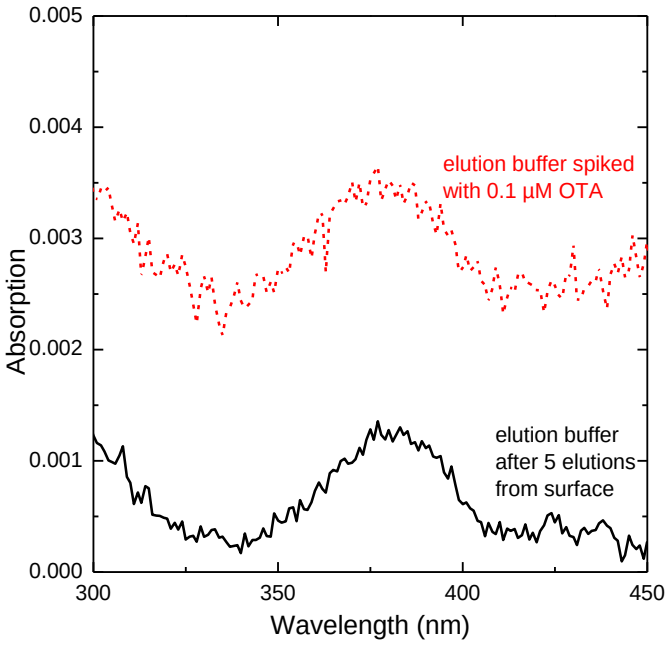


Figure 38: UV-vis spectra of (black curve) regeneration buffer after five regenerations of OTA from surface, and (red) of regeneration buffer spiked with 0.1 µM OTA, as obtained during calibration measurements in chapter 3.3.2. The reference spectra are the regeneration buffer without OTA.

The calibration measurements conducted in chapter 3.3.2 yielded a slope of m = 0.452 nm/µM. An integration of the regeneration buffer in the region 320 – 430 nm yields an integrated surface under the curve of $S_{int} = 0.044\ nm$. With this we can calculate the OTA concentration in the solution:

$$c_{OTA} = \frac{S_{int}}{m} = 0.097 \mu M$$

This leads us to the number of OTA molecules in the solution (with Avogadro constant N_A and volume V = 1 ml):

$N_{OTA,sol} = c_{OTA} \cdot N_A \cdot V = 5.84 \cdot 10^{13}$ molecules

Taking into account the 5 repetitions, the surface density of OTA on the prism before it was removed by the regeneration buffer is calculated with (with number of repetitions n = 5, prism surface $S_{prism} = 3\ cm^2$):

$$N_{OTA,surf} = \frac{N_{OTA,sol}}{n \cdot S_{prism}} = 0.4 \cdot 10^{13}\ cm^{-2}$$

The difference of the surface densities which were retrieved by UV-vis spectroscopy and by ATR-IR ($N_{OTA,UV-vis} = 0.4 \cdot 10^{13}\ cm^{-2}$ and $N_{OTA-removed,IR} = 1.2 \cdot 10^{13}\ cm^{-2}$, respectively) is a factor 3. This difference can be explained by the multiple associations and regenerations performed without a perfect quantitative correlation with OTA bound to aptamers on the surface. Another influence is the IR-cross-section of OTA which is not identical in liquid or on surfaces, which affects the IR-quantification, as discussed in chapter 4.3.2.

4.3.4 Non-specific interaction of aptamers with warfarin

In order to determine the specificity of the aptamer for the detection of OTA, it is tested in the presence of a chemical with similar structure. In the case of OTA, warfarin (Figure 39) is often used.[82,128,223,224] Warfarin not only displays a similar structure, but also uses the same binding sites on human serum albumin, which is the main mean of transport for OTA in the human body.

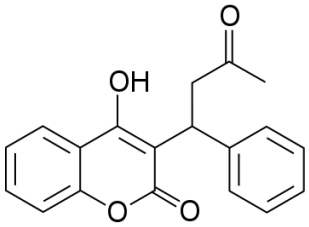


Figure 39: Chemical structure of warfarin.

The ATR-FTIR spectrum of an association with warfarin on aptamers is displayed in Figure 40, the reference spectrum being the surfaces with immobilized aptamers. The spectrum of OTA after association with its aptamer is also displayed for comparison (black line). The association with warfarin was conducted under the exact same conditions as the association with OTA is normally carried out (1 mM warfarin in BB-Aguado, pH 8.5).

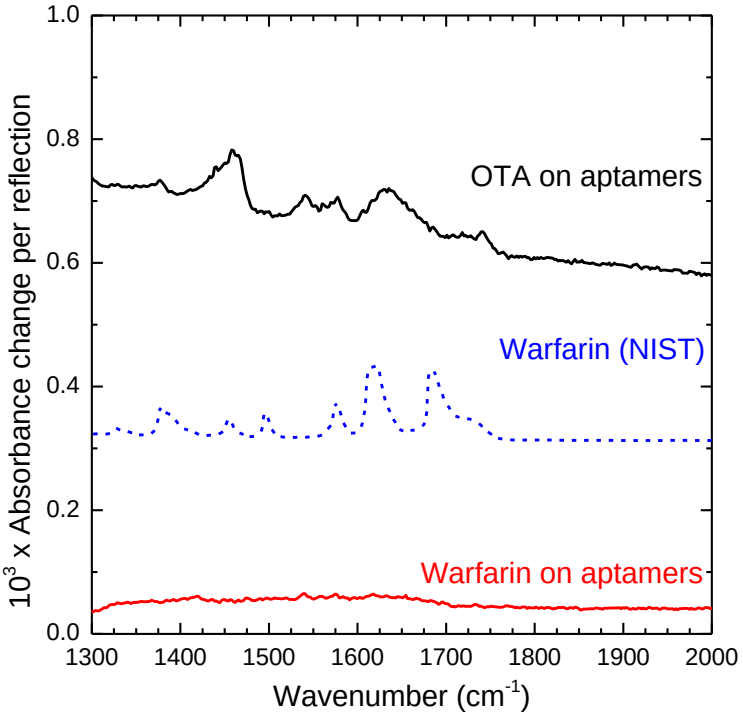


Figure 40: ATR-FTIR spectra of non-specific adsorption of warfarin on aptamers. Red: ATR-FTIR spectrum (p-polarization) of surface with immobilized aptamers after association with warfarin. The reference spectrum is the aptamer surface before adding warfarin. Black: (p-polarization) surface after association with OTA, as shown before. The reference spectrum is the surface with immobilized aptamers. Dotted blue: spectrum of warfarin as provided by NIST (solid – KBR pellet).[237]

The spectrum after association with warfarin only exhibits noise. Comparing the spectrum of warfarin on the surface with the spectrum from NIST, no comparable peaks are visible. Comparison with the spectrum of OTA on the surface also indicates that no association of warfarin took place. This indicates that the aptamer has no or very little affinity towards warfarin, so it is a good choice for a selective and specific interaction with OTA.

4.4 Conclusion

In this chapter we presented the strategy for immobilization of NH_2-terminated aptamers on functionalized silicon surfaces. The aminolysis reaction yield was increased by optimizing the reaction buffer in respect to: buffer composition and pH, aptamer concentration. Once an ideal buffer for the aminolysis reaction was found the yield was further increased by repeating activation and aminolysis reactions until no further immobilization of aptamers took place on the surfaces, resulting in an aptamer surface density of $N_{apta} = 1.6 \cdot 10^{14}\ cm^{-2}$. The interaction of OTA with its aptamer on surfaces was successfully shown and quantified for the first time by ATR-FTIR, yielding an OTA surface density of $N_{OTA} = 1.9 \cdot 10^{13}\ cm^{-2}$ on the aptamers. The regeneration of aptamers (removal of OTA) was studied with two methods. Quantification of the surfaces by ATR-FTIR showed that 63% (or $1.2 \cdot 10^{13}\ cm^{-2}$) of the OTA was removed, while quantification of the regeneration buffer solution by UV-vis spectroscopy yielded a density lower by a factor 3. Finally, the specificity of the aptamer towards OTA was demonstrated by using a chemically similar molecule (warfarin), towards which the aptamer showed no affinity.

Having seen the interaction of OTA with its aptamers directly by infrared spectroscopy, we can now look at the interaction indirectly with fluorescence. This interaction will be done on the biochip architecture, as explained in the next chapter.

5 FLUORESCENT BIOCHIPS FOR OTA DETECTION

5.1 Introduction

The goal of this chapter is to develop a biochip architecture based on an a-$Si_{1-X}C_X$:H thin film deposited on a back-reflector for a sensitive and multiplex detection. The first role of this amorphous silicon carbon alloy is to act as a reliable basis for the immobilization of probes via stable Si-C bonds. The second role of the architecture is to enhance the sensitivity of the fluorescence detection by the presence of an aluminium back reflector allowing constructive interference.

The fluorescence yield depends on the distance of the fluorophore from the substrate surface, and also the refractive index of the substrate. Crystalline silicon is not a good substrate for fluorescence measurements because of its high refractive index (energy gap 1.12 eV with n = 3.4 at 635 nm). Therefore this film of a-$Si_{1-X}C_X$:H is chosen as it has tunable optical properties. Increasing the carbon content enlarges the optical band gap and thus reduces the refractive index. It was demonstrated that a film containing 10 – 20% carbon has minimal optical losses and can thereby be tuned for fluorescence detection, as displayed in Figure 41 for Cy5 (wavelength excitation 635 nm, and emission 670 nm).[20] Moreover such a film can be deposited by PECVD on a large variety of substrates. This enables an increase of the fluorescence yield in presence of a metallic back-reflector covered with a-$Si_{1-X}C_X$:H for constructive interference, depending on the film-thickness. The ideal thickness for Cy5-labelled oligonucleotides is a 44 nm a-$Si_{0.85}C_{0.15}$:H layer. [20]

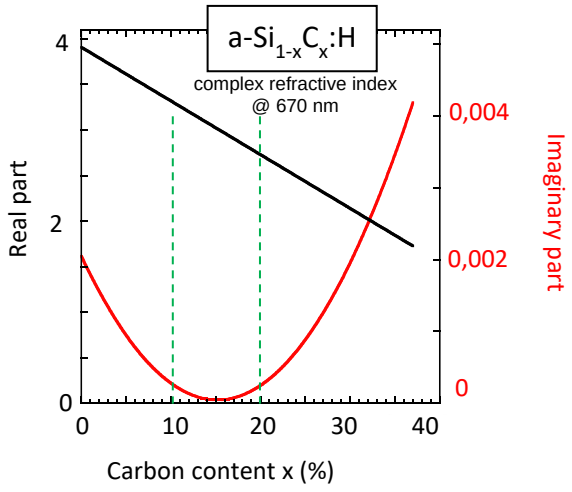


Figure 41: Refractive index of a-$Si_{1-X}C_X$:H films in dependence of their carbon content.

On this layer the same steps for surface functionalization are carried out as before, except that now the aptamers and oligonucleotides are deposited by robotic spotting, which enables the immobilization of various aptamers and oligonucleotides on one slide, giving it its biochip (multiplex) capabilities.

The indirect detection by fluorescence is based on two detection strategies "signal OFF" and "signal ON", which are widely used in literature.[120,225,226,238–240] For the "signal OFF" detection method (Figure 42, left) a short complementary oligonucleotide labelled with Cy5 is hybridized to the aptamer, resulting in a fluorescence signal. Successful association of OTA with the aptamer removes the complementary strands, resulting in a decrease of fluorescence intensity. In the "signal ON" method (Figure 42, right) the immobilized aptamers are labelled with Cy5, while the short complementary oligonucleotides are modified with a quencher (BHQ2), which suppresses fluorescence emission of nearby fluorophores. Successful association of OTA removes the quencher and therefore an increased fluorescence signal can be detected.

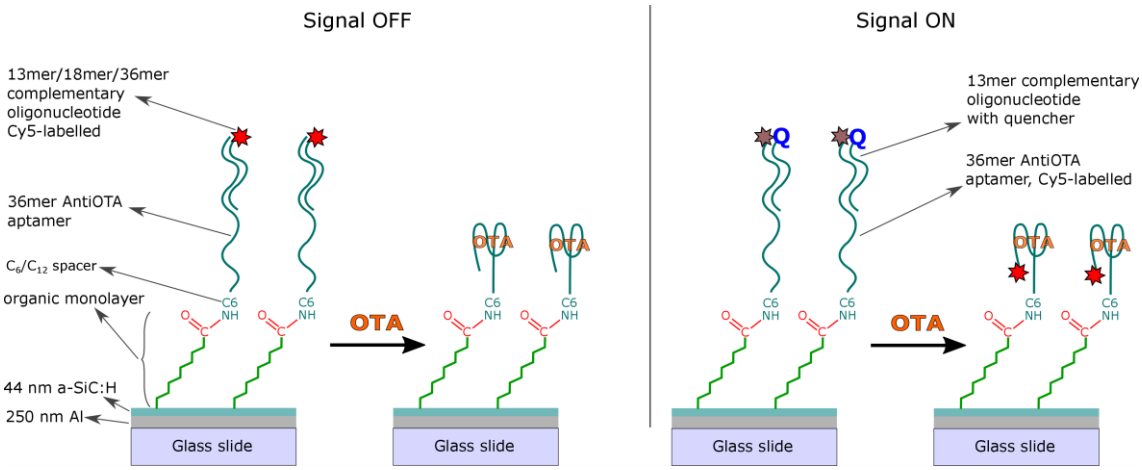


Figure 42: Strategy for OTA detection by fluorescence. Left side: "signal OFF" method, hybridization with a Cy5-labelled complementary strand. Right side: "signal ON" method, immobilized aptamer is Cy5-labelled; hybridization with quencher-labelled complementary oligonucleotide quenches Cy5.

Before the experiments on the biochip architecture are studied, the calibration of the deposition of the a-$Si_{1-x}C_x$:H-layer by PECVD is discussed, in order to have the optimal layer thickness for a good signal enhancement.

The two fluorescence detection methods “signal OFF” and “signal ON” will be studied for the detection of the interaction of OTA with its aptamer. The increase of stringency and the stability of the oligonucleotide immobilization will be discussed. The duplex stability and interaction of OTA with its aptamer will be first studied by comparing different buffers. Then the influence of the aptamer orientation on the surface (3’ and 5’), the position on the fluorophore (near or far from the surface) and different complementary strand lengths (13, 18, 36 mer) will be compared.

5.2 Materials and Methods

5.2.1 Chemicals and substrates

In our experiments all chemicals were reagent grade or higher and most were described in previous chapters. Ethanolamine ($NH_2CH_2CH_2OH$, redistilled, 99.5%) was supplied by Aldrich.

The oligonucleotides and aptamers which are used are displayed in Table 11 and were supplied by Eurogentec, France. The control strands are spotted as control for the spotting process. The OTA-binding aptamer (noted as “Apt”) was used with modifications on the 3’-side and on the 5’-side, with two different spacer lengths (C_6 and C_{12}), and in one case labelled with the fluorophore Cy5. Five different complementary oligonucleotides are used and are indicated by a “c” in their name. They have different lengths (13, 18 and 36mer) and are modified with the cyanine dye Cy5 and the quencher BHQ2. The oligonucleotides are dissolved in ultrapure water to form their 100 µM stock solution and are stored at -20°C.

Table 11: Oligonucleotides and aptamers used for experiments, including their sequences and modifications.

Name	**Function**	**Sequence 5' → 3'**	**Mod. 3'**	**Mod. 5'**
Control	Control	AAC-GCC-CAT-CTT-AAA-ATC-GAC-GCC-T	NH_2-C_6	Cy5
Apt-3'C6	Aptamer	GAT-CGG-GTG-TGG-GTG-GCG-TAA-AGG-GAG-CAT-CGG-ACA	NH_2-C_6	
Apt-5'C12	Aptamer	GAT-CGG-GTG-TGG-GTG-GCG-TAA-AGG-GAG-CAT-CGG-ACA		NH_2-C_{12}
Apt-3'C6-5'Cy5	Aptamer	GAT-CGG-GTG-TGG-GTG-GCG-TAA-AGG-GAG-CAT-CGG-ACA	NH_2-C_6	Cy5
cApt13-5'Cy5	Hybridization	CCC-ACA-CCC-GAT-C		Cy5
cApt18-3'Cy5	Hybridization	CGC-CAC-CCA-CAC-CCG-ATC	Cy5	
cApt18-5'Cy5	Hybridization	TGT-CCG-ATG-CTC-CCT-TTA		Cy5
cApt36-5'Cy5	Hybridization	TGT-CCG-ATG-CTC-CCT-TTA-CGC-CAC-CCA-CAC-CCG-ATC		Cy5
cApt13-3'BHQ	Hybridization	CCC-ACA-CCC-GAT-C	BHQ2	

The base substrates for the biochips are standard microscope slides which are cleaned meticulously before further handling. The slides are soaked in a TFD4-solution for 15 minutes before thorough scrubbing between fingers with latex gloves. Then the slides are rinsed well with ultra-pure water and immersed in ethanol for 30 minutes. Afterwards the slides are again rinsed carefully with ultra-pure water and then immersed in Piranha solution for 30 minutes. Then the slides are again rinsed thoroughly with ultra-pure water and dried under a nitrogen flow. A 250 nm thick aluminium layer is deposited by thermal evaporation (cf. annex III), before a 44 nm amorphous silicon-carbon layer (a-$Si_{0.85}C_{0.15}$:H) is deposited by PECVD (cf. annex IV).

5.2.2 Transfer of protocols from crystalline silicon

HF-etching for hydrogenated silicon surfaces:

The oxide of the a-$Si_{0.85}C_{0.15}$:H-layer is removed by HF-vapor etching. For this a container containing 50% HF-solution is opened and carefully stirred. The slide is then

held for 15 seconds over the open container with the a-$Si_{1-x}C_x$:H side towards the opening.

Photochemical hydrosilylation of undecylenic acid and activation reaction with EDC/NHS are carried out as before (cf. chapter 2.3).

5.2.3 Preparation of solutions for spotting

The aptamers and oligonucleotides are diluted from their stock solution to 10 µM concentration in two buffers. The buffer used was optimized for the aminolysis reaction of AntiOTA-aptamers on crystalline silicon as described in chapter 4, and is a 150 mM phosphate buffer with 0.01% SDS, pH 8.5. The aptamers are denaturized by heating to 95°C for 5 minutes and rapid cooling in ice for 10 minutes. The solutions (each 20 µl) are then deposited in a microplate for robotic spotting (annex V). The spotting is carried out on a Biorobotics MicroGrid II microarrayer with a controlled climate (~60% humidity and 15-18°C room temperature). After the spotting is finished, the slides are stored overnight in a humidifier with a controlled 75% humidity.

5.2.4 Blocking of remaining active surface sites

The remaining active sites on the surfaces after robotic spotting are blocked. For this, the slides are immersed in 30 ml of a 50 mM ethanolamine in PBS 1X, pH 8.5 in a glass tank on a shaker for 1 hour. Then they are cleaned for 2 min in glass tanks with ultrapure water on a shaker and finally dried.

5.2.5 Hybridization with complementary oligonucleotides

The aptamers are hybridized with the Cy5-labelled complementary strands. The complementary strands are diluted to 1 µM in PBS 1X. The oligonucleotides are then denaturized by 5 minutes heating to 95°C and 10 minutes cooling in ice.

The hybridization is conducted in a hybridization chamber, with PBS 1X in the reservoirs for a controlled climate inside the chamber. 20 µl of oligonucleotide solution is deposited on each hybridization-zone and covered with a coverslip. The hybridization chamber is closed hermetically and immersed in a water bath at 25°C or 45°C (depending on the experiment) for 1h30. Then the slides are removed from the chamber and each zone carefully rinsed with 1 ml PBS 1X from a micropipette, before cleaning in glass tanks on a shaker is conducted twice with PBS 1X for 10 min. Finally the slides are immersed in ultrapure water for 15 seconds before drying.

5.2.6 Association with OTA

OTA is pre-dissolved in ethanol (34.7 mM) from its dry state. Then it is further diluted in its buffer. Two buffers were used: *BB-Aguado* (10 mM TRIS, 120 mM NaCl, 20 mM $CaCl_2$, and 5 mM KCl; pH 8.5), and *SB-Aguado* (10 mM HEPES, 120 mM NaCl, 5 mM KCl, 20 mM $CaCl_2$; pH 7). BB-Aguado and SB-Aguado are the binding and selection buffer, respectively, which were used during the SELEX-process of AntiOTA.[128]

The association is carried out in a hybridization chamber, with buffer solution in the reservoirs for a controlled humid environment during the association. 20-25 µl of the OTA-solution is deposited on each zone of the slide and then covered with a coverslip. The hybridization chamber is closed hermetically and then immersed for 1 hour in a water bath at 25°C. Next the slides are removed from the chambers and carefully rinsed with 1 ml buffer solution from a micropipette, before cleaning in a glass tank on shaker with buffer solution for 5 minutes. The slides are then dipped in ultrapure water for 15 seconds before drying.

5.3 Results and discussion

5.3.1 PECVD-calibration

In order to be in the optimal conditions with the right thickness and carbon content for ideal fluorescence augmentation the depositions of the in-house PECVD were calibrated concerning the deposition rate and the carbon content. The deposition rate depends on the gas flow, but also on the methane content of the deposition. Depositions were carried out on silicon wafers and glass slides at the same time and two methods were combined for analysis. Scanning electron microscopy (SEM, cf. annex II) allows to measure the thickness of the thin layers by imaging the cross-section of depositions on crystalline silicon wafers. UV-vis spectroscopy enables measuring the thickness, refractive index and carbon content of depositions on glass slides.

5.3.1.1 Calibration by SEM

For the calibration by SEM the PECVD depositions were carried out on crystalline silicon for 30 min with three different carbon contents. The SEM images of the cross-section of the wafers with layers of a-$Si_{0.9}C_{0.1}$:H, a-$Si_{0.85}C_{0.15}$:H and a-$Si_{0.8}C_{0.2}$:H are displayed in Figure 43. Imaging of these layers with SEM is challenging, as crystalline and amorphous silicon are chemically very similar and topographical differences are relatively low due to the cross-section analysis. The deposition rate is calculated by dividing the layer thickness by the deposition time, the results are displayed in Table 12. At the lowest carbon content (10% C incorporated in the layer) the deposition is the fastest with 1.33 µm/h. It drops to 1.08 µm/h for the a-$Si_{0.85}C_{0.15}$:H layer and remains nearly stable (1.06 µm/h) when the carbon content is further increased to 20%.

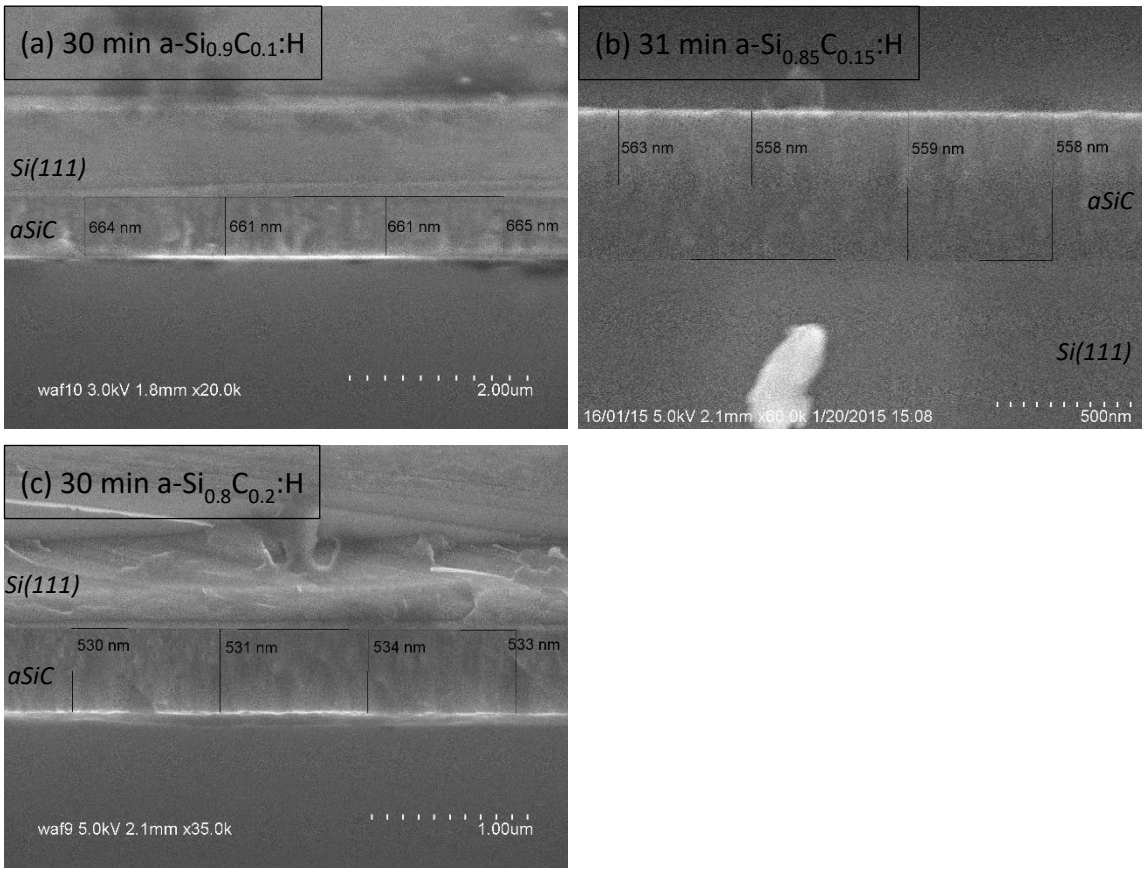


Figure 43: SEM-images of Si(111)-wafer cross-sections after three 30 min PECVD-depositions with carbon content of 10% (a), 15% (b) and 20% (c).

Table 12: Deposition rates of a-$Si_{1-X}C_X$:H PECVD-depositions displayed in Figure 43.

C%	Deposition time (min)	Average thickness (nm)	Deposition rate (µm/h)
10	30	662.8	1.33
15	31	559.5	1.08
20	30	532.0	1.06

Another question which arises for the PECVD-deposition is the uniformity of the deposition rate when changing the duration (i.e. is the deposition faster/slower in the beginning or not). Therefore further depositions were carried out, with 5 min and 15 min duration. The SEM-images of the cross-sections are displayed in Figure 44. With

shorter deposition times and hence thinner layers it becomes increasingly difficult to distinguish between the amorphous silicon layer and crystalline silicon below. Therefore the 5 min deposition (b) was the shortest deposition analyzable by SEM. The calculated deposition rates are displayed in Table 13 and compared to the deposition rate achieved during the 30 min deposition. The deposition rates for the three thicknesses converge around 1.10 µm/h, with little difference between the three thicknesses.

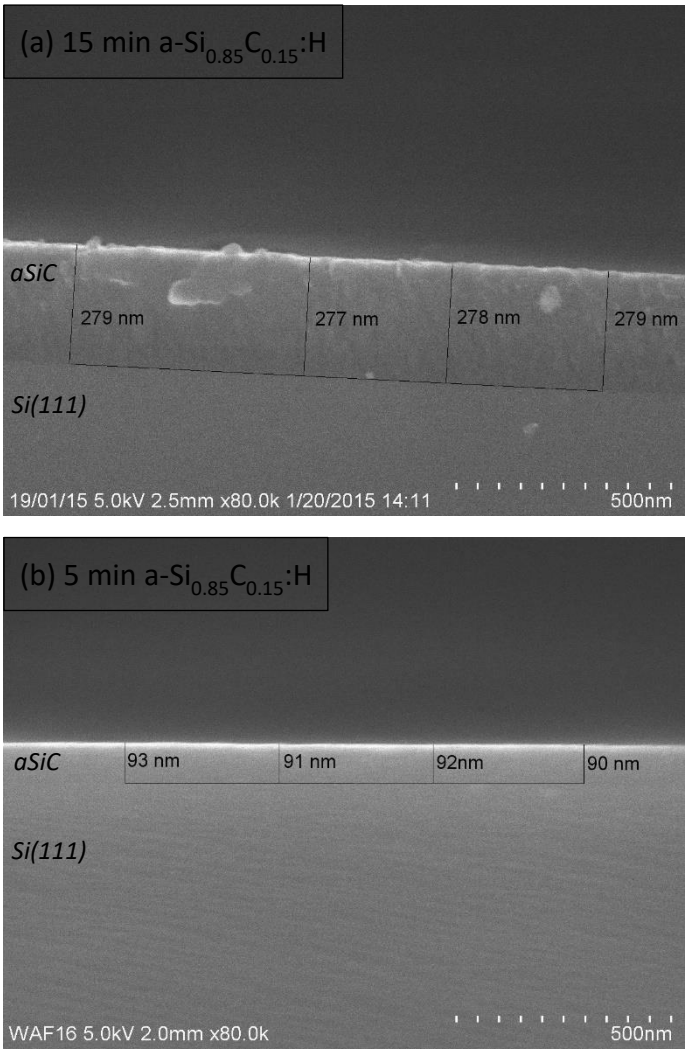


Figure 44: SEM-images of Si(111)-wafer cross-sections after 15 min (a) and 5 min (b) PECVD-depositions with carbon content 15%.

Table 13: Average thicknesses and deposition rates of a-$Si_{0.85}C_{0.15}$:H PECVD-depositions displayed in Figure 43 (bottom line) and Figure 44 (1st and 2nd line).

Nominal C%	Deposition time (min)	Average thickness (nm)	Deposition rate (µm/h)
15	5	91.5	1.10
15	15	278.3	1.11
15	31	559.5	1.08

5.3.1.2 UV-vis spectroscopy

The glass slides were covered with a thin layer of a-$Si_{1-X}C_X$:H by PECVD at the same time as the wafers above. They were then analyzed with a UV-vis spectrometer. The resulting curves were analyzed (with Matlab, following the calculation below) to retrieve thickness and refractive index, and subsequently compared with the work of Solomon et al.[241] to retrieve the carbon content in the films.

The wavelength dependent refractive index of the glass slide is estimated with:[242]

$$n_3 = 1.513 - 0.003169 \cdot \lambda^2 + 0.003962 \cdot \lambda^{-2}$$

In order to be able to calculate the transmission through the thin film and the glass substrate some assumptions have to be made. We assume the surface is perfectly flat and we assume a normal light beam with zero divergence. The film is considered to be transparent, even though it is slightly absorbing. The last assumption probably influences the calculation less than the first ones.

For the calculation it is necessary to consider what happens at the interfaces. With the refractive index n_1 of air and n_2 of the amorphous silicon thin film it is possible to calculate the reflection coefficients r_{12} and r_{23} at the interfaces between air and the a-$Si_{1-X}C_X$:H -thin film, and the a-$Si_{1-X}C_X$:H -thin film and glass, respectively:[243]

$r_{12} = \frac{n_1 - n_2}{n_1 + n_2}$ and $r_{23} = \frac{n_2 - n_3}{n_2 + n_3}$

Then the *equivalent reflection coefficient* for a single layer film is given by:[243]

$$r = \frac{r_{12} + r_{23} e^{-2i\delta}}{1 + r_{12} r_{23} e^{-2i\delta}}$$

and δ is the phase delay of passing the film (with the film-thickness t):

$$\delta = \frac{2\pi n_2 t}{\lambda}$$

The reflectance is then calculated with:

$$R = |r|^2$$

Taking into account a reflectance of 4% for the interface glass-air, the simulated transmittance results in:

$$T_{sim} = 0.96 * (1 - R)$$

The UV-vis transmission spectra of three 30 min a-SiC depositions with different carbon concentrations and one 15 min deposition of a-$Si_{0.85}C_{0.15}$:H are displayed in Figure 45 (red curves). The simulated transmittance curves are obtained by tuning the parameters "n_2" and "t" until it is in good accordance with the measured curve. The simulated transmittance curves are displayed in blue. The thereby obtained thicknesses and deposition rates are displayed in Table 14, and are very similar to the results obtained with SEM. The lowest carbon content (10%) exhibits the highest deposition rate. The rate drops when the carbon content (15%) is increased, but nearly stabilizes for the highest concentration (20%).

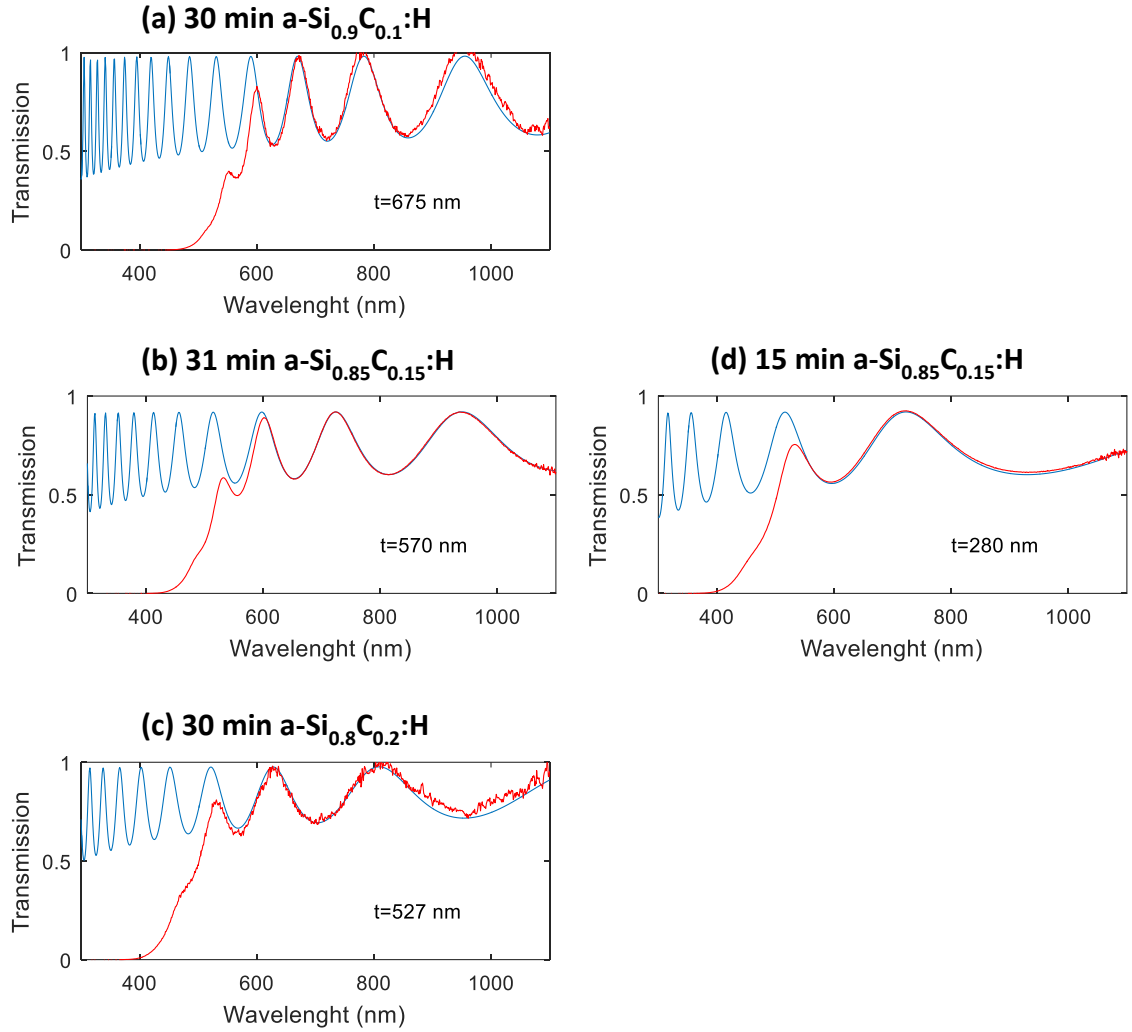


Figure 45: UV-vis transmission spectra of PECVD depositions of a-Si_XC_{1-X}:H thin films on glass (red) and its simulation (blue). (a) 30 min deposition of a-$Si_{0.9}C_{0.1}$:H, (b) 31 min of a-$Si_{0.85}C_{0.15}$:H, (c) 30 min of a-$Si_{0.8}C_{0.2}$:H, (d) 15 min of a-$Si_{0.85}C_{0.15}$:H.

Table 14: Thickness and deposition rates of a $Si_{1-X}C_X$:H PECVD-depositions from analysis by UV-vis spectroscopy

Nominal C%	Deposition time (min)	Thickness (nm)	Deposition rate (µm/h)
10	30	675	1.35
15	15	280	1.12
15	31	570	1.10
20	30	527	1.05

The carbon content was calculated with the curves published by Solomon et al. on the PECVD-deposition of a-$Si_{1-X}C_X$:H -thin films.[241] They demonstrated, that the energy E_{04} (optical gap, energy at which the absorption coefficient is 10^4 cm^{-1}) only depends on the gas composition (SiH_4/CH_4 ratio) and is very insensitive to the deposition parameters, such as temperature, total pressure, flow rate and power density. They also showed that the carbon incorporation in the film depends exclusively on the gas composition. The energy E_{04} can be calculated by first taking into account the absorption of the silicon thin film for the transmission:

$$T = 0.96 * (1 - R) * e^{-\alpha t}$$

with the film thickness t and the absorption coefficient α. Inversing this formula yields the wavelength-dependent absorption coefficient:

$$\alpha = -log\left(\frac{T}{0.96 * (1 - R)}\right)/t$$

As the absorption coefficient is implicitly wavelength dependent the wavelength λ could be calculated where $\alpha = 10^4\ cm^{-1}$, in order to retrieve the energy E_{04} with the approximation $E(eV) = \frac{1.2398}{\lambda(\mu m)}$. A simpler method is to plot α (retrieved with the formula above) in dependence of the wavelength, as displayed for the 31 min a-$Si_{0.85}C_{0.15}$:H deposition in Figure 46 (left). Then the energy E_{04} can be calculated from the wavelength, where $\alpha = 10^4\ cm^{-1}$. This energy can be used to find the carbon content with the results given by Solomon et al., as displayed by the green arrows in Figure 46 on the right. The results for the four depositions analyzed by UV-vis spectroscopy are displayed in Table 15. The measured carbon content shows a very good agreement with the nominal values.

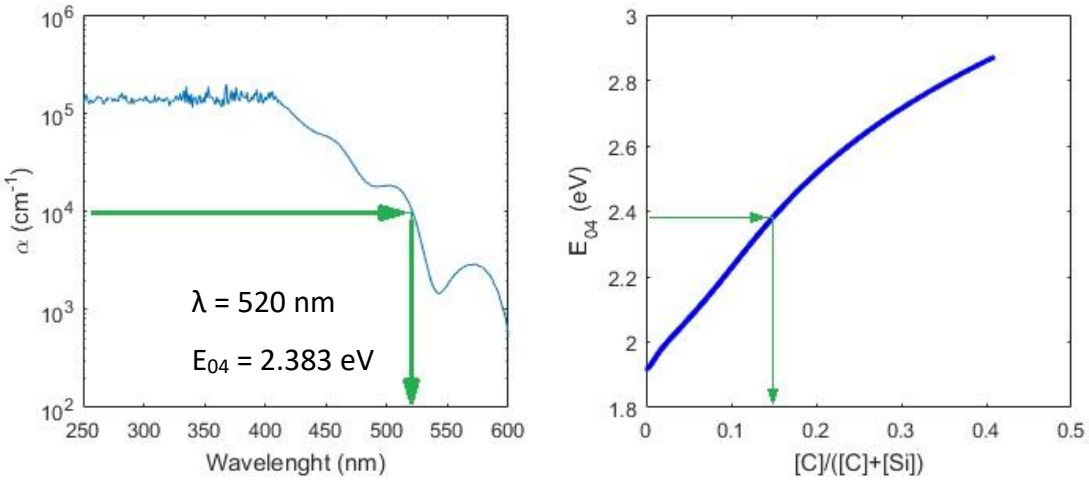


Figure 46: Left: plot of absorption coefficient of the 31 min a-$Si_{0.85}C_{0.15}$:H deposition over wavelength. Right: energy E_{04} (absorption coefficient of 10^4 cm^{-1}) over incorporated carbon in thin film. Adapted from Solomon et al.[241]

Table 15: Carbon content in a-$Si_{1-X}C_X$:H PECVD-depositions from analysis by UV-vis spectroscopy.

Nominal C%	Deposition time (min)	UV-vis: C%
10	30	10
15	15	15
15	31	16
20	30	21

The layer thicknesses (and thereby the deposition rates) which were found by SEM and UV-vis spectroscopy show very good agreement of the two methods. The deposition rates for the a-$Si_{0.85}C_{0.15}$:H layer were found to be 1.08 and 1.11 µm/h by SEM and 1.10 and 1.12 µm/h by UV-vis spectroscopy. Therefore for all conducted depositions a rate of 1.10 µM/h was presumed. The carbon content in the layer was shown to correspond well with the nominal values with only slight divergences.

5.3.2 Fluorescent assays

5.3.2.1 Signal OFF/ON with 13mer complementary strands

The detection methods “signal OFF” and “signal ON” were applied for the first experiments.

Signal OFF

The “control” oligonucleotide and the aptamer Apt-3’C6 were deposited by robotic spotting at 10 µM on the ester-NHS terminated slides. The hybridization was carried out with the complementary strand cApt13-5’Cy5 with a concentration of 1 µM at 45°C. The association with OTA was conducted with 10 µM OTA in BB-Aguado.

The fluorescence images (0.5 s scan time) after all steps (blocking, hybridization and association with OTA) are displayed in Figure 47. After blocking the control spots are clearly visible, and the aptamer spots show no fluorescence signal, which is expected since they are not labelled. After hybridization with the complementary strands the spots with the aptamers can be seen clearly, indicating successful hybridization. The images after association with OTA show a strong decrease of fluorescence signal for both types of spots. A clear difference can be seen between the two types, with the aptamer spots exhibiting a more intense loss.

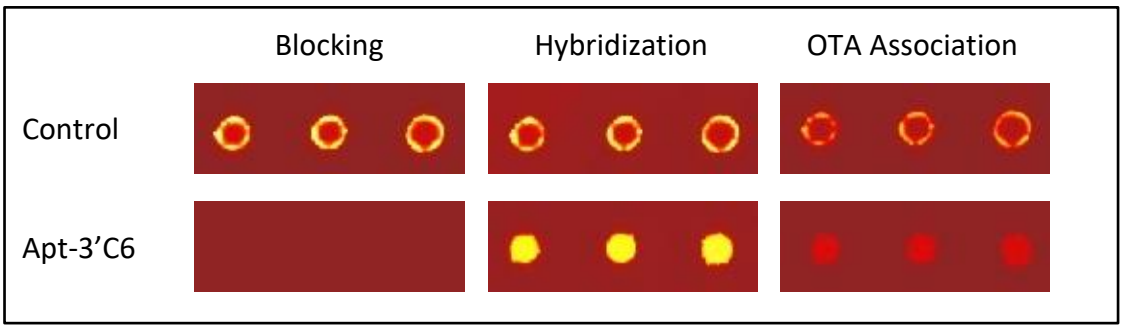


Figure 47: Fluorescence images (0.5 s scan time) of the spotted control oligonucleotide and Apt-3’C6 aptamer.

For further analysis of the spots different values are calculated. The **signal loss** of the spots is calculated with:

$$\mu_{apta} = 1 - {I'_{apta}}/{I_{apta}}$$

where I_{apta} is the fluorescence intensity of the aptamer spots before the reaction, and I'_{apta} the fluorescence intensity after the reaction was carried out (e.g. after hybridization and after association).

The second value takes into account the intensity loss of the control spots for calculating the loss of the aptamer spots, and is called **relative loss** for "signal OFF". For this we assume that the bleaching of the fluorophores displays the same behavior on the control spots and the Cy5-labelled complementary strands. To retrieve the relative loss first the signal loss of the control spots is calculated with:

$$\eta_{cont} = {I'_{cont}}/{I_{cont}}$$

where I_{cont} is the fluorescence intensity of the control spots before the reaction (after hybridization), and I'_{cont} the fluorescence intensity after the reaction (after association). With this we can calculate the relative signal loss of aptamer spots, which takes into account the loss of the control spots:

$$\frac{\Delta I}{I} = \frac{\eta_{cont} I_{apta} - I'_{apta}}{\eta_{cont} I_{apta}} = 1 - \frac{I'_{apta}}{\eta_{cont} I_{apta}}$$

The histogram of the fluorescence intensities of the spots is displayed on the left in Figure 48, and the signal loss of the control and aptamer spots after association with OTA is displayed on the right. Mean values of the spots were used for the analysis because the control spots are not uniform.[244] The intensity of the control spots is slightly decreased after hybridization ($\mu_{cont} = 17\%$), but is strongly reduced after the association ($\mu_{cont} = 52\%$). The Apt-3'C6 aptamer shows, as expected, zero intensity after the blocking, and increases strongly by the hybridization with its Cy5-labelled complementary strands. The association with OTA strongly decreases the measured fluorescence of the aptamer spots ($\mu_{apta} = 88\%$), while the control spots showed a

significantly lower decrease (52%). The higher loss of the Apt-3'C6 indicates removal of complementary strands by the association.

The relative loss of the aptamer spots can then be calculated with eq. 3 to be $\frac{\Delta I}{I} = 75\%$. This means that 75% of the loss of the aptamer spots is accounted to the association reaction with OTA.

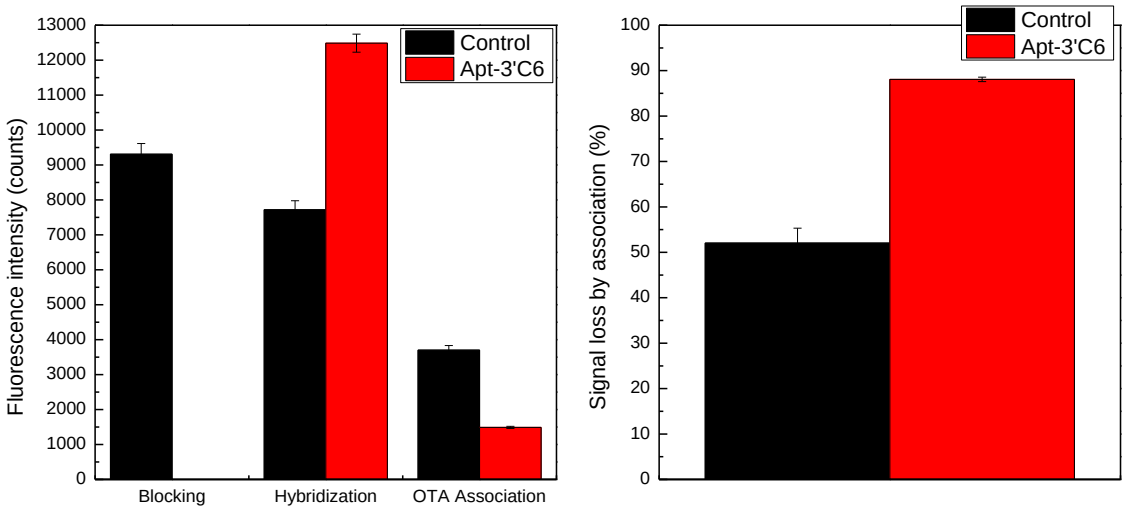


Figure 48: Left: histogram of fluorescence intensity (0.5 s scan time) during all steps of the experiment of control and Apt-3'C6 spots in Figure 47. Right: histogram of signal loss of spots after association.

Signal ON:

The "signal ON" experiment is conducted with the spotting of a control oligonucleotide and the Cy5-labelled aptamer Apt-3'C6-5'Cy5 at 10 µM. The hybridization is carried out with the complementary strand cApt13-3'BHQ with a concentration of 1 µM at 45°C. The association with OTA is conducted with 10 µM OTA in BB-Aguado.

The fluorescence images (0.5 s scan time) after all steps (blocking, hybridization and association with OTA) are displayed in Figure 49. After blocking, the control and the aptamer spots are clearly visible, as expected. The images after hybridization display a slightly decreased signal for the control spots. The hybridization of the quencher-labelled complementary strands results in a strongly reduced intensity for the

aptamers, indicating successful hybridization and quenching of the fluorophore on the aptamer. After association with OTA the control spots display a strong decrease while the aptamers only show a slight one.

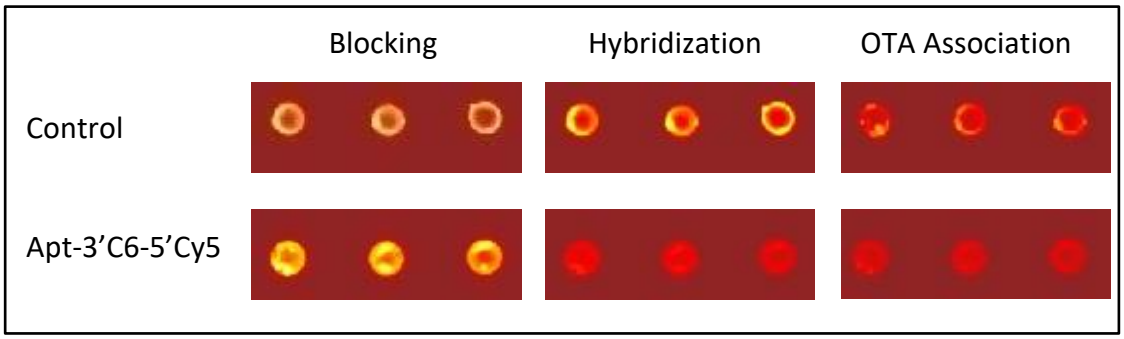


Figure 49: Fluorescence images (0.5 s scan time) of the spotted control oligonucleotides and Apt-3'C6-5'-Cy5 aptamer.

For the system "signal ON", a signal gain is expected instead of a signal loss as for the system off. Therefore the **relative gain** for "signal ON", which takes into account the loss of the control spots, is calculated with:

$$\frac{\Delta I_{gain}}{I} = \frac{I'_{apta} - \eta_{cont} I_{apta}}{\eta_{cont} I_{apta}} = \frac{I'_{apta}}{\eta_{cont} I_{apta}} - 1$$

Figure 50 shows the histogram of the fluorescence intensities of the spots on the left and the relative signal loss on the right. After blocking, the control and aptamer spots exhibit very similar fluorescence intensity. The intensity of the control spots decreased slightly after hybridization ($\mu_{cont} = 22\%$), but strongly after the association ($\mu_{cont} = 50\%$). The aptamer on the other hand exhibits a strong signal decrease ($\mu_{apta} = 77\%$) by the hybridization with the quencher-labelled complementary strands. The following association with OTA causes a further decrease of intensity of $\mu_{apta} = 18\%$ for the aptamer spots. The lower loss of the Apt-3'C6-5'Cy5 spots indicates removal of complementary strands by the association.

Calculating the relative gain of the aptamer spots with eq. 4 yields $\frac{\Delta I_{gain}}{I} = 64\%$. So despite the fact that the spots lost in absolute intensity they display a relative gain, when taking into account the loss of the control spots. The relative gain verifies the dissociation of the complementary strands during the association reaction with OTA.

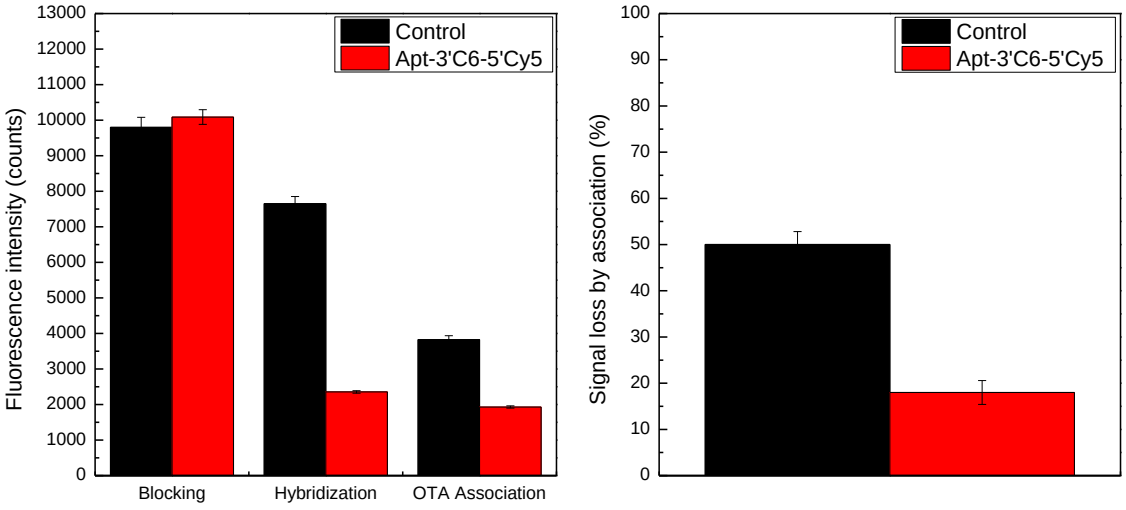


Figure 50: Left: histogram of fluorescence intensity (0.5 s scan time) during all steps of the experiment of control and Apt-3'C6-5'Cy5 spots displayed in Figure 49. Right: histogram of signal loss of spots after association.

5.3.2.2 Increased stringency during association reaction

The first experiments showed promising results, therefore the stringency of the experiments was increased. In order to avoid false positive results the association was carried out with the buffer solution containing OTA, as well as containing no OTA. For this two different buffer solutions were compared, BB-Aguado (10 mM TRIS, 120 mM NaCl, 20 mM $CaCl_2$, and 5 mM KCl; pH 8.5), and SB-Aguado (10 mM HEPES, 120 mM NaCl, 5 mM KCl, 20 mM $CaCl_2$; pH 7).

For these experiments a "control" oligonucleotide and the aptamer Apt-3'C6 were spotted at 10 µM. The hybridization was carried out with 1 µM of the 13mer complementary strand cApt13-5'Cy5 at 45°C. The association was conducted with (A) 10 µM OTA in BB-Aguado pH 8.5, and BB-Aguado pH 8.5 without OTA on separate

zones, and (B) 10 µM OTA in SB-Aguado pH 7, and SB-Aguado pH 7 without OTA on separate zones.

(A) Association in BB-Aguado

The comparison of the association with and without OTA in the buffer BB-Aguado is carried out on one slide, but on separate *zones*. The steps of blocking and hybridization are conducted identically for both zones. Figure 51 shows the fluorescence images (0.5 s scan time) after all steps (blocking, hybridization and association). Top shows images where the association was carried out in BB-Aguado without any OTA (blank). The bottom images display the association with 10 µM OTA in BB-Aguado. After blocking the control spots are visible, while the aptamer spots show as expected no fluorescence signal. The success of the hybridization with the complementary strands can be seen as the spots of the aptamer show a strong fluorescence response. The control spots have lost a lot in intensity during the hybridization process. The images after association (with and without OTA) show a strong decrease of fluorescence signal for both the control and the aptamer spots.

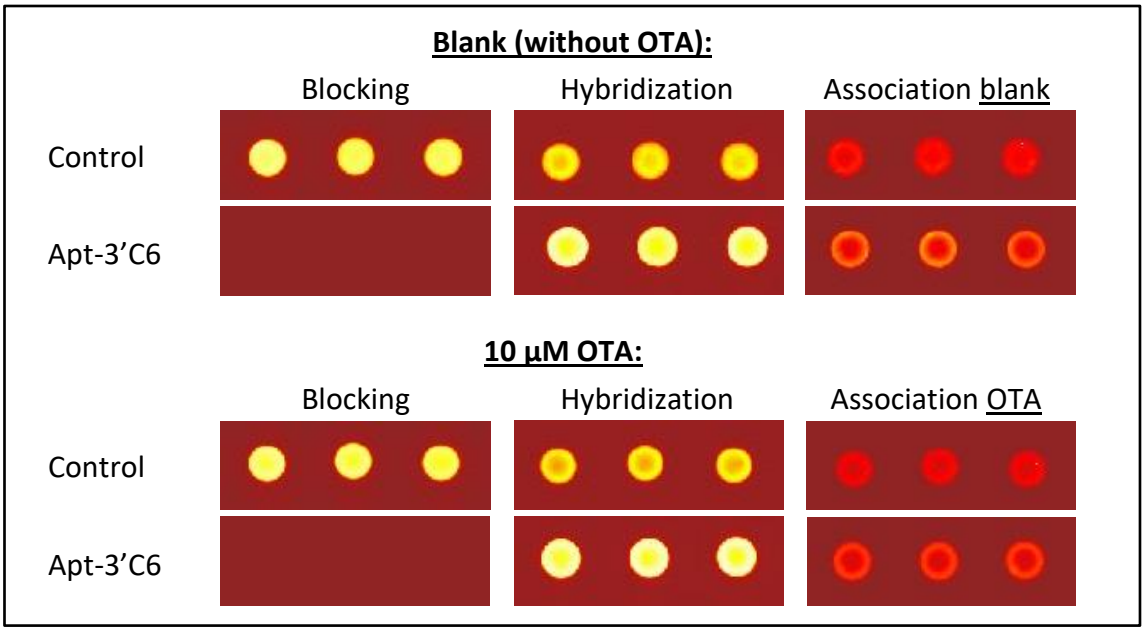


Figure 51: Fluorescence images (0.5 s scan time) of the spotted control oligonucleotides and Apt-3'C6 aptamer. Association on top was carried out in BB-Aguado, pH 8.5 without OTA, on the bottom with 10 µM OTA in BB-Aguado, pH 8.5.

The histogram of the fluorescence intensities of the spots are displayed in Figure 52. On the left side the association was carried out blank (BB-Aguado without OTA), and on the right side the association was conducted with 10 µM OTA. The corresponding signal losses (calculated with eq. 1) of the control and aptamer spots after association are displayed on the left in Figure 53. For both zones (with and without OTA) the intensity of the control spots drops noticeably after hybridization ($\mu_{cont} = 40 - 45\%$), but even more after the association ($\mu_{cont} = 74 - 80\%$). The two zones exhibit very similar fluorescence intensities for the control spots during all steps, indicating good comparability between the zones. The Apt-3'C6 aptamer shows zero intensity after the blocking, and shows a strong signal after being hybridized with its Cy5-labelled complementary strands. Both zones show similar fluorescence intensities for the control and aptamer spots. The association without OTA strongly decreases the fluorescence intensity by $\mu_{apta} = 80\%$, while the association with OTA also exhibits a strong loss of $\mu_{cont} = 85\%$. The relative loss of the aptamer spots, which takes into account the loss of the control spots is calculated with eq. 3; and is displayed on the right in Figure 53. The relative loss without OTA is $\frac{\Delta I}{I} = 21\%$, while it is at $\frac{\Delta I}{I} = 26\%$ with OTA. This difference is not large enough to be statistically significant, and the signal decrease of the aptamers is therefore mainly caused by the association buffer and not OTA.

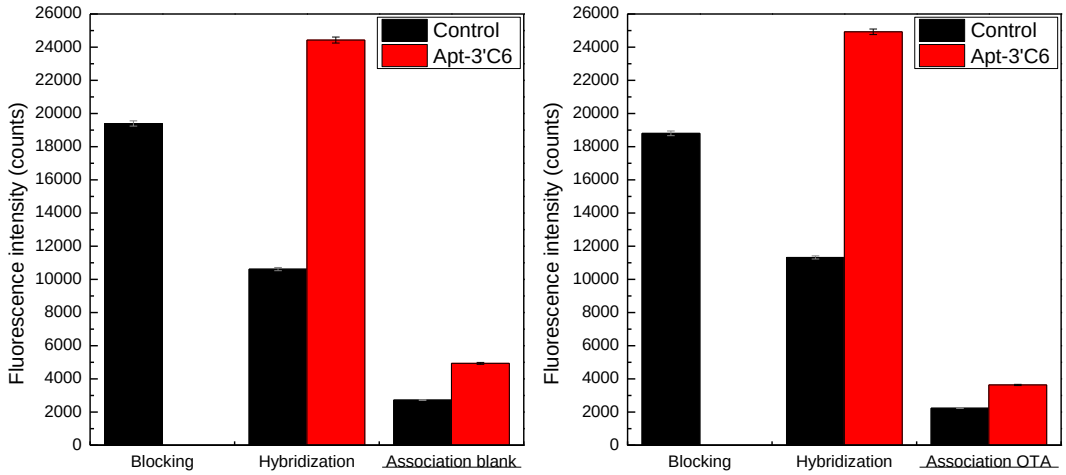


Figure 52: Histogram of fluorescence intensity (0.5 s scan time) during all steps of the experiment of control and Apt-3'C6 spots in Figure 51. Left: "blank" association in BB-Aguado without OTA. Right: association with 10 µM OTA in BB-Aguado.

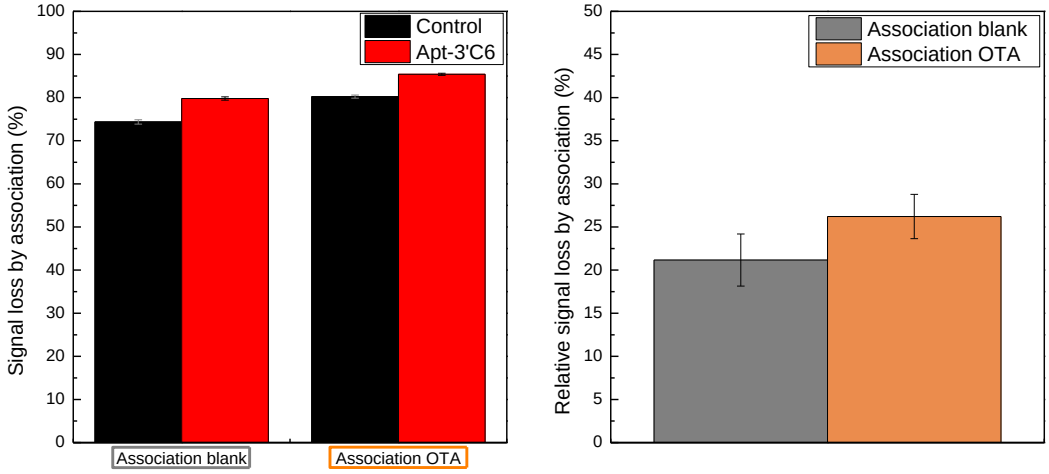


Figure 53: Left: histogram of signal loss of spots after blank and OTA association (with eq. 1). Right: histogram of relative signal loss of aptamers which takes into account the loss of the control spots (with eq. 3).

(B) Association in SB-Aguado

The association was conducted with another buffer in order to test the influence of the buffer on the association. The buffer used is SB-Aguado, the selection buffer used during the SELEX process of the aptamer.[128] The experiment was carried out on one slide, with two separate zones for the association with and without OTA. The blocking and hybridization are carried out identically on both zones. The fluorescence images (0.5 s scan time) after all steps (blocking, hybridization and association) are displayed in Figure 54. Images on the top show the association carried out in SB-Aguado, pH 7 without any OTA (blank). Images on the bottom display the association with 10 µM OTA in SB-Aguado, pH 7. The images after blocking show clearly the control spots, while the aptamer spots show no fluorescence signal. Hybridization with the complementary strands shows intense fluorescence for the aptamer spots, while the intensity of the control spots decreases visibly from the previous step. After association (with and without OTA) a strong decrease of the fluorescence signal can be seen for both the control and the aptamer spots.

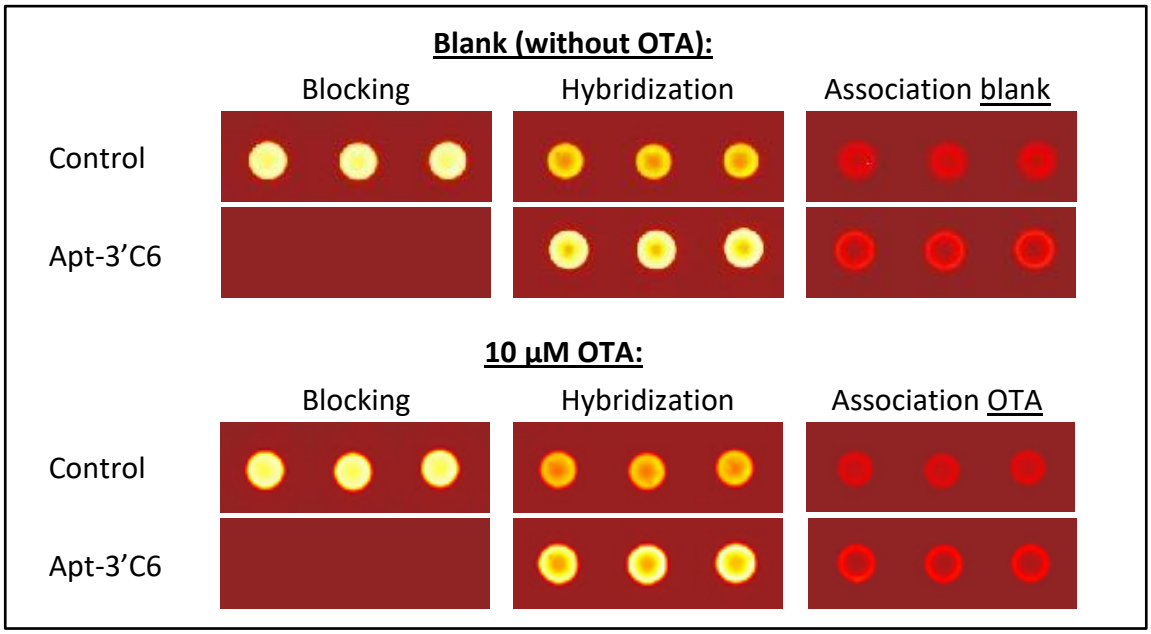


Figure 54: Fluorescence images (0.5 s scan time) of the spotted control oligonucleotides and Apt-3'C6 aptamer during all steps of the experiment. Association on top was carried out in SB-Aguado, pH 7 without OTA, on the bottom with 10 µM OTA in SB-Aguado, pH 7.

The histogram of the fluorescence intensities of the spots is displayed in Figure 55. The left side shows the association carried out blank (SB-Aguado, pH 7 without OTA), and the right side the association conducted with 10 µM OTA in SB-Aguado, pH 7. The control and aptamer spot signal losses after association are displayed on the left in Figure 56. The control spots of both zones exhibit a strong intensity decrease after hybridization ($\mu_{cont} = 56 - 58\%$), but even more after the association ($\mu_{cont} = 82 - 83\%$). Both zones show the same behavior. The Apt-3'C6 aptamer emits no fluorescent signal after blocking, but exhibits a strong signal once hybridized with its fluorescent complementary strands. The association causes an $\mu_{apta} = 88\%$ decrease of fluorescence for both zones (with and without OTA). Taking into account the loss of the control spots yields the relative loss (eq. 3) of the aptamer spots, as displayed on the right in Figure 56. The relative loss on the zone where the association was carried out without OTA is $\frac{\Delta I}{I} = 34\%$, while it is $\frac{\Delta I}{I} = 31\%$ for the zone with OTA. Once again the signal decrease of the aptamers is not only caused by the OTA, but mainly by the

association buffer. This does not necessarily imply that OTA is not bound to the aptamers, it only indicates that the interaction was not detected.

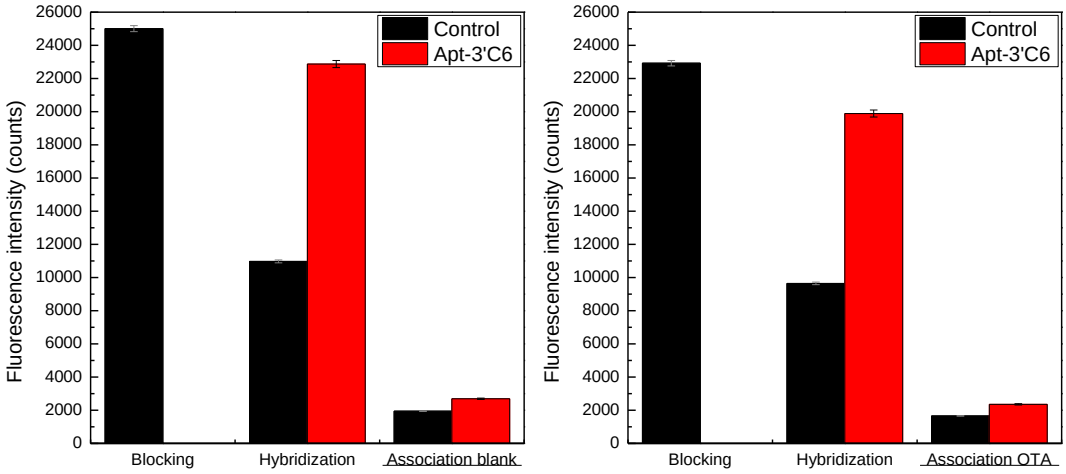


Figure 55: Histogram of fluorescence intensity (0.5 s scan time) during all steps of the experiment of control and Apt-3'C6 spots in Figure 54. Left: "blank" association in SB-Aguado without OTA. Right: association with 10 µM OTA in SB-Aguado.

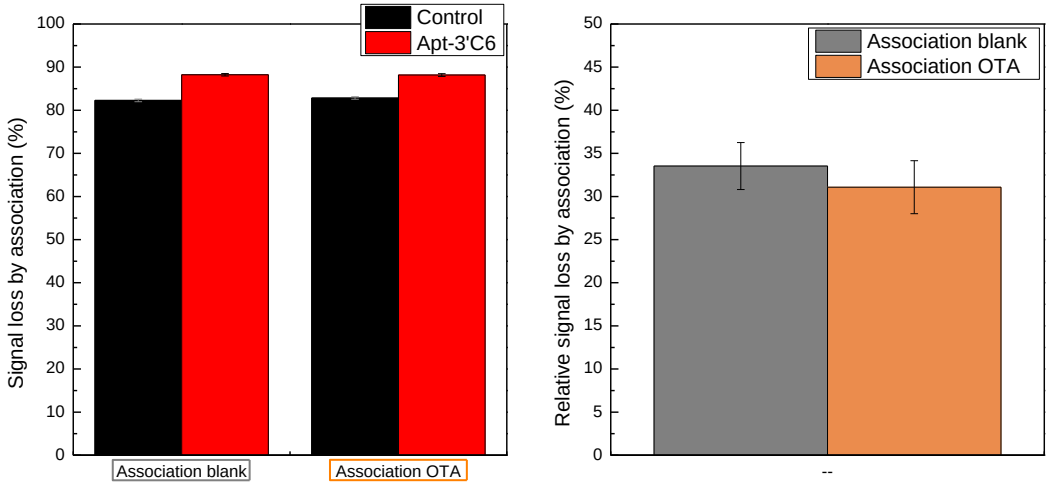


Figure 56: Left: histogram of signal loss of spots after blank and OTA association (with eq. 1). Right: histogram of relative signal loss of aptamers which takes into account the loss of the control spots (with eq. 3).

The high loss of fluorescence intensity during the experiment is a recurrent problem when working with fluorophores. By already comparing the losses of the control spots of only the previous experiments ($\mu_{cont} \approx 20\%$ after hybridization, $\mu_{cont} \approx 50\%$ after association) with the losses of the present one ($\mu_{cont} \approx 50\%$ after hybridization, $\mu_{cont} \approx 80\%$ after association), it becomes visible that the losses change strongly between experiments, despite the experiments having been carried out exactly the same way. High intensity loss is problematic for the analysis of the results, as especially towards the end of the experiment the intensities of the control spots are very low. The two buffers which were used (BB-Aguado and SB-Aguado) differ mainly in their pH (8.5 and 7, respectively) and the buffering agent (TRIS and HEPES, respectively). Since they show very similar behavior the different pH and the buffering agents can be excluded as a reason for the fluorescence intensity loss (bleaching). There are two potential reasons for this bleaching; either it is caused by the instability of the used dye (Cy5)[245] or the oligonucleotides are not well immobilized on the surfaces.

5.3.2.3 Stability of oligonucleotide immobilization

The stability of the immobilization is studied with spotted aptamers (Apt-3'C6). The aptamers are hybridized with their complementary strand (cApt13-5'Cy5), associated with OTA, regenerated and then again re-hybridized. The regeneration of the aptamers is carried out in the same regeneration buffer which was used in chapter 4 for the regeneration of OTA from aptamers immobilized on crystalline silicon surfaces (1 ml of methanol/(10 mM TRIS, 1 mM EDTA, pH 9) (20:80, v/v).

The fluorescence images (0.5 s scan time) of the control and aptamer spots are displayed in Figure 57 and the fluorescence intensity is shown in Figure 58. Even though the first steps of the experiment (blocking, hybridization, association) were carried out exactly as for the previous experiments, the control spots remain very stable. The loss after the first hybridization is $\mu_{cont} = 2\%$ and after the association it is $\mu_{cont} = 6\%$. After the regeneration the control spots display a higher loss ($\mu_{cont} = 30\%$), while it decreases again for the second hybridization ($\mu_{cont} = 12\%$). This

amounts to a total loss of $\mu_{cont} = 38\%$ (or 62% remaining signal) between the first and the second hybridization.

The aptamer spots display no signal after the blocking, as expected. After the 1st hybridization with the complementary strand an intense fluorescence signal is visible. An association with 1 mM OTA in BB-Aguado, pH 8.5 causes a signal decrease of $\mu_{apta} = 15\%$. The following regeneration results in a fluorescence intensity which is decreased by $\mu_{apta} = 86\%$ in comparison to the 1st hybridization. The 2nd hybridization then causes a strong increase, reaching 81% of the intensity of the 1st hybridization, or 96% of the association.

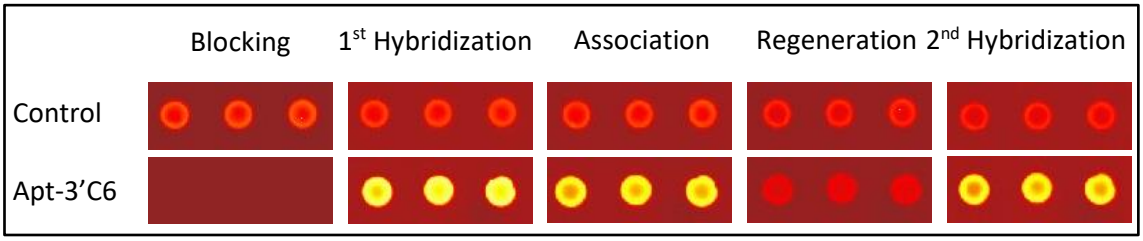


Figure 57: Fluorescence images (0.5 s scan time) of the control and Apt-3'C6 aptamer spots.

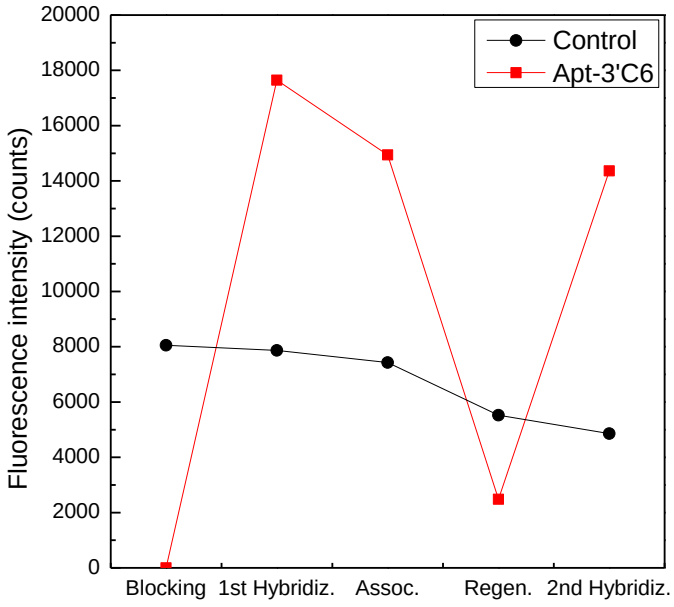


Figure 58: Fluorescence intensity (0.5 s scan time) during all steps of the experiment of control (black) and Apt-3'C6 (red) spots in Figure 57.

The control spots remained surprisingly stable during this experiment, unlike in the previous ones conducted. A clear explanation for this is difficult to find, as it was conducted in the same way and with the same products. For the aptamer spots it can be assumed that after the regeneration some of the OTA remains bound to the aptamers (see chapter 4), and since there is also some remaining signal not all complementary strands are detached. After the second hybridization the signal is at 81% of the intensity of the first hybridization. There are two factors which have to be taken into account. Firstly not all aptamers are available for re-hybridization, as some are still binding OTA, and secondly some aptamers remain hybridized even during the regeneration. The portion of complementary strands which remained hybridized is naturally also subject to bleaching, which also decreases the maximum achievable final intensity after the 2nd hybridization. This indicates that the oligonucleotide immobilization is reliable, and that the strong signal loss of the control spots during the experiments is therefore probably from bleaching of Cy5 and not due to probe-detachment. Nevertheless, an answer for the false positive results of the aptamers has still not been found.

5.3.2.4 Aptamer immobilization direction and complementary strand length

The probe immobilization seems to be sufficiently stable and not to be the source of the false-positive results. Since the “de-hybridization rate” (signal loss) of the duplex aptamer-complementary strand remains the same when conducted with and without OTA, its insufficient stability might be the cause of these problems. This instability might be influenced by the association buffer, but the results in chapter 5.3.2.2 indicate that this is probably not the case. Therefore in order to study the stability of the duplex different lengths of complementary strands were compared, as longer complementary strands suppose a higher stability. Another question which arises is if there is a difference visible when the aptamers are immobilized by their 5’ or 3’ side. Both systems can be found in publications,[229,238] but the binding of OTA probably takes more place towards the 3’ end.[246] Also, as already stated, the distance of the fluorophore from the surface plays an important role in the fluorescence enhancement on this a-$Si_{1-x}C_x$:H architecture.

The comparison of different aptamers and complementary strands is carried out with the two aptamers Apt-3'C6 and Apt-5'C12. The second aptamer also has a longer spacer, which might improve potential problems with steric hindrance. Both aptamers were hybridized with the three complementary strands cApt18-3'Cy5, cApt18-5-'Cy5, cApt36-5'Cy5, as depicted in Figure 59. The association with OTA is carried out with 1 mM OTA in BB-Aguado, pH 8.5, and the association without OTA (blank) is carried out with only BB-Aguado, pH 8.5.

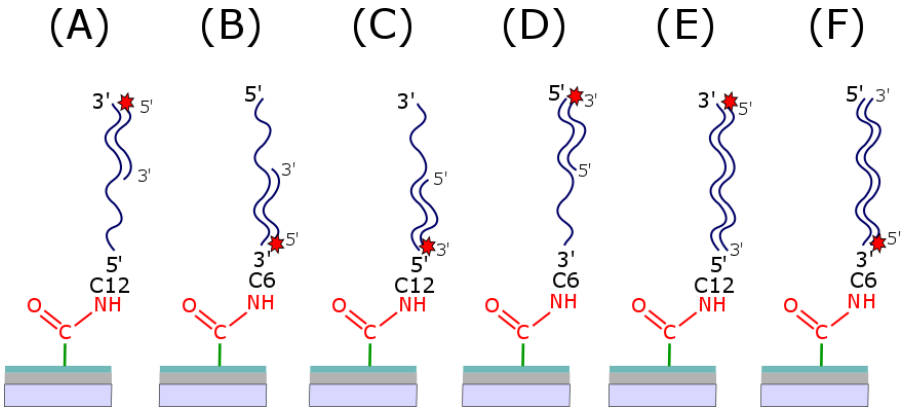


Figure 59: Scheme of all combinations of aptamers with complementary strands.

The fluorescence images (0.5 s scan time) of the control and aptamer spots after hybridization (1 µM) and association with (1 mM) or without OTA are displayed in Figure 60. The images after blocking are not displayed as they are not of interest for the analysis of the association. The fluorescence intensities after hybridization are displayed in Table 16. The influence on the distance from the surface can be best seen with the combination (E) and (F), but is also visible for (A) and (B) or for (C) and (D). The fluorophore being far away from the surface results in a higher fluorescence output. In the case of (F) the hybridization might also be hindered by the Cy5 which might be impeding the hybridization or another unclear problem, since the fluorescence intensity difference is significantly lower for the other combinations. A disturbance of the hybridization by the fluorophore being near the surface does not seem very probable, as this effect was not observed as strong for the couples (A) and (B), or the couples (C) and (D). The difference for the hybridization between immobilizing the aptamer on 3' and 5' cannot be clearly deduced, since the distance of the fluorophore from the surface is crucial for the fluorescence output.

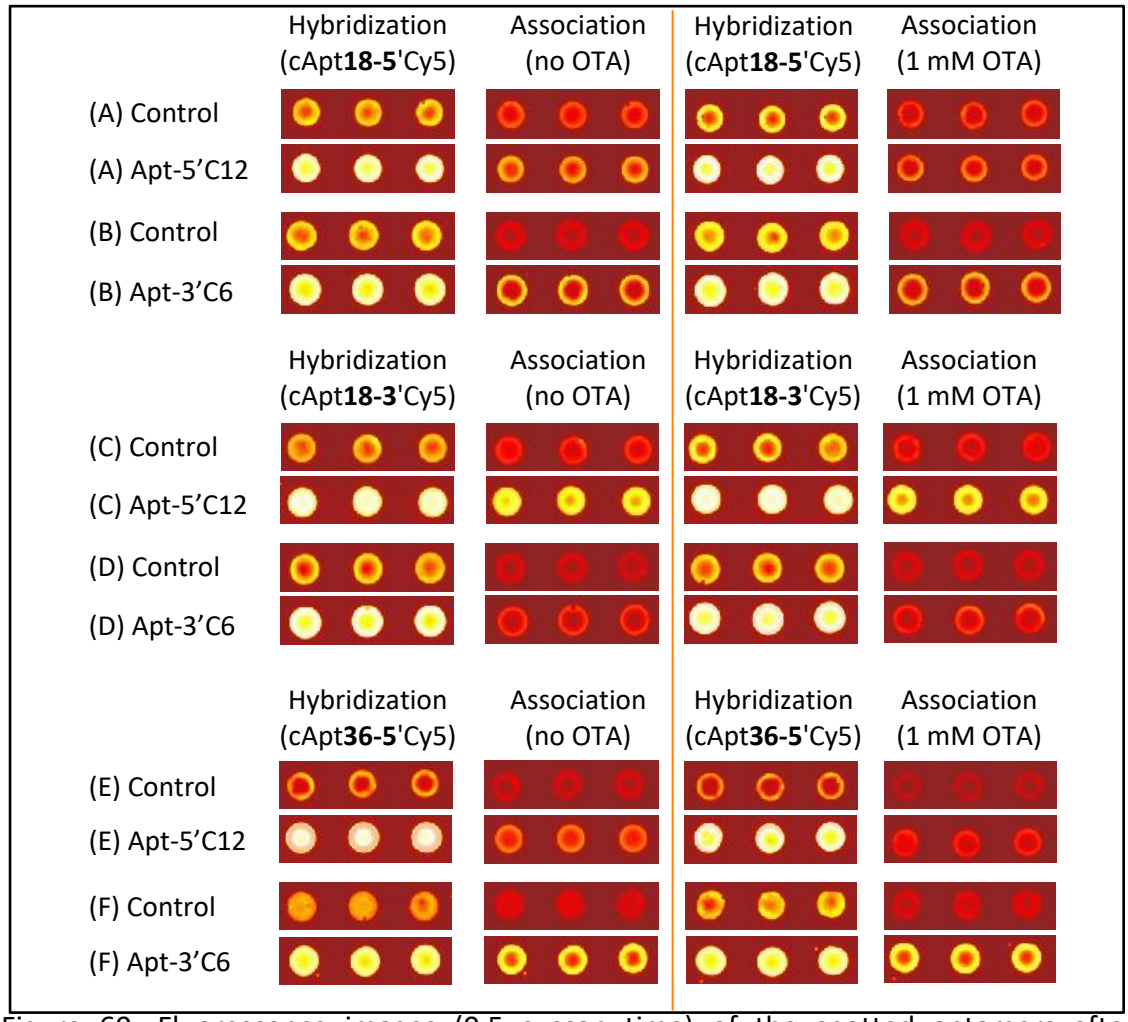


Figure 60: Fluorescence images (0.5 s scan time) of the spotted aptamers after hybridization with different complementary strands, and after association with and without OTA in BB-Aguado, pH 8.5.

Table 16: Fluorescence intensities of aptamer spots after hybridization as displayed in Figure 60.

→ Aptamer	**Apt-5'C12**	**Apt-3'C6**
↓Complemen. oligo.	**Intensity (counts)**	**Intensity (counts)**
cApt**18-3'Cy5**	(C) 28000-30000	(D) 29000-33000
cApt**18-5'Cy5**	(A) 26000-30000	(B) 25000-26000
cApt**36-5'Cy5**	(E) 38000-45000	(F) 23000-24000

All spots on the fluorescence images exhibit a relatively strong signal decrease after association. The signal losses where again calculated with eq. 1 and are displayed in Table 17. The orange cells indicate where the association with OTA was slightly more efficient then the association without OTA, with losses being around 5% higher after association with OTA. The only couple aptamer / complementary strand which worked very well is marked in green. The association without OTA shows a signal decrease of $\mu_{apta} = 69.7\%$, while with OTA an $\mu_{apta} = 82.2\%$ decrease was determined. The relative signal loss, which takes into account the loss of control spot intensity, gives a loss of $\frac{\Delta I}{I} = 40.9\%$ for the association with and $\frac{\Delta I}{I} = 23.9\%$ without OTA, indicating a successful association by OTA for the aptamer Apt-5'C12 hybridized with the complementary strand cApt18-5'Cy5.

Table 17: Signal loss of the different aptamer/complementary strand spots as displayed in Figure 60. The values are calculated with eq. 1.

→ Aptamer	**Apt-5'C12**		**Apt-3'C6**	
↓Complemen. oligo.	**1mM OTA**	**No OTA**	**1mM OTA**	**No OTA**
cApt**18-3'Cy5**	50.4 %	45.3 %	87.7 %	88.0 %
cApt**18-5'Cy5**	82.2 %	69.7 %	73.8 %	67.2 %
cApt**36-5'Cy5**	90.5 %	86.8 %	59.5 %	59.7 %

The association seems to work better on the aptamer which is immobilized on its 5' side, especially when hybridization was conducted with the cApt18-5'Cy5 complementary strand. The problem of equal de-hybridization with and without OTA was again observed, even for the 36mer complementary strand, which is quite surprising, as it should show the highest affinity towards the aptamer. Nevertheless a clear answer for the cause of the false-positive results could not yet be found.

5.3.2.5 Perspectives

In order to find the reason for the false positive results, experiments are ongoing. They include the comparison of the effects of different buffer solutions on the de-hybridization and bleaching of complementary strands with different lengths during the association process.

For further studies concerning OTA there are also some other aspects which would prove of interest. First of all the association reaction could be further improved, as an optimization of the association buffer for OTA could strongly increase the reaction yield. Also the stability of the fluorophore-system should be improved, as high fluorescence signal losses were regularly observed during the experiments. This can be achieved for example by changing to another fluorophore, or by adding Cy5-protectants during the experiment (e.g. Dyesaver from Genisphere or “Stabilization and Drying Solution” from Agilent). It would also be of high interest to study the limit of detection (LOD) and the dissociation constant (Kd) by using a microfluidic in-situ system.

5.4 Conclusion

The biochips for the detection of OTA with aptamers by fluorescence were presented in this chapter. Their architecture is based on an 44 nm a-$Si_{1-X}C_X$:H film deposited on an aluminium back-reflector. In a first step the PECVD-deposition of a-$Si_{1-X}C_X$:H was calibrated to ensure good fluorescence enhancement. The deposition rate for a-$Si_{0.85}C_{0.15}$:H was found to be 1.10 µm/h.

Two methods of fluorescence detection (signal OFF and signal ON) were studied with 13mer complementary strands. The assays displayed promising results, with 75% and 64% relative signal change by the association for “signal OFF”and “signal ON”, respectively. Nevertheless, increased stringency lead to false positive results, where no difference was found between a blank association and an association with OTA. The strong fluorescence intensity decrease of control spots lead to the study of the quality of the oligonucleotide-immobilization, which were found to be stable and well-controlled. Finally two different aptamer immobilization directions (Apt-3’C6 and Apt-5’C12) were compared with three different complementary strands. The three complementary strands were two 18mer, one from each end (cApt18-3'Cy5, cApt18-5-'Cy5), and one 36mer cApt36-5'Cy5. The combination which yielded the best result was the aptamer Apt-5’C12 with the complementary strand cApt18-5-'Cy5, which showed a 40.9% relative signal loss with OTA and 23.9% without OTA.

6 General Conclusion and Outlook

The goal of this thesis was to develop a stable and reproducible biochip architecture, based on an amorphous silicon carbon alloy for a reliable and sensitive detection of the interaction of pathogens with aptamers, notably the interaction of the toxin ochratoxin A with its DNA-aptamer as a model system.

The goal of this thesis was to study the interaction of pathogens with aptamers on a stable and reproducible biochip architecture based on an amorphous silicon carbon alloy (a-$Si_{1-X}C_X$:H) deposited on an aluminium back-reflector for reliable and sensitive detection of pathogens.

The selected strategy for biomolecule immobilization consists of the grafting of acid-terminated monolayers on hydrogenated silicon surfaces with stable Si-C bonds. These acid surfaces are the basis for the immobilization in soft conditions (with EDC and NHS) of NH_2-terminated functional groups by reliable amide bonds. Quantitative analysis by ATR-FTIR enables detailed study of quality and density of the grafted surfaces. The immobilization of NH_2-terminated PEG was carried out as an example, and the antifouling properties of the resulting PEG-layers towards bacteria showed promising results.

The relation of OTA-structure with its infrared and UV-vis response in different media was studied and put in relation with preliminary DFT calculation results, which were obtained in collaboration with the laboratory LCM at Ecole Polytechnique. It was found that in water the open-ring and double-deprotonated forms coexist at pH 8.5 and pH 11. In-situ IR and UV-vis calibration measurements were conducted to be able to quantify OTA on surfaces after interacting with grafted aptamers.

Quantitative studies of the grafting of aptamers on acid-terminated crystalline silicon surfaces were performed by ATR-FTIR. Thereby the amidation yield was optimized by tuning the buffer solution and the 2-step amidation process, resulting in high-density aptamer surfaces. The interaction of OTA with its aptamer on surfaces was successfully shown and quantified by ATR-FTIR, yielding an OTA surface density of $N_{OTA} = 1.9 \cdot 10^{13}\ cm^{-2}$ on the aptamers. The regeneration of OTA from its aptamers with a regeneration buffer was also demonstrated by IR and UV-vis, and the specificity and selectivity of the aptamer towards OTA was validated by using a chemically similar molecule (warfarin), towards which the aptamer displayed no affinity.

The biochips for the detection of OTA with aptamers by fluorescence were presented. Their architecture is based on an a-$Si_{1-X}C_X$:H film, with an optimized thickness and carbon content for increased fluorescence, deposited on an aluminium back-reflector. The quality of the oligonucleotide-immobilization on the a-$Si_{1-X}C_X$:H surfaces was studied and were found to be stable and well-controlled. Two methods of fluorescence detection (signal OFF and signal ON) were studied by using Cy5-labelled 13mer complementary strands. The assays displayed promising results, with 64%-75% relative signal change by the association with OTA at 10 µM. However, increased stringency lead to false positive results when the aptamer was hybridized with the 13mer complementary strand. Suspecting an insufficient stability of the duplex (aptamer-complementary strand) causing the false positive results, different immobilization direction of the aptamer (on 3' or 5') was compared with different lengths of complementary strands (18mer and 36mer). The combination which yielded the best result was the aptamer Apt-5'C12 with the complementary strand cApt18-5-'Cy5, which showed a 17% difference of signal loss between association with OTA and without OTA.

The study of the model system with OTA and its aptamer still offers plenty of interesting aspects to explore, such as an improved stability of the aptamer/complementary strand duplex, an improved association in different media, and retrieving the limit of detection (LOD) of the detection by fluorescence.

A new challenge could be found in the direct detection of pathogens by surface-enhanced Raman spectroscopy (SERS). The direct detection method can help to avoid the problems encountered with indirect detection by fluorescence (bleaching of fluorophores, false positive results). An enhanced Raman response can be achieved by adapting an architecture of noble metal nanostructures covered by an a-$Si_{1-X}C_X$:H thin film, which has already been developed for LSPR-enhancement of fluorescence in PMC.[21,23] Applying first the model system of OTA with its aptamer for direct detection by SERS offers the possibility of using a known system for a new method of detection. Once the direct detection of OTA by SERS is well in place the system can be adapted for other pathogens, notably bacteriological pathogens.

LIST OF ABBREVIATIONS AND ACRONYMS

OTA … Ochratoxin A

Cy5 … Cyanine 5, commonly used fluorophore

Aptamer … single stand of DNA, selected to bind a specific target

mer … repeating unit in a polymer, in this case the number of bases of an aptamer

a-$Si_{1-X}C_X$:H … amorphous silicon-carbon

NP … nanoparticle

MB … magnetic bead

PECVD … plasma enhanced chemical vapor deposition

SEM … scanning electron microscopy

ATR-FTIR … attenuated total reflection – Fourier transform infrared spectroscopy

LSPR … localized surface plasmon resonance

SERS … surface-enhanced Raman spectroscopy

ANNEX

A.I. ATR-FTIR SPECTROSCOPY

I.1 Principle of FTIR spectroscopy in ATR geometry

Infrared spectroscopy is based on the absorption of infrared light by an analyzed material. It is used to identify substances, elucidate chemical structures or quantify known materials.

The basic principle relies on the excitation of vibrational and rotational modes of molecules by the irradiation with (and thus absorption of) polychromatic electromagnetic waves in the mid-infrared wavelength region (wavenumber 4000 - 400 cm^{-1}, or wavelength 25 – 2.5 µm). The absorption of the infrared light is visible in the measured spectrum. This allows the identification and quantification of materials, since the frequencies and energies are characteristic for the respective chemical bonds.

There are different methods of IR-spectroscopy, such as transmission and diffuse reflectance infrared Fourier transform spectroscopy. The measuring technique used in the laboratory PMC is referred to as ATR–FTIR spectroscopy (attenuated total reflection - Fourier transform infrared), which enables the direct examination of samples in solid or liquid phase. The core principle is total internal reflection of the infrared light in the ATR crystal (Figure 61). The infrared beam is passed through a crystal and reflects off the internal surface. Total internal reflection takes place at the interface of two non-absorbing media of two different refraction indices. When the propagating wave strikes the interface, where the refractive index is lower on the other side and at an angle larger than the critical angle the wave is entirely reflected. The critical angle depends on the refractive indices of the two media.

Generally this will result in partial reflection and refraction of the wave, depending on the incident angle. When the beams' incident angle is larger than a particular critical angle θ_C it is fully reflected internally (see eq. 5, with n_1 and n_2 the refractive index of the crystal and the medium on the other side of the interface, respectively).

$$\theta_C = sin^{-1}\left(\frac{n_2}{n_1}\right) \quad (5)$$

Total reflection creates an evanescent wave which extends 0.5 - 5 µm beyond the internal surface and decays exponentially with increasing distance from the interface. The penetration depth δ_P of the evanescent wave depends on the wavelength as shown in eq. 6 (with wavelength λ, incident angle φ).[170]

$$\delta_P = \frac{\lambda}{2\pi\sqrt{{n_1}^2 sin^2\varphi - n_2^2}} \quad (6)$$

A sample brought close to the evanescent wave (and thereby the crystal surface) can then interact with it.

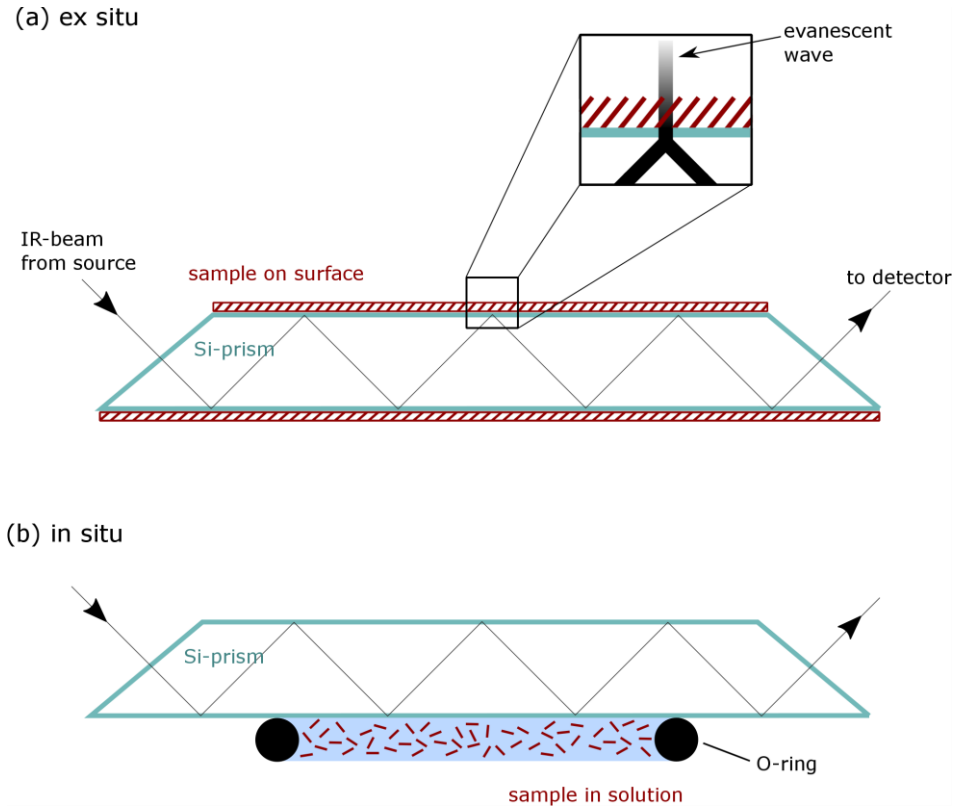


Figure 61: Scheme of silicon sample for spectroscopic studies by ATR-IR for *ex situ* (a) and *in situ* (b) measurements.

The measurements were carried out on a Bomem MB 100, with a Michelson interferometer for fast data acquisition by Fourier transform. The detector is a liquid nitrogen cooled mercury cadmium telluride detector (MCT). The substrates used are

double-polished FZ n-Si(111) wafers. They are polished to obtain 45° bevels, resulting in around 30 internal reflections. In order to minimize the influence of water vapor and carbon dioxide, the sample chamber was purged for 40 minutes with nitrogen gas, before the spectra (100 scans) were recorded with a resolution of 4 cm^{-1}. The spectra were recorded in p- and s-polarization for *ex situ* measurements and in s-polarization for *in situ* measurements. The *in situ* measurements were conducted with an *in situ* liquid cell, which allows adding and removing solutions, without changing the setup. The O-rings were made of Kalrez (perfluorelastomer) with a 10 mm diameter, resulting in 10 internal reflections.

I.2 Quantitative analysis

I.2.1 Theoretical background

The method of extracting the density of molecules on a surface from their IR-absorbance was developed in the laboratory PMC.[16,170,247] The absorbance of a material is related to its concentration, analogous to the Beer-Lambert law in transmission spectroscopy. Carrying out in situ measurements in liquid phase at known concentrations enables the calibration of the absorbance to the number of molecules detected.

The expressions describing the absorbance of a layer with thickness δ and a dielectric function $\epsilon = \epsilon' + i \cdot \epsilon''$ can be linearized, assuming that the layer thickness is much smaller than other characteristic lengths of reflectivity. Following Chabal the absorption of a layer in s- and p-polarization can then be given by:[170]

$$A_S = \frac{2\pi}{\lambda} \frac{1}{n_S \, cos\varphi} I_y \epsilon_y'' d \tag{7}$$

$$A_P = \frac{2\pi}{\lambda} \frac{1}{n_S \, cos\varphi} \left(I_x \epsilon_x'' \delta + I_z \frac{n_2^4}{\epsilon_z'^2 + \epsilon_z''^2} \epsilon_z'' d \right) \tag{8}$$

Where n_S and n_2 are the refractive indices of silicon and the adjacent medium, respectively. d is the layer thickness, λ is the wavelength and φ the incident angle.

I_x, I_y, I_z are dimensionless coefficients which characterise the intensity of the electric field on the surface in the three dimensions x, y and z. They are given by:

$$I_x = \frac{4\, n_S^2\, cos^2\varphi\, (n_S^2\, sin^2\varphi - n_2^2)}{n_2^4\, cos^2\varphi + n_S^4\, sin^2\varphi - n_S^2\, n_2^2} \tag{9}$$

$$I_y = \frac{4\, n_S^2\, cos^2\varphi}{n_S^2 - n_2^2} \tag{10}$$

$$I_x = \frac{4\, n_S^4\, cos^2\varphi\ sin^2\varphi}{n_2^4\, cos^2\varphi + n_S^4\, sin^2\varphi - n_S^2 n_2^2} \tag{11}$$

In case of s-polarization only I_y plays a role. In p-polarization the two other coefficients I_x and I_z partake.

The calibration experiments are carried out on silicon, while the molecules are suspended in liquid. This means, that the coefficients of the electric field I_x^0, I_y^0, I_z^0 are different from the coefficients I_x, I_y, I_z which were describing the interface silicon/vacuum before. In this experimental setup there is no interfacial layer, but the adjacent medium absorbs and its refractive index is complex ($\tilde{n}_2 = n_2 + ik_2$).

The calibration measurement allows determining the absorption of the liquid, which is defined by the loss of intensity reflected in relation to the total reflection (without absorption). If the absorption is weak enough ($k_2 < 0.1$), then the attenuation by the decreasing electromagnetic field from the interface can be ignored. In this case the penetration depth can be calculated as described in eq. (6).

This leads to the absorption per reflection in liquid:

$$A_S^0 = \frac{2\pi}{\lambda} \frac{1}{n_S\, cos\varphi} I_y^0 2 n_2 k_2 \frac{\delta}{2} \tag{12}$$

$$A_P^0 = \frac{2\pi}{\lambda} \frac{1}{n_S\, cos\varphi} (I_x^0 + I_z^0) 2 n_2 k_2 \frac{\delta}{2} \tag{13}$$

In order to find the number N of molecules on the surface two populations $N_\parallel$ and $N_\perp$ are described (with $N = N_\parallel + N_\perp$). They are expressed regarding the orientation of their dynamic dipoles to the surface. $N_\parallel$ is the number corresponding to the projection of all the dynamic dipoles onto the surface plane, while $N_\perp$ corresponds to the projection of dipoles to the surface normal.

In order to obtain the number of molecules on the surface two assumptions have to be made. These assumptions describe that the vibrational behavior of the molecules is

the same on surface or in liquid. The first assumption concerns the absorption coefficients. We assume that the absorption coefficient of a certain chemical group is proportional to the volume concentration of this group, in solid and in liquid phase. And we suppose that the proportionality factor remains the same in both phases. The second assumption involves the real dielectric response. We assume that it is isotropic for the adsorbate layer and that it is identical to the response of the liquid ($\sqrt{\epsilon'_x} \approx \sqrt{\epsilon'_y} \approx \sqrt{\epsilon'_z} \approx n_2$). With the molecule concentration in liquid (C) we get:

$$\frac{N_\perp/\delta}{C/3} = \frac{\epsilon''_z}{2n_2k_2} \tag{14}$$

$$\frac{N_\parallel/2\delta}{C/3} = \frac{\epsilon''_x}{2n_2k_2} = \frac{\epsilon''_y}{2n_2k_2} \tag{15}$$

The factors "1/3" and "2" in the above equations are from the assumption that the medium is isotropic. This means that $N_\parallel$ takes into account I_x and I_y ($N_\perp = \frac{N_\parallel}{2} = \frac{N}{3}$).

With these assumptions one can derive $N_\parallel$ from the equations (7), (12) and (14):

$$N_\parallel = \frac{A_S}{A_S^0}\,\frac{I_y^0}{I_y}\,\frac{C}{3}\,\delta \tag{16}$$

And since the imaginary part of ϵ'' is negligible ($\epsilon_z'^{\,2} + \epsilon_z''^{\,2} \approx \epsilon_z'^{\,2}$) we retrieve:

$$N_\perp = \frac{I_y A_P - I_x A_S}{I_z A_S^0/n_1^4}\,\frac{I_y^0}{I_y}\,\frac{C}{3}\,\frac{\delta}{2} \tag{17}$$

The two equations (16) and (17) are sufficient to calculate the surface concentration of molecules. The only remaining parameters that have to be retrieved experimentally are A_S and A_P from solid phase, and C/A_S^0 from liquid phase. Therefore it is sufficient to conduct the calibration experiment in s-polarization at a known concentration to be able to calculate the surface concentration of molecules on surfaces. The calibration measurement is conducted in liquid phase in an *in situ* IR cell as displayed in Figure 61 (b). Several concentrations are measured to have multiple points of A_S^0 plotted over C, and a linear behavior should be observed. Taking the slope (A_S^0/C) allows the quantification at a high accuracy.

I.2.2. Quantification of acid groups

Fitting for vCO bands of acid groups

Moraillon et al. showed a fitting method of the IR-spectra of acid-terminated surfaces to calculate the surface density.[19] Here the vCO-peak is fitted with two peaks, a Guassian at ~1709 cm^{-1} and a Lorentzian at ~1715 cm^{-1} (see for example fit in Figure 17). The peak position of the vCO-band can shift quite strongly, depending on the surface composition. This is for example the case after aminolysis, were unreacted acid groups remain on the surface. In this case the position of the fitted curves should be shifted accordingly. Moraillon et al. retrieved the following values for calibration (with δ = 441 nm at λ = 1712 cm^{-1}):

$$N_{\parallel} = 6.57 \cdot 10^{15} A_S$$

$$N_{\perp} = 1.24 \cdot 10^{16} A_P - 1.12 \cdot 10^{16} A_S$$

Fitting for ester-NHS bands

The calibration measurements for ester-NHS terminated surfaces was carried out by Moraillon et al.[19,205] They proposed a multiple step fitting process to optimize the Gaussian/Lorentzian ratio of the peaks. Peaks are fitted at ~1650 cm^{-1}, ~1718 cm^{-1}, ~1742 cm^{-1}, ~1787 cm^{-1} and ~1815 cm^{-1}, but only the last two are used for the quantification. The retrieved the following values (with δ = 439 nm at λ = 1787 cm^{-1} and δ = 432 nm at λ = 1815 cm^{-1}):

$$N_{\parallel} = 1.16 \cdot 10^{16} \left(A_{S(1789)} + A_{S(1815)}\right)$$

$$N_{\perp} = 2.99 \cdot 10^{16} \left(A_{P(1789)} + A_{P(1815)}\right) - 1.90 \cdot 10^{16} \left(A_{S(1789)} + A_{S(1815)}\right)$$

A.II. SCANNING ELECTRON MICROSCOPY

Scanning electron microscopy takes advantage of the interaction of a focused electron beam with a sample. The sample is scanned point by point, one line after another. At each point the electron beam interacts with the sample, generating various different signals which can be used for evaluation. Generally, secondary electrons,

backscattered electrons and characteristic X-rays are analyzed. Secondary electrons (per definition low energies < 50 eV) are excited upon inelastic scattering. They give the best resolution and the contrast stems mainly from sample topography.[248] Back-scattered electrons are elastically back scattered from the sample nuclei. They can travel longer distances and originate from deeper areas than secondary electrons, which comparably worsens the lateral resolution. Their contrast originates from chemical differences or in other words from the differences in atomic number.[249] Despite its versatility and easiness to use, SEM has some major limitations, as the samples must be vacuum-tolerant and electrically conductive.

A.III. THERMAL VAPOR DEPOSITION

Thermal evaporation is one of the physical vapor deposition methods, and allows the deposition of thin films. The source material is heated in high vacuum with an electric heater (resistive or inductive) to temperatures near the melting point, thereby evaporating the source material. The vapor then condenses on the surface of the substrates, resulting in a thin film. The evaporation is conducted in high vacuum in order to avoid impurities in the film and to minimize collisions of the source material with remaining gas molecules (as they might react with each other). The quality of the film also depends on the purity of the source material.

The device used for the deposition of aluminium thin-films was constructed in-house and uses resistive heating for the evaporation process. An aluminium wire (99.999%, Chempur Germany) is hooked to a tungsten filament. The deposition chamber is then pumped to a vacuum of $25\text{-}35 \cdot 10^{-6}$ Torr. A current of 2 A is passed through the filament in order to evaporate the aluminium wire and the deposition thickness of 250 nm is ensured with a quartz crystal microbalance.

A.IV. PLASMA ENHANCED CHEMICAL VAPOR DEPOSITION

The thin a-$Si_{1-X}C_X$:H layers are deposited by plasma-enhanced chemical vapor deposition (PECVD) in the “low power regime” with a power density of 0.1 W/cm^{-2} and

a radio frequency (RF) of 13.56 MHz. The depositions are carried out with a substrate temperature of 250°C, a chamber pressure around 40 mTorr and a gas flow rate around 2 L/h. For the deposition to take place the precursor gases are introduced into a capacitively coupled chamber where they are dissociated by accelerated electrons in the RF-plasma. The ions which are thereby created in the plasma induce the deposition on the substrate. Amorphous silicon-carbon alloys can be deposited by choosing silane (SiH_4) and methane (CH_4) as precursor gasses.[241] The ratios of the gasses determine the carbon-content in the deposited thin films. Solomon et al. showed experimentally, that an a-$Si0_{0.85}C_{0.15}$:H layer requires a CH_4/SiH_4 ratio of 73/27 (or 1.45 L/h and 0.55 L/h, respectively). For an a-$Si0_{0.8}C_{0.2}$:H layer the CH_4/SiH_4 ratio is 81/19 (or 1.62 L/h and 0.38 L/h). The depositions can be carried out on a wide range of substrates (e.g. used during this thesis: glass slides, aluminium covered glass slides, crystalline silicon). The deposition time determines the thickness of the deposed layer, but depends on the carbon content. For a-$Si0_{0.85}C_{0.15}$:H the deposition rate was found to be 1.1 µm/h.

A.V. ROBOTIC SPOTTER

The robotic spotting is carried out on a Biorobotics MicroGrid II microarrayer (Figure 62). The slides are fixed by a vacuum and the spotting solutions are deposited at pre-programmed positions from a microplate with an arraying pin. This enables the spot-deposition of several different solutions on one slide. The spotting is conducted in a controlled climate (~60% humidity, 15-18°C room temperature) and the spotted slides are stored overnight in a humidifier with ~75% humidity.



Figure 62: MicroGrid II robotic spotter.[250]

A.VI. FLUORESCENCE IMAGING

The fluorescence was measured with a Genewave Diagarray scanner (Figure 63). The inserted slides are illuminated with LEDs at 650 nm for Cy5 or at 550 nm for Cy 3, and the images are captured with the Diagarray software.



Figure 63: Diagarray fluorescence scanner.

The analysis of the images is partially conducted with the Diagarray software, which can automatically select the spots. The automatic selection of spots is only reliable when they are homogenous and round, as well as when their fluorescence intensity is significantly higher than the background. When the automatic selection is not reliable, a manual adjustment is necessary, as can be seen in the example in Figure 64.

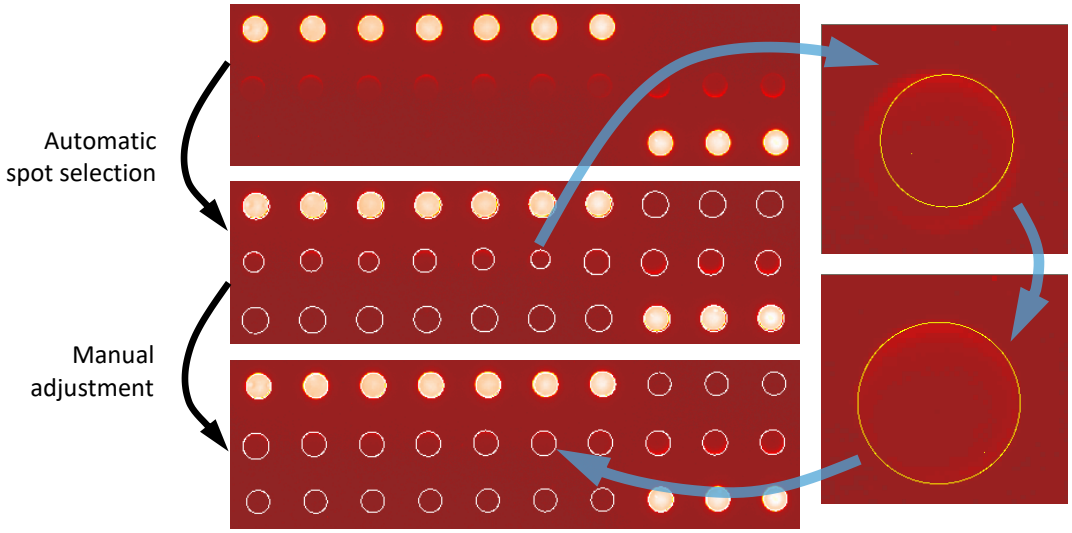


Figure 64: Example of bad automatic spot selection by Diagarray software and necessary manual adjustment.

Visibly bad spots (outliers) are excluded manually from further analysis. These spots are for example very inhomogeneous spots, or spots which are visibly different from the spots of the same type, as shown in Figure 65.

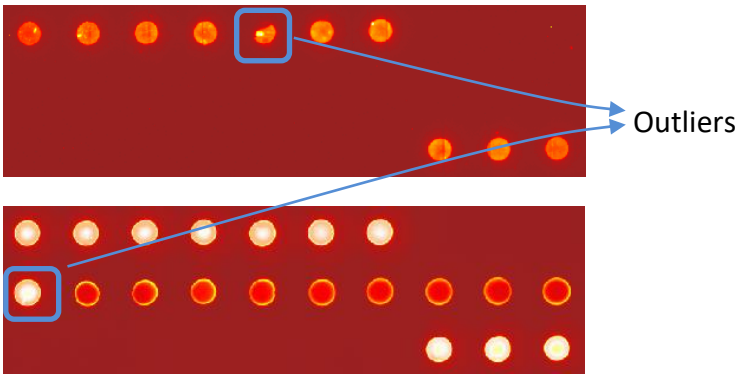


Figure 65: Examples of outlier spots.

The Diagarray software can then retrieve the properties of each spot. These include among others: diameter, position, and number of pixels in circle; It furthermore calculates for each spot the background, the median intensity, mean intensity, and the

standard deviation. Depending on the homogeneity of the spots, either the median intensity or the mean intensity are used. The median is generally statistically more stable in case of high inhomogeneity. The background is subtracted for each spot, and the average of all spots of the one type is then used for further analysis of the behaviour during the experiments.

REFERENCES

1. Costigliola V, Quagliata F. *Detection of Bacteria, Viruses, Parasites and Fungi*. (Viola Magni M, ed.). Dordrecht: Springer Netherlands; 2010. doi:10.1007/978-90-481-8544-3.
2. Vo-Dinh T. Biosensors and Biochips. In: Ferrari M, Bashir R, Wereley S, eds. *BioMEMS and Biomedical Nanotechnology*. Boston, MA: Springer US; 2007:1-20. doi:10.1007/978-0-387-25845-4_1.
3. Clark LC, Lyons C. Electrode systems for continuous monitoring in cardiovascular surgery. *Ann N Y Acad Sci*. 2006;102(1):29-45. doi:10.1111/j.1749-6632.1962.tb13623.x.
4. D'Orazio P. Biosensors in clinical chemistry. *Clin Chim Acta*. 2003;334(1-2):41-69. doi:10.1016/S0009-8981(03)00241-9.
5. Cho EJ, Lee J-W, Ellington AD. Applications of Aptamers as Sensors. *Annu Rev Anal Chem*. 2009;2(1):241-264. doi:10.1146/annurev.anchem.1.031207.112851.
6. Seok Kim Y, Ahmad Raston NH, Bock Gu M. Aptamer-based nanobiosensors. *Biosens Bioelectron*. 2016;76:2-19. doi:10.1016/j.bios.2015.06.040.
7. Sharma S, Byrne H, O'Kennedy RJ. Antibodies and antibody-derived analytical biosensors. *Essays Biochem*. 2016;60(1):9-18. doi:10.1042/EBC20150002.
8. Amine A, Arduini F, Moscone D, Palleschi G. Recent advances in biosensors based on enzyme inhibition. *Biosens Bioelectron*. 2016;76:180-194. doi:10.1016/j.bios.2015.07.010.
9. Gutiérrez JC, Amaro F, Marti-n-Gonzalez A. Heavy metal whole-cell biosensors using eukaryotic microorganisms: an updated critical review. *Front Microbiol*. 2015;6. doi:10.3389/fmicb.2015.00048.
10. De Michele R, Carimi F, Frommer WB. Mitochondrial biosensors. *Int J Biochem Cell Biol*. 2014;48:39-44. doi:10.1016/j.biocel.2013.12.014.
11. Jayasena SD. Aptamers: An emerging class of molecules that rival antibodies in diagnostics. *Clin Chem*. 1999;45(9):1628-1650. doi:10.1038/mtna.2014.74.
12. Sassolas A, Leca-Bouvier BD, Blum LJ. DNA Biosensors and Microarrays. *Chem Rev*. 2008;108(1):109-139. doi:10.1021/cr0684467.
13. Faucheux A, Gouget-Laemmel AC, Allongue P, Henry de Villeneuve C, Ozanam F, Chazalviel J-N. Mechanisms of Thermal Decomposition of Organic Monolayers Grafted on (111) Silicon. *Langmuir*. 2007;23(3):1326-1332. doi:10.1021/la061260i.
14. Touahir L, Allongue P, Aureau D, Boukherroub R, Chazalviel J-N, Galopin E, Gouget-Laemmel AC, de Villeneuve CH, Moraillon A, Niedziółka-Jönsson J, Ozanam F, Andresa JS, Sam S, Solomon I, Szunerits S. Molecular monolayers on silicon as substrates for biosensors. *Bioelectrochemistry*. 2010;80(1):17-25. doi:10.1016/j.bioelechem.2010.03.011.
15. Warntjes M. Electrochemical Methoxylation of Porous Silicon Surface. *J Electrochem Soc*. 1995;142(12):4138. doi:10.1149/1.2048476.
16. Fellah S, Teyssot A, Ozanam F, Chazalviel J-N, Vigneron J, Etcheberry A. Kinetics of Electrochemical Derivatization of the Silicon Surface by Grignards. *Langmuir*. 2002;18(15):5851-5860. doi:10.1021/la0203739.
17. Faucheux A, Gouget-Laemmel AC, Henry de Villeneuve C, Boukherroub R, Ozanam F, Allongue P, Chazalviel J-N. Well-Defined Carboxyl-Terminated Alkyl Monolayers Grafted onto H−Si(111): Packing Density from a Combined AFM and Quantitative IR Study. *Langmuir*. 2006;22(1):153-162. doi:10.1021/la052145v.
18. Sam S, Touahir L, Salvador Andresa J, Allongue P, Chazalviel J-N, Gouget-

Laemmel a. C, Henry de Villeneuve C, Moraillon A, Ozanam F, Gabouze N, Djebbar S. Semiquantitative Study of the EDC/NHS Activation of Acid Terminal Groups at Modified Porous Silicon Surfaces. *Langmuir*. 2010;26(2):809-814. doi:10.1021/la902220a.

19. Moraillon A, Gouget-Laemmel AC, Ozanam F, Chazalviel J-N. Amidation of Monolayers on Silicon in Physiological Buffers: A Quantitative IR Study. *J Phys Chem C*. 2008;112(18):7158-7167. doi:10.1021/jp7119922.
20. Touahir L, Moraillon A, Allongue P, Chazalviel J-N, Henry de Villeneuve C, Ozanam F, Solomon I, Gouget-Laemmel AC. Highly sensitive and reusable fluorescence microarrays based on hydrogenated amorphous silicon–carbon alloys. *Biosens Bioelectron*. 2009;25(4):952-955. doi:10.1016/j.bios.2009.08.046.
21. Galopin E, Touahir L, Niedziółka-Jönsson J, Boukherroub R, Gouget-Laemmel AC, Chazalviel J-N, Ozanam F, Szunerits S. Amorphous silicon–carbon alloys for efficient localized surface plasmon resonance sensing. *Biosens Bioelectron*. 2010;25(5):1199-1203. doi:10.1016/j.bios.2009.10.012.
22. Touahir L, Galopin E, Boukherroub R, Chantal Gouget-Laemmel A, Chazalviel J-N, Ozanam F, Saison O, Akjouj A, Pennec Y, Djafari-Rouhani B, Szunerits S. Plasmonic properties of silver nanostructures coated with an amorphous silicon–carbon alloy and their applications for sensitive sensing of DNA hybridization. *Analyst*. 2011;136(9):1859. doi:10.1039/c0an01022g.
23. Touahir L, Galopin E, Boukherroub R, Gouget-Laemmel AC, Chazalviel J-N, Ozanam F, Szunerits S. Localized surface plasmon-enhanced fluorescence spectroscopy for highly-sensitive real-time detection of DNA hybridization. *Biosens Bioelectron*. 2010;25(12):2579-2585. doi:10.1016/j.bios.2010.04.026.
24. NIAID Emerging Infectious Diseases/Pathogens. https://www.niaid.nih.gov/research/emerging-infectious-diseases-pathogens. Accessed August 26, 2016.
25. Pallen MJ, Nelson KE, Preston GM. *Bacterial Pathogenomics*. Wasington DC: ASM Press; 2007.
26. De Scott B. Toxigenic fungi isolated from cereal and legume products. *Mycopathol Mycol Appl*. 1965;25(3-4):213-222. doi:10.1007/BF02049914.
27. van der Merwe KJ, Steyn PS, Fourie L. Mycotoxins. Part II. The constitution of ochratoxins A, B, and C, metabolites of Aspergillus ochraceus wilh. *J Chem Soc*. 1965:7083. doi:10.1039/jr9650007083.
28. van der Merwe KJ, Steyn PS, Fourie L, Scott de B., Theron JJ. Ochratoxin A, a Toxic Metabolite produced by Aspergillus ochraceus Wilh. *Nature*. 1965;205(4976):1112-1113. doi:10.1038/2051112a0.
29. Hutchison RD, Steyn PS, Thompson DL. The isolation and structure of 4-hydroxyochratoxin A and 7-carboxy-3,4-dihydro-8-hydroxy-3-methylisocoumarin from penicillium viridicatum. *Tetrahedron Lett*. 1971;12(43):4033-4036. doi:10.1016/S0040-4039(01)97353-8.
30. Abarca ML, Bragulat MR, Castellá G, Cabañes FJ. Ochratoxin A production by strains of Aspergillus niger var. niger. *Appl Environ Microbiol*. 1994;60(7):2650-2652. http://www.ncbi.nlm.nih.gov/pubmed/8074536.
31. Ciegler A. Bioproduction of ochratoxin A and penicillic acid by members of the Aspergillus ochraceus group. *Can J Microbiol*. 1972;18(5):631-636. doi:10.1139/m72-100.
32. Bayman P, Baker JL, Doster MA, Michailides TJ, Mahoney NE. Ochratoxin

Production by the Aspergillus ochraceus Group and Aspergillus alliaceus. *Appl Environ Microbiol*. 2002;68(5):2326-2329. doi:10.1128/AEM.68.5.2326-2329.2002.

33. Speijers GJA, Van Egmond HP. Worldwide ochratoxin A levels in food and feeds. In: *Human Ochratoxicosis and Its Pathologies*. INSERM John Libbey Eurotext Ltd; 1993:85.
34. Jørgensen K, Jacobsen JS. Occurrence of ochratoxin A in Danish wheat and rye, 1992-99. *Food Addit Contam*. 2002;19(12):1184-1189. doi:10.1080/0265203021000012376.
35. Jørgensen K. Occurrence of ochratoxin A in commodities and processed food--a review of EU occurrence data. *Food Addit Contam*. 2005;22 Suppl 1(October 2014):26-30. doi:10.1080/02652030500344811.
36. Steyn PS. *Mycotoxins: Production, Isolation, Separation and Purification*. Developmen. (BETINA V, ed.). Elsevier; 1984.
37. Krogh P, Hald B, Pedersen EJ. Occurrence of ochratoxin A and citrinin in cereals associated with mycotoxic porcine necropathy. *Acta Pathol Microbiol Scand Sect B Microbiol Immunol*. 2009;81B(6):689-695. doi:10.1111/j.1699-0463.1973.tb02261.x.
38. Ribelin WE, Fukushima K, Still PE. The toxicity of ochratoxin to ruminants. *Can J Comp Med Rev Can médecine Comp*. 1978;42(2):172-176. http://www.pubmedcentral.nih.gov/articlerender.fcgi?artid=1277611&tool=pmcentrez&rendertype=abstract.
39. Gayathri L, Dhivya R, Dhanasekaran D, Periasamy VS, Alshatwi AA, Akbarsha MA. Hepatotoxic effect of ochratoxin A and citrinin, alone and in combination, and protective effect of vitamin E: In vitro study in HepG2 cell. *Food Chem Toxicol*. 2015;83:151-163. doi:10.1016/j.fct.2015.06.009.
40. Qi X, Yang X, Chen S, He X, Dweep H, Guo M, Cheng W, Xu W, Luo Y, Gretz N, Dai Q, Huang K. Ochratoxin A induced early hepatotoxicity: new mechanistic insights from microRNA, mRNA and proteomic profiling studies. *Sci Rep*. June 2014:1-14. doi:10.1038/srep05163.
41. Miki T, Fukui Y, Uemura N, Takeuchi Y. Regional difference in the neurotoxicity of ochratoxin A on the developing cerebral cortex in mice. *Brain Res Dev Brain Res*. 1994;82(1-2):259-264. http://www.ncbi.nlm.nih.gov/pubmed/7842513.
42. Sava V, Reunova O, Velasquez A, Harbison R, Sanchez-Ramos J. Acute neurotoxic effects of the fungal metabolite ochratoxin-A. *Neurotoxicology*. 2006;27(1):82-92. doi:10.1016/j.neuro.2005.07.004.
43. Gilani SH, Bancroft J, Reily M. Teratogenicity of ochratoxin A in chick embryos. *Toxicol Appl Pharmacol*. 1978;46(2):543-546. doi:10.1016/0041-008X(78)90099-6.
44. Brown MH, Szczech GM, Purmalis BP. Teratogenic and toxic effects of ochratoxin A in rats. *Toxicol Appl Pharmacol*. 1976;37(2):331-338. doi:10.1016/0041-008X(76)90096-X.
45. Luster MI, Germolec DR, Burleson GR, Jameson CW, Ackermann MF, Lamm KR, Hayes HT. Selective Immunosuppression in Mice of Natural Killer Cell Activity by Ochratoxin A. *Cancer Res*. 1987;47(9):2259-2263. http://cancerres.aacrjournals.org/content/47/9/2259.
46. Al-Anati L, Katz N, Petzinger E. Interference of arachidonic acid and its metabolites with TNF-α release by ochratoxin A from rat liver. *Toxicology*.

2005;208(3):335-346. doi:10.1016/j.tox.2004.11.025.
47. Bendele AM, Carlton WW, Krogh P, Lillehoj EB. Ochratoxin A carcinogenesis in the (C57BL/6J X C3H)F1 mouse. *J Natl Cancer Inst*. 1985;75(4):733-742. http://www.ncbi.nlm.nih.gov/pubmed/3862905.
48. Mantle P, Kulinskaya E, Nestler S. Renal tumourigenesis in male rats in response to chronic dietary ochratoxin A. *Food Addit Contam*. 2005;22(1):58-64. doi:10.1080/02652030500358431.
49. EFSA. EFSA evaluates ochratoxin A in food and derives a Tolerable Weekly Intake. http://www.efsa.europa.eu/en/press/news/contam060609. Accessed September 23, 2016.
50. US Food and Drug Administration. www.fda.gov.
51. Kunsagi Z. *Report on the Validation of a Method for the Determination of Ochratoxin A in Capsicum Spp . (Paprika and Chilli)*.; 2012. doi:10.2787/64803.
52. Hernández MJ, García-Moreno MV, Durán E, Guillén D, Barroso CG. Validation of two analytical methods for the determination of ochratoxin A by reversed-phased high-performance liquid chromatography coupled to fluorescence detection in musts and sweet wines from Andalusia. *Anal Chim Acta*. 2006;566(1):117-121. doi:10.1016/j.aca.2006.02.002.
53. Solfrizzo M, Gambacorta L, Lattanzio VMT, Powers S, Visconti A. Simultaneous LC–MS/MS determination of aflatoxin M1, ochratoxin A, deoxynivalenol, de-epoxydeoxynivalenol, α and β-zearalenols and fumonisin B1 in urine as a multi-biomarker method to assess exposure to mycotoxins. *Anal Bioanal Chem*. 2011;401(9):2831-2841. doi:10.1007/s00216-011-5354-z.
54. Prieto-Simón B, Campàs M, Marty J-L, Noguer T. Novel highly-performing immunosensor-based strategy for ochratoxin A detection in wine samples. *Biosens Bioelectron*. 2008;23(7):995-1002. doi:10.1016/j.bios.2007.10.002.
55. Prieto-Simón B, Karube I, Saiki H. Sensitive detection of ochratoxin A in wine and cereals using fluorescence-based immunosensing. *Food Chem*. 2012;135(3):1323-1329. doi:10.1016/j.foodchem.2012.05.060.
56. Mandal PK, Biswas AK, Choi K, Pal UK. Methods for Rapid Detection of Foodborne Pathogens: An Overview. *Am J Food Technol*. 2011;6(2):87-102. doi:10.3923/ajft.2011.87.102.
57. Law JW-F, Ab Mutalib N-S, Chan K-G, Lee L-H. Rapid methods for the detection of foodborne bacterial pathogens: principles, applications, advantages and limitations. *Front Microbiol*. 2015;5. doi:10.3389/fmicb.2014.00770.
58. Mullis KB, Erlich HA, Arnheim N, Horn GT, Saiki RK, Scharf SJ. Process for amplifying, detecting, and/or-cloning nucleic acid sequences. 1987. http://www.google.co.jp/patents/US4683195.
59. Filion M. *Quantitative Real-Time PCR in Applied Microbiology*. Caister Academic Press; 2012.
60. Lazcka O, Campo FJ Del, Muñoz FX. Pathogen detection: A perspective of traditional methods and biosensors. *Biosens Bioelectron*. 2007;22(7):1205-1217. doi:10.1016/j.bios.2006.06.036.
61. Iqbal SS, Mayo MW, Bruno JG, Bronk B V, Batt CA, Chambers JP. A review of molecular recognition technologies for detection of biological threat agents. *Biosens Bioelectron*. 2000;15(11-12):549-578. doi:10.1016/S0956-5663(00)00108-1.
62. Engvall E, Perlmann P. Enzyme-linked immunosorbent assay (ELISA) quantitative

assay of immunoglobulin G. *Immunochemistry*. 1971;8(9):871-874. doi:10.1016/0019-2791(71)90454-X.

63. Rohr TE. Magnetically assisted binding assays using magnetically labeled binding members. 1995. https://www.google.com/patents/US5445971.
64. Yetisen AK, Akram MS, Lowe CR. Paper-based microfluidic point-of-care diagnostic devices. *Lab Chip*. 2013;13(12):2210-2251. doi:10.1039/c3lc50169h.
65. Sajid M, Kawde AN, Daud M. Designs, formats and applications of lateral flow assay: A literature review. *J Saudi Chem Soc*. 2015;19(6):689-705. doi:10.1016/j.jscs.2014.09.001.
66. Gan SD, Patel KR. Enzyme immunoassay and enzyme-linked immunosorbent assay. *J Invest Dermatol*. 2013;133(9):e12. doi:10.1038/jid.2013.287.
67. Karube I, Nomura Y. Enzyme sensors for environmental analysis. *J Mol Catal B Enzym*. 2000;10(1-3):177-181. doi:10.1016/S1381-1177(00)00125-9.
68. Dong S, Wang B. Electrochemical Biosensing in Extreme Environment. *Electroanalysis*. 2002;14(1):7-16. doi:10.1002/1521-4109(200201)14:1<7::AID-ELAN7>3.0.CO;2-V.
69. Solanki PR, Kaushik A, Manaka T, Pandey MK, Iwamoto M, Agrawal V V, Malhotra BD. Self-assembled monolayer based impedimetric platform for food borne mycotoxin detection. *Nanoscale*. 2010;2(12):2811-2817. doi:10.1039/c0nr00289e.
70. Ensafi AA, Rezaei B, Amini M, Heydari-Bafrooei E. A novel sensitive DNA-biosensor for detection of a carcinogen, Sudan II, using electrochemically treated pencil graphite electrode by voltammetric methods. *Talanta*. 2012;88:244-251. doi:10.1016/j.talanta.2011.10.038.
71. Liu G, Mao X, Phillips JA, Xu H, Tan W, Zeng L. Aptamer−Nanoparticle Strip Biosensor for Sensitive Detection of Cancer Cells. *Anal Chem*. 2009;81(24):10013-10018. doi:10.1021/ac901889s.
72. Kumar S, Kumar S, Srivastava S, Yadav BK, Lee SH, Sharma JG, Doval DC, Malhotra BD. Reduced graphene oxide modified smart conducting paper for cancer biosensor. *Biosens Bioelectron*. 2015;73:114-122. doi:10.1016/j.bios.2015.05.040.
73. Mauriz E, Calle A, Manclús JJ, Montoya A, Hildebrandt A, Barceló D, Lechuga LM. Optical immunosensor for fast and sensitive detection of DDT and related compounds in river water samples. *Biosens Bioelectron*. 2007;22(7):1410-1418. doi:10.1016/j.bios.2006.06.016.
74. Andreou VG, Clonis YD. A portable fiber-optic pesticide biosensor based on immobilized cholinesterase and sol–gel entrapped bromcresol purple for in-field use. *Biosens Bioelectron*. 2002;17(1-2):61-69. doi:10.1016/S0956-5663(01)00261-5.
75. Marrazza G, Chianella I, Mascini M. Disposable DNA electrochemical biosensors for environmental monitoring. *Anal Chim Acta*. 1999;387(3):297-307. doi:10.1016/S0003-2670(99)00051-3.
76. Bagni G, Osella D, Sturchio E, Mascini M. Deoxyribonucleic acid (DNA) biosensors for environmental risk assessment and drug studies. *Anal Chim Acta*. 2006;573-574:81-89. doi:10.1016/j.aca.2006.03.085.
77. Moll N, Pascal E, Dinh DH, Pillot J-P, Bennetau B, Rebière D, Moynet D, Mas Y, Mossalayi D, Pistré J, Déjous C. A Love wave immunosensor for whole E. coli bacteria detection using an innovative two-step immobilisation approach.

Biosens Bioelectron. 2007;22(9-10):2145-2150. doi:10.1016/j.bios.2006.09.032.
78. Chan KY, Ye WW, Zhang Y, Xiao LD, Leung PHM, Li Y, Yang M. Ultrasensitive detection of E. coli O157:H7 with biofunctional magnetic bead concentration via nanoporous membrane based electrochemical immunosensor. *Biosens Bioelectron*. 2013;41(1):532-537. doi:10.1016/j.bios.2012.09.016.
79. Iqbal SS, Mayo MW, Bruno JG, Bronk B V., Batt CA, Chambers JP. A review of molecular recognition technologies for detection of biological threat agents. *Biosens Bioelectron*. 2000;15(11-12):549-578. doi:10.1016/S0956-5663(00)00108-1.
80. Uslu F, Ingebrandt S, Mayer D, Böcker-Meffert S, Odenthal M, Offenhäusser A. Labelfree fully electronic nucleic acid detection system based on a field-effect transistor device. *Biosens Bioelectron*. 2004;19(12):1723-1731. doi:10.1016/j.bios.2004.01.019.
81. He Y, Zhang S, Zhang X, Baloda M, Gurung AS, Xu H, Zhang X, Liu G. Ultrasensitive nucleic acid biosensor based on enzyme–gold nanoparticle dual label and lateral flow strip biosensor. *Biosens Bioelectron*. 2011;26(5):2018-2024. doi:10.1016/j.bios.2010.08.079.
82. Yang C, Wang Y, Marty J-L, Yang X. Aptamer-based colorimetric biosensing of Ochratoxin A using unmodified gold nanoparticles indicator. *Biosens Bioelectron*. 2011;26(5):2724-2727. doi:10.1016/j.bios.2010.09.032.
83. Barthelmebs L, Jonca J, Hayat A, Prieto-Simon B, Marty JL. Enzyme-Linked Aptamer Assays (ELAAs), based on a competition format for a rapid and sensitive detection of Ochratoxin A in wine. *Food Control*. 2011;22(5):737-743. doi:10.1016/j.foodcont.2010.11.005.
84. Miodek A, Castillo G, Hianik T, Korri-Youssoufi H. Electrochemical aptasensor of cellular prion protein based on modified polypyrrole with redox dendrimers. *Biosens Bioelectron*. 2014;56:104-111. doi:10.1016/j.bios.2013.12.051.
85. Piro B, Kapella A, Le VH, Anquetin G, Zhang QD, Reisberg S, Noel V, Tran LD, Duc HT, Pham MC. Towards the detection of human papillomavirus infection by a reagentless electrochemical peptide biosensor. *Electrochim Acta*. 2011;56(28):10688-10693. doi:10.1016/j.electacta.2011.04.094.
86. Subramanian A, Irudayaraj J, Ryan T. A mixed self-assembled monolayer-based surface plasmon immunosensor for detection of E. coli O157:H7. *Biosens Bioelectron*. 2006;21(7):998-1006. doi:10.1016/j.bios.2005.03.007.
87. Wang SG, Zhang Q, Wang R, Yoon SF, Ahn J, Yang DJ, Tian JZ, Li JQ, Zhou Q. Multi-walled carbon nanotubes for the immobilization of enzyme in glucose biosensors. *Electrochem commun*. 2003;5(9):800-803. doi:10.1016/j.elecom.2003.07.007.
88. Kharitonov AB, Zayats M, Lichtenstein A, Katz E, Willner I. Enzyme monolayer-functionalized field-effect transistors for biosensor applications. *Sensors Actuators B Chem*. 2000;70(1-3):222-231. doi:10.1016/S0925-4005(00)00573-6.
89. Blackburn GF, Talley DB, Booth PM, Durfor CN, Martin MT, Napper AD, Rees AR. Potentiometric biosensor employing catalytic antibodies as the molecular recognition element. *Anal Chem*. 1990;62(20):2211-2216. doi:10.1021/ac00219a011.
90. Blackburn GF, Durfor C, Powell MJ, Massey RJ. Catalytic antibodies as chemical sensors. 2005. https://www.google.com/patents/US6846654.
91. Rusmini F, Zhong Z, Feijen J. Protein Immobilization Strategies for Protein

Biochips. *Biomacromolecules*. 2007;8(6):1775-1789. doi:10.1021/bm061197b.

92. Wong CL, Ho HP, Suen YK, Kong SK, Chen QL, Yuan W, Wu SY. Real-time protein biosensor arrays based on surface plasmon resonance differential phase imaging. *Biosens Bioelectron*. 2008;24(4):606-612. doi:10.1016/j.bios.2008.06.013.
93. Védrine C, Leclerc J-C, Durrieu C, Tran-Minh C. Optical whole-cell biosensor using Chlorella vulgaris designed for monitoring herbicides. *Biosens Bioelectron*. 2003;18(4):457-463. doi:10.1016/S0956-5663(02)00157-4.
94. Bahl MI, Hansen LH, Licht TR, Sorensen SJ. In Vivo Detection and Quantification of Tetracycline by Use of a Whole-Cell Biosensor in the Rat Intestine. *Antimicrob Agents Chemother*. 2004;48(4):1112-1117. doi:10.1128/AAC.48.4.1112-1117.2004.
95. D'Souza SF. Microbial biosensors. *Biosens Bioelectron*. 2001;16(6):337-353. doi:10.1016/S0956-5663(01)00125-7.
96. Rizzuto R, Pinton P, Brini M, Chiesa A, Filippin L, Pozzan T. Mitochondria as biosensors of calcium microdomains. *Cell Calcium*. 1999;26(5):193-200. doi:10.1054/ceca.1999.0076.
97. Hoffman TL, Canziani G, Jia L, Rucker J, Doms RW. A biosensor assay for studying ligand-membrane receptor interactions: Binding of antibodies and HIV-1 Env to chemokine receptors. *Proc Natl Acad Sci*. 2000;97(21):11215-11220. doi:10.1073/pnas.190274097.
98. Quintana A, Raczka E, Piehler L, Lee I, Myc A, Majoros I, Patri AK, Thomas T, Mulé J, Baker, Jr. JR. Design and Function of a Dendrimer-Based Therapeutic Nanodevice Targeted to Tumor Cells Through the Folate Receptor. *Pharm Res*. 2002;19(9):1310-1316. doi:10.1023/A:1020398624602.
99. Oungpipat W, Alexander PW, Southwell-Keely P. A reagentless amperometric biosensor for hydrogen peroxide determination based on asparagus tissue and ferrocene mediation. *Anal Chim Acta*. 1995;309(1-3):35-45. doi:10.1016/0003-2670(95)00066-9.
100. Itoh T, Shimomura T, Hayashi A, Yamaguchi A, Teramae N, Ono M, Tsunoda T, Mizukami F, Stucky GD, Hanaoka T. Electrochemical enzymatic biosensor with long-term stability using hybrid mesoporous membrane. *Analyst*. 2014;139(18):4654. doi:10.1039/C4AN00975D.
101. Hussain M, Wackerlig J, Lieberzeit P. Biomimetic Strategies for Sensing Biological Species. *Biosensors*. 2013;3(1):89-107. doi:10.3390/bios3010089.
102. Sassolas A, Blum LJ, Leca-Bouvier BD. Electrochemical Aptasensors. *Electroanalysis*. 2009;21(11):1237-1250. doi:10.1002/elan.200804554.
103. Clerc D, Lukosz W. Direct immunosensing with an integrated-optical output grating coupler. *Sensors Actuators B Chem*. 1997;40(1):53-58. doi:10.1016/S0925-4005(97)80199-2.
104. Wandermur G, Rodrigues D, Allil R, Queiroz V, Peixoto R, Werneck M, Miguel M. Plastic optical fiber-based biosensor platform for rapid cell detection. *Biosens Bioelectron*. 2014;54:661-666. doi:10.1016/j.bios.2013.11.030.
105. Park J-H, Byun J-Y, Mun H, Shim W-B, Shin Y-B, Li T, Kim M-G. A regeneratable, label-free, localized surface plasmon resonance (LSPR) aptasensor for the detection of ochratoxin A. *Biosens Bioelectron*. 2014;59:321-327. doi:10.1016/j.bios.2014.03.059.
106. Borisov SM, Wolfbeis OS. Optical Biosensors. *Chem Rev*. 2008;108(2):423-461.

doi:10.1021/cr068105t.
107. Marrazza G. Piezoelectric Biosensors for Organophosphate and Carbamate Pesticides: A Review. *Biosensors*. 2014;4(3):301-317. doi:10.3390/bios4030301.
108. Faegh S, Jalili N, Sridhar S. A self-sensing piezoelectric microcantilever biosensor for detection of ultrasmall adsorbed masses: theory and experiments. *Sensors (Basel)*. 2013;13(5):6089-6108. doi:10.3390/s130506089.
109. DeMiguel-Ramos M, Díaz-Durán B, Escolano J-M, Barba M, Mirea T, Olivares J, Clement M, Iborra E. Gravimetric biosensor based on a 1.3GHz AlN shear-mode solidly mounted resonator. *Sensors Actuators B Chem*. September 2016. doi:10.1016/j.snb.2016.09.079.
110. Kopparthy V, Crews N. Microscale Thermal Biosensor: Critical Design Considerations and Optimization. In: *2016 32nd Southern Biomedical Engineering Conference (SBEC)*. IEEE; 2016:127-127. doi:10.1109/SBEC.2016.36.
111. Devkota J, Howell M, Mukherjee P, Srikanth H, Mohapatra S, Phan MH. Magneto-reactance based detection of MnO nanoparticle-embedded Lewis lung carcinoma cells. *J Appl Phys*. 2015;117(17):17D123. doi:10.1063/1.4914950.
112. Tuerk C, Gold L. Systematic evolution of ligands by exponential enrichment: RNA ligands to bacteriophage T4 DNA polymerase. *Science (80-)*. 1990;249(4968):505-510.
113. Ellington AD, Szostak JW. In vitro selection of RNA molecules that bind specific ligands. *Nature*. 1990;346(6287):818-822. doi:10.1038/346818a0.
114. Torres-Chavolla E, Alocilja EC. Aptasensors for detection of microbial and viral pathogens. *Biosens Bioelectron*. 2009;24(11):3175-3182. doi:10.1016/j.bios.2008.11.010.
115. Wang Y-X, Ye Z-Z, Si C-Y, Ying Y-B. Application of Aptamer Based Biosensors for Detection of Pathogenic Microorganisms. *Chinese J Anal Chem*. 2012;40(4):634-642. doi:10.1016/S1872-2040(11)60542-2.
116. Song S, Wang L, Li J, Fan C, Zhao J. Aptamer-based biosensors. *TrAC - Trends Anal Chem*. 2008;27(2):108-117. doi:10.1016/j.trac.2007.12.004.
117. Deng Q, German I, Buchanan D, Kennedy RT. Retention and Separation of Adenosine and Analogues by Affinity Chromatography with an Aptamer Stationary Phase. *Anal Chem*. 2001;73(22):5415-5421. doi:10.1021/ac0105437.
118. De Girolamo A, McKeague M, Miller JD, Derosa MC, Visconti A. Determination of ochratoxin A in wheat after clean-up through a DNA aptamer-based solid phase extraction column. *Food Chem*. 2011;127(3):1378-1384. doi:10.1016/j.foodchem.2011.01.107.
119. Mascini M. Aptamers and their applications. *Anal Bioanal Chem*. 2008;390(4):987-988. doi:10.1007/s00216-007-1769-y.
120. E. Wang R, Zhang Y, Cai J, Cai W, Gao T. Aptamer-Based Fluorescent Biosensors. *Curr Med Chem*. 2011;18(27):4175-4184. doi:10.2174/092986711797189637.
121. Radom F, Jurek PM, Mazurek MP, Otlewski J, Jeleń F. Aptamers: Molecules of great potential. *Biotechnol Adv*. 2013;31(8):1260-1274. doi:10.1016/j.biotechadv.2013.04.007.
122. Li L, Li B, Qi Y, Jin Y. Label-free aptamer-based colorimetric detection of mercury ions in aqueous media using unmodified gold nanoparticles as colorimetric probe. *Anal Bioanal Chem*. 2009;393(8):2051-2057. doi:10.1007/s00216-009-2640-0.
123. Song K-M, Lee S, Ban C. Aptamers and Their Biological Applications. *Sensors*.

2012;12(12):612-631. doi:10.3390/s120100612.
124. Mayer G. The chemical biology of aptamers. *Angew Chemie - Int Ed*. 2009;48(15):2672-2689. doi:10.1002/anie.200804643.
125. Ellington A, Szostak J. Selection in vitro of single-stranded DNA molecules that fold into specific ligand-binding structures. *Nature*. 1992;355:850-852. doi:10.1038/355850a0.
126. Cox JC, Ellington AD. Automated selection of anti-protein aptamers. *Bioorganic Med Chem*. 2001;9(10):2525-2531. doi:10.1016/S0968-0896(01)00028-1.
127. Hermann T. Adaptive Recognition by Nucleic Acid Aptamers. *Science (80-)*. 2000;287(5454):820-825. doi:10.1126/science.287.5454.820.
128. Cruz-Aguado JA, Penner G. Determination of Ochratoxin A with a DNA Aptamer. *J Agric Food Chem*. 2008;56(22):10456-10461. doi:10.1021/jf801957h.
129. Wang C, Dong X, Liu Q, Wang K. Label-free colorimetric aptasensor for sensitive detection of ochratoxin A utilizing hybridization chain reaction. *Anal Chim Acta*. 2015;860:83-88. doi:10.1016/j.aca.2014.12.031.
130. Liu Y, Yu J, Wang Y, Liu Z, Lu Z. An ultrasensitive aptasensor for detection of Ochratoxin A based on shielding effect-induced inhibition of fluorescence resonance energy transfer. *Sensors Actuators B Chem*. 2016;222:797-803. doi:10.1016/j.snb.2015.09.007.
131. Hayat A, Mishra RK, Catanante G, Marty JL. Development of an aptasensor based on a fluorescent particles-modified aptamer for ochratoxin A detection. *Anal Bioanal Chem*. 2015;407(25):7815-7822. doi:10.1007/s00216-015-8952-3.
132. Wu S, Duan N, Wang Z, Wang H. Aptamer-functionalized magnetic nanoparticle-based bioassay for the detection of ochratoxin a using upconversion nanoparticles as labels. *Analyst*. 2011;136(11):2306. doi:10.1039/c0an00735h.
133. Galarreta BC, Tabatabaei M, Guieu V, Peyrin E, Lagugné-Labarthet F. Microfluidic channel with embedded SERS 2D platform for the aptamer detection of ochratoxin A. *Anal Bioanal Chem*. 2013;405(5):1613-1621. doi:10.1007/s00216-012-6557-7.
134. Ma W, Yin H, Xu L, Xu Z, Kuang H, Wang L, Xu C. Femtogram ultrasensitive aptasensor for the detection of OchratoxinA. *Biosens Bioelectron*. 2013;42:545-549. doi:10.1016/j.bios.2012.11.024.
135. Yang X, Qian J, Jiang L, Yan Y, Wang K, Liu Q, Wang K. Ultrasensitive electrochemical aptasensor for ochratoxin A based on two-level cascaded signal amplification strategy. *Bioelectrochemistry*. 2014;96:7-13. doi:10.1016/j.bioelechem.2013.11.006.
136. Barthelmebs L, Hayat A, Limiadi AW, Marty JL, Noguer T. Electrochemical DNA aptamer-based biosensor for OTA detection, using superparamagnetic nanoparticles. *Sensors Actuators, B Chem*. 2011;156(2):932-937. doi:10.1016/j.snb.2011.03.008.
137. Mishra RK, Hayat A, Catanante G, Istamboulie G, Marty J-L. Sensitive quantitation of Ochratoxin A in cocoa beans using differential pulse voltammetry based aptasensor. *Food Chem*. 2016;192:799-804. doi:10.1016/j.foodchem.2015.07.080.
138. Galopin E, Noual A, Niedziółka-Jönsson J, Jönsson-Niedziółka M, Akjouj A, Pennec Y, Djafari-Rouhani B, Boukherroub R, Szunerits S. Short- and Long-Range Sensing Using Plasmonic Nanostrucures: Experimental and Theoretical Studies. *J Phys Chem C*. 2009;113(36):15921-15927. doi:10.1021/jp905154z.

139. Jane A, Dronov R, Hodges A, Voelcker NH. Porous silicon biosensors on the advance. *Trends Biotechnol*. 2009;27(4):230-239. doi:10.1016/j.tibtech.2008.12.004.
140. Liao W, Wei F, Qian MX, Zhao XS. Characterization of protein immobilization on alkyl monolayer modified silicon(1 1 1) surface. *Sensors Actuators, B Chem*. 2004;101(3):361-367. doi:10.1016/j.snb.2004.04.006.
141. Hsiao CY, Lin CH, Hung CH, Su CJ, Lo YR, Lee CC, Lin HC, Ko FH, Huang TY, Yang YS. Novel poly-silicon nanowire field effect transistor for biosensing application. *Biosens Bioelectron*. 2009;24(5):1223-1229. doi:10.1016/j.bios.2008.07.032.
142. Dhanekar S, Jain S. Porous silicon biosensor: Current status. *Biosens Bioelectron*. 2013;41(1):54-64. doi:10.1016/j.bios.2012.09.045.
143. Slowing II, Trewyn BG, Giri S, Lin VSY. Mesoporous Silica Nanoparticles for Drug Delivery and Biosensing Applications. *Adv Funct Mater*. 2007;17(8):1225-1236. doi:10.1002/adfm.200601191.
144. Urmann K, Walter J-G, Scheper T, Segal E. Label-Free Optical Biosensors Based on Aptamer-Functionalized Porous Silicon Scaffolds. *Anal Chem*. 2015;87(3):1999-2006. doi:10.1021/ac504487g.
145. Zheng G, Gao XPA, Lieber CM. Frequency Domain Detection of Biomolecules Using Silicon Nanowire Biosensors. *Nano Lett*. 2010;10(8):3179-3183. doi:10.1021/nl1020975.
146. Liu Y, Du Y, Li CM. Direct Electrochemistry Based Biosensors and Biofuel Cells Enabled with Nanostructured Materials. *Electroanalysis*. 2013;25(4):815-831. doi:10.1002/elan.201200555.
147. Pramanik S, Pingguan-Murphy B, Osman NAA. Developments of immobilized surface modified piezoelectric crystal biosensors for advanced applications. *Int J Electrochem Sci*. 2013;8(6):8863-8892.
148. Tamayo J, Kosaka PM, Ruz JJ, San Paulo Á, Calleja M. Biosensors based on nanomechanical systems. *Chem Soc Rev*. 2013;42(3):1287-1311. doi:10.1039/C2CS35293A.
149. Wasisto HS, Merzsch S, Waag A, Uhde E, Salthammer T, Peiner E. Airborne engineered nanoparticle mass sensor based on a silicon resonant cantilever. *Sensors Actuators B Chem*. 2013;180:77-89. doi:10.1016/j.snb.2012.04.003.
150. Wassum KM, Tolosa VM, Wang J, Walker E, Monbouquette HG, Maidment NT. Silicon wafer-based platinum microelectrode array biosensor for near real-time measurement of glutamate in vivo. *Sensors*. 2008;8(8):5023-5036. doi:10.3390/s8085023.
151. Effenberger F, Götz G, Bidlingmaier B, Wezstein M. Photoactivated Preparation and Patterning of Self-Assembled Monolayers with 1-Alkenes and Aldehydes on Silicon Hydride Surfaces. *Angew Chemie Int Ed*. 1998;37(18):2462-2464. doi:10.1002/(SICI)1521-3773(19981002)37:18<2462::AID-ANIE2462>3.0.CO;2-R.
152. Flavel BS, Jasieniak M, Velleman L, Ciampi S, Luais E, Peterson JR, Griesser HJ, Shapter JG, Gooding JJ. Grafting of Poly(ethylene glycol) on Click Chemistry Modified Si(100) Surfaces. *Langmuir*. 2013;29(26):8355-8362. doi:10.1021/la400721c.
153. Banerjee I, Pangule RC, Kane RS. Antifouling Coatings: Recent Developments in the Design of Surfaces That Prevent Fouling by Proteins, Bacteria, and Marine Organisms. *Adv Mater*. 2011;23(6):690-718. doi:10.1002/adma.201001215.
154. Gooding JJ, Ciampi S. The molecular level modification of surfaces: from self-

assembled monolayers to complex molecular assemblies. *Chem Soc Rev*. 2011;40(5):2704. doi:10.1039/c0cs00139b.

155. Hair ML, Hertl W. Reactions of chlorosilanes with silica surfaces. *J Phys Chem*. 1969;73(7):2372-2378. doi:10.1021/j100727a046.
156. Tian R, Seitz O, Li M, Hu W (Walter), Chabal YJ, Gao J. Infrared Characterization of Interfacial Si−O Bond Formation on Silanized Flat SiO 2 /Si Surfaces. *Langmuir*. 2010;26(7):4563-4566. doi:10.1021/la904597c.
157. Le Grange JD, Markham JL, Kurkjian CR. Effects of surface hydration on the deposition of silane monolayers on silica. *Langmuir*. 1993;9(7):1749-1753. doi:10.1021/la00031a023.
158. Hanson EL, Schwartz J, Nickel B, Koch N, Danisman MF. Bonding Self-Assembled, Compact Organophosphonate Monolayers to the Native Oxide Surface of Silicon. *J Am Chem Soc*. 2003;125(51):16074-16080. doi:10.1021/ja035956z.
159. Silverman BM, Wieghaus KA, Schwartz J. Comparative Properties of Siloxane vs Phosphonate Monolayers on A Key Titanium Alloy. *Langmuir*. 2005;21(1):225-228. doi:10.1021/la048227l.
160. Dubey M, Weidner T, Gamble LJ, Castner DG. Structure and Order of Phosphonic Acid-Based Self-Assembled Monolayers on Si(100). *Langmuir*. 2010;26(18):14747-14754. doi:10.1021/la1021438.
161. Vega A, Thissen P, Chabal YJ. Environment-Controlled Tethering by Aggregation and Growth of Phosphonic Acid Monolayers on Silicon Oxide. *Langmuir*. 2012;28(21):8046-8051. doi:10.1021/la300709n.
162. Bean KE. Anisotropic etching of silicon. *IEEE Trans Electron Devices*. 1978;25(10):1185-1193. doi:10.1109/T-ED.1978.19250.
163. Higashi GS, Chabal YJ, Trucks GW, Raghavachari K. Ideal hydrogen termination of the Si (111) surface. *Appl Phys Lett*. 1990;56(7):656. doi:10.1063/1.102728.
164. Niwano M, Kageyama J, Kurita K, Kinashi K, Takahashi I, Miyamoto N. Infrared spectroscopy study of initial stages of oxidation of hydrogen-terminated Si surfaces stored in air. *J Appl Phys*. 1994;76(4):2157. doi:10.1063/1.357627.
165. Higashi GS, Becker RS, Chabal YJ, Becker AJ. Comparison of Si(111) surfaces prepared using aqueous solutions of NH4F versus HF. *Appl Phys Lett*. 1991;58(15):1656. doi:10.1063/1.105155.
166. Uhlir A. Electrolytic Shaping of Germanium and Silicon. *Bell Syst Tech J*. 1956;35(2):333-347. doi:10.1002/j.1538-7305.1956.tb02385.x.
167. Lehmann V, Gösele U. Porous silicon formation: A quantum wire effect. *Appl Phys Lett*. 1991;58(8):856. doi:10.1063/1.104512.
168. Archer RJ. Stain films on silicon. *J Phys Chem Solids*. 1960;14:104-110. doi:10.1016/0022-3697(60)90215-8.
169. Ubara H, Imura T, Hiraki A. Formation of Si-H bonds on the surface of microcrystalline silicon covered with SiOx by HF treatment. *Solid State Commun*. 1984;50(7):673-675. doi:10.1016/0038-1098(84)90156-X.
170. Chabal YJ. Surface infrared spectroscopy. *Surf Sci Rep*. 1988;8(5-7):211-357. doi:10.1016/0167-5729(88)90011-8.
171. Thissen P, Seitz O, Chabal YJ. Wet chemical surface functionalization of oxide-free silicon. *Prog Surf Sci*. 2012;87(9-12):272-290. doi:10.1016/j.progsurf.2012.10.003.
172. Linford MR, Chidsey CED. Alkyl monolayers covalently bonded to silicon surfaces. *J Am Chem Soc*. 1993;115(26):12631-12632. doi:10.1021/ja00079a071.

173. Fidélis A, Ozanam F, Chazalviel J-N. Fully methylated, atomically flat (111) silicon surface. *Surf Sci*. 2000;444(1-3):L7-L10. doi:10.1016/S0039-6028(99)01065-1.
174. Fellah S, Boukherroub R, Ozanam F, Chazalviel J-N. Hidden Electrochemistry in the Thermal Grafting of Silicon Surfaces from Grignard Reagents. *Langmuir*. 2004;20(15):6359-6364. doi:10.1021/la049672j.
175. Pinson J, Podvorica F. Attachment of organic layers to conductive or semiconductive surfaces by reduction of diazonium salts. *Chem Soc Rev*. 2005;34(5):429. doi:10.1039/b406228k.
176. Wang D, Buriak JM. Electrochemically driven organic monolayer formation on silicon surfaces using alkylammonium and alkylphosphonium reagents. *Surf Sci*. 2005;590(2-3):154-161. doi:10.1016/j.susc.2005.06.018.
177. Linford MR, Fenter P, Eisenberger PM, Chidsey CED. Alkyl Monolayers on Silicon Prepared from 1-Alkenes and Hydrogen-Terminated Silicon. *J Am Chem Soc*. 1995;117(11):3145-3155. doi:10.1021/ja00116a019.
178. Cicero RL, Linford MR, Chidsey CED. Photoreactivity of Unsaturated Compounds with Hydrogen-Terminated Silicon(111). *Langmuir*. 2000;16(13):5688-5695. doi:10.1021/la9911990.
179. Sun Q-Y, de Smet LCPM, van Lagen B, Giesbers M, Thüne PC, van Engelenburg J, de Wolf FA, Zuilhof H, Sudhölter EJR. Covalently Attached Monolayers on Crystalline Hydrogen-Terminated Silicon: Extremely Mild Attachment by Visible Light. *J Am Chem Soc*. 2005;127(8):2514-2523. doi:10.1021/ja045359s.
180. Boukherroub R, Morin S, Bensebaa F, Wayner DDM. New Synthetic Routes to Alkyl Monolayers on the Si(111) Surface. *Langmuir*. 1999;15(11):3831-3835. doi:10.1021/la9901478.
181. Buriak JM, Allen MJ. Lewis Acid Mediated Functionalization of Porous Silicon with Substituted Alkenes and Alkynes. *J Am Chem Soc*. 1998;120(6):1339-1340. doi:10.1021/ja9740125.
182. Gouget-Laemmel AC, Yang J, Lodhi MA, Siriwardena A, Aureau D, Boukherroub R, Chazalviel J-N, Ozanam F, Szunerits S. Functionalization of Azide-Terminated Silicon Surfaces with Glycans Using Click Chemistry: XPS and FTIR Study. *J Phys Chem C*. 2013;117(1):368-375. doi:10.1021/jp309866d.
183. Staros J V., Wright RW, Swingle DM. Enhancement by N-hydroxysulfosuccinimide of water-soluble carbodiimide-mediated coupling reactions. *Anal Biochem*. 1986;156(1):220-222. doi:10.1016/0003-2697(86)90176-4.
184. Ciampi S, Harper JB, Gooding JJ. Wet chemical routes to the assembly of organic monolayers on silicon surfaces via the formation of Si–C bonds: surface preparation, passivation and functionalization. *Chem Soc Rev*. 2010;39(6):2158. doi:10.1039/b923890p.
185. Stewart MP, Buriak JM. Photopatterned Hydrosilylation on Porous Silicon. *Angew Chemie Int Ed*. 1998;37(23):3257-3260. doi:10.1002/(SICI)1521-3773(19981217)37:23<3257::AID-ANIE3257>3.0.CO;2-1.
186. Stewart MP, Buriak JM. Exciton-Mediated Hydrosilylation on Photoluminescent Nanocrystalline Silicon. *J Am Chem Soc*. 2001;123(32):7821-7830. doi:10.1021/ja011116d.
187. de Smet LCPM, Zuilhof H, Sudhölter EJR, Lie LH, Houlton A, Horrocks BR. Mechanism of the Hydrosilylation Reaction of Alkenes at Porous Silicon: Experimental and Computational Deuterium Labeling Studies. *J Phys Chem B*.

2005;109(24):12020-12031. doi:10.1021/jp044400a.

188. Cai W, Lin Z, Strother T, Smith LM, Hamers RJ. Chemical Modification and Patterning of Iodine-Terminated Silicon Surfaces Using Visible Light. *J Phys Chem B*. 2002;106(10):2656-2664. doi:10.1021/jp013523h.
189. Sun Q-Y, de Smet LCPM, van Lagen B, Wright A, Zuilhof H, Sudhölter EJR. Covalently Attached Monolayers on Hydrogen-Terminated Si(100): Extremely Mild Attachment by Visible Light. *Angew Chemie Int Ed*. 2004;43(11):1352-1355. doi:10.1002/anie.200352137.
190. de Smet LCPM, Pukin A V., Sun Q-Y, Eves BJ, Lopinski GP, Visser GM, Zuilhof H, Sudhölter EJR. Visible-light attachment of SiC linked functionalized organic monolayers on silicon surfaces. *Appl Surf Sci*. 2005;252(1):24-30. doi:10.1016/j.apsusc.2005.01.107.
191. Wang X, Ruther RE, Streifer JA, Hamers RJ. UV-Induced Grafting of Alkenes to Silicon Surfaces: Photoemission versus Excitons. *J Am Chem Soc*. 2010;132(12):4048-4049. doi:10.1021/ja910498z.
192. Wang X, Colavita PE, Streifer JA, Butler JE, Hamers RJ. Photochemical Grafting of Alkenes onto Carbon Surfaces: Identifying the Roles of Electrons and Holes. *J Phys Chem C*. 2010;114(9):4067-4074. doi:10.1021/jp911264n.
193. Sehgal D, Vijay IK. A Method for the High Efficiency of Water-Soluble Carbodiimide-Mediated Amidation. *Anal Biochem*. 1994;218(1):87-91. doi:10.1006/abio.1994.1144.
194. Carpino LA, Imazumi H, El-Faham A, Ferrer FJ, Zhang C, Lee Y, Foxman BM, Henklein P, Hanay C, Mügge C, Wenschuh H, Klose J, Beyermann M, Bienert M. The Uronium/Guanidinium Peptide Coupling Reagents: Finally the True Uronium Salts. *Angew Chemie Int Ed*. 2002;41(3):441-445. doi:10.1002/1521-3773(20020201)41:3<441::AID-ANIE441>3.0.CO;2-N.
195. Hiebl J, Baumgartner H, Bernwieser I, Blanka M, Bodenteich M, Leitner K, Rio A, Rovenszky F, Alberts DP, Bhatnagar PK, Banyard AF, Baresch K, Esch PM, Kollmann H, Mayrhofer G, Weihtrager H, Welz W, Winkler K, Chen T, Patel R, Lantos I, Stevenson D, Tubman KD, Undheim K. Large-scale synthesis of hematoregulatory nonapeptide SK&F 107647 by fragment coupling. *J Pept Res*. 1999;54(1):54-65. doi:10.1034/j.1399-3011.1999.00089.x.
196. Castro B, Dormoy JR, Evin G, Selve C. Reactifs de couplage peptidique I (1) - l'hexafluorophosphate de benzotriazolyl N-oxytrisdimethylamino phosphonium (B.O.P.). *Tetrahedron Lett*. 1975;16(14):1219-1222. doi:10.1016/S0040-4039(00)72100-9.
197. Castro B, Dormoy J-R, Dourtoglou B, Evin G, Selve C, Ziegler J-C. Peptide Coupling Reagents VI 1 . A Novel, Cheaper Preparation of Benzotriazolyloxytris[dimethylamino]phosphonium Hexafluorophosphate (BOP Reagent). *Synthesis (Stuttg)*. 1976;1976(11):751-752. doi:10.1055/s-1976-24189.
198. Valeur E, Bradley M. Amide bond formation: beyond the myth of coupling reagents. *Chem Soc Rev*. 2009;38(2):606-631. doi:10.1039/B701677H.
199. Han S-Y, Kim Y-A. Recent development of peptide coupling reagents in organic synthesis. *Tetrahedron*. 2004;60(11):2447-2467. doi:10.1016/j.tet.2004.01.020.
200. Khorana HG. The Chemistry of Carbodiimides. *Chem Rev*. 1953;53(2):145-166. doi:10.1021/cr60165a001.
201. Kurzer F, Douraghi-Zadeh K. Advances in the Chemistry of Carbodiimides. *Chem Rev*. 1967;67(2):107-152. doi:10.1021/cr60246a001.

202. Nakajima N, Ikada Y. Mechanism of Amide Formation by Carbodiimide for Bioconjugation in Aqueous Media. *Bioconjug Chem*. 1995;6(1):123-130. doi:10.1021/bc00031a015.
203. Touahir L, Chazalviel J-N, Sam S, Moraillon A, Henry de Villeneuve C, Allongue P, Ozanam F, Gouget-Laemmel a. C. Kinetics of Activation of Carboxyls to Succinimidyl Ester Groups in Monolayers Grafted on Silicon: An in Situ Real-Time Infrared Spectroscopy Study. *J Phys Chem C*. 2011;115(14):6782-6787. doi:10.1021/jp200150m.
204. Perez E, Lahlil K, Rougeau C, Moraillon A, Chazalviel J-N, Ozanam F, Gouget-Laemmel AC. Influence of the Molecular Design on the Antifouling Performance of Poly(ethylene glycol) Monolayers Grafted on (111) Si. *Langmuir*. 2012;28(41):14654-14664. doi:10.1021/la303022a.
205. Moraillon A, Gouget-Laemmel AC, Ozanam F, Chazalviel J-N. -Amidation of Monolayers on Silicon in Physiological Buffers: A Quantitative IR Study - Supporting Info. *J Phys Chem C*. 2008;112(18):7158-7167. doi:10.1021/jp7119922.
206. Anderson AS, Dattelbaum AM, Montano G a., Price DN, Schmidt JG, Martinez JS, Grace WK, Grace KM, Swanson BI. Functional PEG-modified thin films for biological detection. *Langmuir*. 2008;24(5):2240-2247. doi:10.1021/la7033438.
207. Kingshott P, Griesser HJ. Surfaces that resist bioadhesion. *Curr Opin Solid State Mater Sci*. 1999;4(4):403-412. doi:10.1016/S1359-0286(99)00018-2.
208. Yan X, Sivignon A, Yamakawa N, Crepet A, Travelet C, Borsali R, Dumych T, Li Z, Bilyy R, Deniaud D, Fleury E, Barnich N, Darfeuille-Michaud A, Gouin SG, Bouckaert J, Bernard J. Glycopolymers as antiadhesives of E. coli strains inducing inflammatory bowel diseases. *Biomacromolecules*. 2015;16(6):1827-1836. doi:10.1021/acs.biomac.5b00413.
209. Lambert JB, Marsmann H, Gronert S, Shurvell HF, Lightner DA. *Spektroskopie - Strukturaufklärung in Der Organischen Chemie*. 2nd ed. Pearson, Higher Education; 2012.
210. Queeney KT, Weldon MK, Chang JP, Chabal YJ, Gurevich a. B, Sapjeta J, Opila RL. Infrared spectroscopic analysis of the Si/SiO[sub 2] interface structure of thermally oxidized silicon. *J Appl Phys*. 2000;87(3):1322. doi:10.1063/1.372017.
211. Ohwaki T, Takeda M, Takai Y. Characterization of silicon native oxide formed in SC-1, H2O2 and wet ozone processes. *Japanese J Appl Physics, Part 1 Regul Pap Short Notes Rev Pap*. 1997;36(9 A):5507-5513.
212. Beckmann KH. Investigation of the chemical properties of stain films on silicon by means of infrared spectroscopy. *Surf Sci*. 1965;3(4):314-332. doi:10.1016/0039-6028(65)90002-6.
213. Sieval AB, van den Hout B, Zuilhof H, Sudhölter EJR. Molecular Modeling of Covalently Attached Alkyl Monolayers on the Hydrogen-Terminated Si(111) Surface. *Langmuir*. 2001;17(7):2172-2181. doi:10.1021/la001494g.
214. Xiao S-J, Brunner S, Wieland M. Reactions of Surface Amines with Heterobifunctional Cross-Linkers Bearing Both Succinimidyl Ester and Maleimide for Grafting Biomolecules. *J Phys Chem B*. 2004;108(42):16508-16517. doi:10.1021/jp047726s.
215. Tozlovanu M, Pfohl-Leszkowicz A. Ochratoxin A in roasted coffee from French supermarkets and transfer in coffee beverages: Comparison of analysis methods. *Toxins (Basel)*. 2010;2(8):1928-1942. doi:10.3390/toxins2081928.

216. Bazin I, Faucet-Marquis V, Monje MC, El Khoury M, Marty JL, Pfohl-Leszkowicz A. Impact of pH on the stability and the cross-reactivity of ochratoxin A and citrinin. *Toxins (Basel)*. 2013;5(12):2324-2340. doi:10.3390/toxins5122324.
217. Frenette C, Paugh RJ, Tozlovanu M, Juzio M, Pfohl-Leszkowicz A, Manderville RA. Structure–activity relationships for the fluorescence of ochratoxin A: Insight for detection of ochratoxin A metabolites. *Anal Chim Acta*. 2008;617(1-2):153-161. doi:10.1016/j.aca.2007.12.030.
218. Pfohl-Leszkowicz A, Manderville RA. Ochratoxin A: An overview on toxicity and carcinogenicity in animals and humans. *Mol Nutr Food Res*. 2007;51(1):61-99. doi:10.1002/mnfr.200600137.
219. el Khoury A, Atoui A. Ochratoxin A: General Overview and Actual Molecular Status. *Toxins (Basel)*. 2010;2(4):461-493. doi:10.3390/toxins2040461.
220. Zezza F, Longobardi F, Pascale M, Eremin S a., Visconti A. Fluorescence polarization immunoassay for rapid screening of ochratoxin A in red wine. *Anal Bioanal Chem*. 2009;395(5):1317-1323. doi:10.1007/s00216-009-2994-3.
221. Bredenkamp MW, Dillen JLM, van Rooyen PH, Steyn PS. Crystal structures and conformational analysis of ochratoxin A and B: probing the chemical structure causing toxicity. *J Chem Soc Perkin Trans 2*. 1989;1(11):1835. doi:10.1039/p29890001835.
222. Zhao Q, Geng X, Wang H. Fluorescent sensing ochratoxin A with single fluorophore-labeled aptamer. *Anal Bioanal Chem*. 2013;405(19):6281-6286. doi:10.1007/s00216-013-7047-2.
223. McKeague M, Velu R, Hill K, Bardóczy V, Mészáros T, DeRosa MC. Selection and characterization of a novel DNA aptamer for label-free fluorescence biosensing of ochratoxin A. *Toxins (Basel)*. 2014;6(8):2435-2452. doi:10.3390/toxins6082435.
224. Yang C, Lates V, Prieto-Simón B, Marty J-L, Yang X. Aptamer-DNAzyme hairpins for biosensing of Ochratoxin A. *Biosens Bioelectron*. 2012;32(1):208-212. doi:10.1016/j.bios.2011.12.011.
225. Cruz-Aguado J a., Penner G. Fluorescence Polarization Based Displacement Assay for the Determination of Small Molecules with Aptamers. *Anal Chem*. 2008;80(22):8853-8855. doi:10.1021/ac8017058.
226. Chen J, Zhang X, Cai S, Wu D, Chen M, Wang S, Zhang J. A fluorescent aptasensor based on DNA-scaffolded silver-nanocluster for ochratoxin A detection. *Biosens Bioelectron*. 2014;57:226-231. doi:10.1016/j.bios.2014.02.001.
227. Gabriel CM, Keener M, Gallou F, Lipshutz BH. Amide and Peptide Bond Formation in Water at Room Temperature. *Org Lett*. 2015;17(16):3968-3971. doi:10.1021/acs.orglett.5b01812.
228. Schott. *Protocol NEXTERION Slide H DNA Application*. http://www.schott.com/nexterion/english/download/protocol_slide_h_dna_3_0.pdf.
229. Hayat A, Sassolas A, Marty J-L, Radi A-E. Highly sensitive ochratoxin A impedimetric aptasensor based on the immobilization of azido-aptamer onto electrografted binary film via click chemistry. *Talanta*. 2013;103:14-19. doi:10.1016/j.talanta.2012.09.048.
230. Meneghello A, Sosic A, Antognoli A, Cretaio E, Gatto B. Development and Optimization of a Thrombin Sandwich Aptamer Microarray. *Microarrays*. 2012;1(3):95-106. doi:10.3390/microarrays1020095.

231. Taboury JA, Liquier J, Taillandier E. Characterization of DNA structures by infrared spectroscopy: double helical forms of poly(dG-dC)•poly(dG-dC), poly(dD 8 G-dC)•poly(dD 8 G-dC), and poly(dG-dm 5 C)•poly(dG-dm 5 C). *Can J Chem*. 1985;63(7):1904-1909. doi:10.1139/v85-315.
232. Mao Y, Daniel LN, Whittaker N, Saffiotti U. DNA binding to crystalline silica characterized by Fourier-transform infrared spectroscopy. *Environ Health Perspect*. 1994;102(Suppl 10):165-171. doi:10.1289/ehp.94102s10165.
233. Venta K, Shemer G, Puster M, Rodríguez-Manzo JA, Balan A, Rosenstein JK, Shepard K, Drndić M. Differentiation of Short, Single-Stranded DNA Homopolymers in Solid-State Nanopores. *ACS Nano*. 2013;7(5):4629-4636. doi:10.1021/nn4014388.
234. Marsh TC, Vesenka J, Henderson E. A new DNA nanostructure, the G-wire, imaged by scanning probe microscopy. *Nucleic Acids Res*. 1995;23(4):696-700. doi:10.1093/nar/23.4.696.
235. Mergny J-L, Phan A-T, Lacroix L. Following G-quartet formation by UV-spectroscopy. *FEBS Lett*. 1998;435(1):74-78. doi:10.1016/S0014-5793(98)01043-6.
236. Burge S, Parkinson GN, Hazel P, Todd AK, Neidle S. Quadruplex DNA: sequence, topology and structure. *Nucleic Acids Res*. 2006;34(19):5402-5415. doi:10.1093/nar/gkl655.
237. IR Warfarin NIST. http://webbook.nist.gov/cgi/inchi?ID=C81812&Type=IR-SPEC&Index=1#IR-SPEC.
238. Zhang J, Zhang X, Yang G, Chen J, Wang S. A signal-on fluorescent aptasensor based on Tb3+ and structure-switching aptamer for label-free detection of Ochratoxin A in wheat. *Biosens Bioelectron*. 2013;41:704-709. doi:10.1016/j.bios.2012.09.053.
239. Kuang H, Chen W, Xu D, Xu L, Zhu Y, Liu L, Chu H, Peng C, Xu C, Zhu S. Fabricated aptamer-based electrochemical “signal-off” sensor of ochratoxin A. *Biosens Bioelectron*. 2010;26(2):710-716. doi:10.1016/j.bios.2010.06.058.
240. Lv Z, Chen A, Liu J, Guan Z, Zhou Y, Xu S, Yang S, Li C. A Simple and Sensitive Approach for Ochratoxin A Detection Using a Label-Free Fluorescent Aptasensor. Antopolsky M, ed. *PLoS One*. 2014;9(1):e85968. doi:10.1371/journal.pone.0085968.
241. Solomon I, Schmidt MP, Tran-Quoc H. Selective low-power plasma decomposition of silane-methane mixtures for the preparation of methylated amorphous silicon. *Phys Rev B*. 1988;38(14):9895-9901. doi:10.1103/PhysRevB.38.9895.
242. Rubin M. Optical properties of soda lime silica glasses. *Sol Energy Mater*. 1985;12(4):275-288. doi:10.1016/0165-1633(85)90052-8.
243. Heavens OS. *Optical Properties of Thin Solid Films*. Dover Publications; 1955.
244. Eisen MB, Brown PO. DNA arrays for analysis of gene expression. In: *Methods in Enzymology*. Vol 303. ; 1999:179-205. doi:10.1016/S0076-6879(99)03014-1.
245. Fare TL, Coffey EM, Dai H, He YD, Kessler D a., Kilian K a., Koch JE, LeProust E, Marton MJ, Meyer MR, Stoughton RB, Tokiwa GY, Wang Y. Effects of Atmospheric Ozone on Microarray Data Quality. *Anal Chem*. 2003;75(17):4672-4675. doi:10.1021/ac034241b.
246. Rhouati A, Yang C, Hayat A, Marty J-L. Aptamers: A Promosing Tool for Ochratoxin A Detection in Food Analysis. *Toxins (Basel)*. 2013;5(11):1988-2008.

doi:10.3390/toxins5111988.

247. Chazalviel J-N, Fellah S, Ozanam F. In situ infrared spectroscopy: a powerful technique for semiconducting electrodes. *J Electroanal Chem*. 2002;524-525:137-143. doi:10.1016/S0022-0728(01)00741-0.
248. Reimer L. *Scanning Electron Microscopy*. Vol 45. Berlin, Heidelberg: Springer Berlin Heidelberg; 1998. doi:10.1007/978-3-540-38967-5.
249. Goldstein JI, Newbury DE, Echlin P, Joy DC, Lyman CE, Lifshin E, Sawyer L, Michael JR. *Scanning Electron Microscopy and X-Ray Microanalysis*. Boston, MA: Springer US; 2003. doi:10.1007/978-1-4615-0215-9.
250. Biorobotics MicroGrid II. http://www.nature.com/nbt/journal/v19/n1/full/nbt0101_89.html. Accessed September 20, 2016.

Titre: Biocapteurs sur silicium pour la détection des interactions aptamères / agents pathogènes.

La détection rapide et sensible des agents pathogènes est d'une très grande importance pour la biosécurité. Les biopuces sont bien adaptées à cet effet, car elles permettent la détection multiplexe des cibles. Une limitation cruciale des biopuces est leur manque de fiabilité et de sensibilité. L'objectif de cette thèse est de développer une architecture reproductible de biopuces à base de couche mince de silicium amorphe carboné (a-SiC:H) déposée sur un réflecteur en aluminium pour une détection fiable et sensible des pathogènes. Nous avons choisi comme système modèle l'interaction de la toxine alimentaire ochratoxine A (OTA) avec son aptamère AntiOTA de longueur 36mer. Les aptamères (simples brins d'ADN) sont de plus en plus utilisés comme sondes en raison de leur grande spécificité et affinité vis-à-vis d'une large gamme de cibles (i.e. protéines, bactéries…). La stratégie de fabrication consiste en un greffage de monocouches organiques d'acides carboxyliques via des liaisons Si-C robustes, suivi de l'accrochage covalent des aptamères par un couplage peptidique. Les processus de greffage ont été mis au point sur silicium cristallin permettant la quantification des couches greffées par spectroscopie infrarouge en mode ATR (Attenuated total reflexion). La quantification IR des interactions OTA – AntiOTA a été montrée pour la première fois sur des surfaces par IR-ATR. La spécificité de l'aptamère a été démontrée en utilisant une molécule chimiquement similaire (warfarin), pour laquelle l'AntiOTA ne montre aucune affinité. Ces protocoles bien contrôlés ont été transférés sur l'architecture de la biopuce a-SiC:H. Les aptamères immobilisés sont hybridés avec des brins complémentaires marqués avec des fluorophores. En présence de l'OTA une déshybridation des brins complémentaires est attendue, conduisant à une diminution du signal fluorescent. Différentes longueurs de brins complémentaires ont été comparées, montrant jusqu'à 13% de diminution due à l'interaction de l'OTA.

Mots-clés: biopuce, aptamère, pathogène, ochratoxine A, hydrosilylation, fluorescence, IR-ATR

Title: Biochips based on silicon for detecting the interaction between aptamers and pathogens.

Rapid and sensitive detection of pathogenic targets play a crucial role in biosecurity. Biochips are ideal for this, as they allow easy and multiplex detection of targets. A crucial limitation in biochips is that they often suffer from low reliability and sensitivity. The goal of this thesis is to develop a stable and reproducible architecture for biochips based on an amorphous silicon carbon alloy (a-SiC:H) deposited on an aluminium back-reflector for reliable and sensitive detection of pathogens. On these biochips we introduced the interaction of the food and feed toxin ochratoxin A (OTA) with its 36mer aptamer AntiOTA as a model system. Aptamers (single strands of DNA) are ideal as probes for biochips as they display high specificity and affinity towards a wide range of targets (i.e. proteins, bacteria…). The well-controlled multi-step fabrication process consists of the reliable photochemical grafting of acid-terminated organic monolayers on silicon surfaces by robust Si-C bonds, which in turn were functionalized with aptamers by stable peptide coupling. Carrying out this process on crystalline silicon allowed monitoring and quantification of every step by infrared spectroscopy (IR-ATR). The interaction OTA – AntiOTA was shown for the first time on surfaces by IR, and an IR *in situ* calibration allowed the quantification of OTA which was bound by the aptamers on the surface. The specificity of AntiOTA towards OTA was demonstrated by using a chemically similar molecule (warfarin), for which AntiOTA shows no affinity. The well-controlled protocols were transferred to the a-SiC:H biochip. The immobilized aptamers were hybridized with complementary and fluorescent-labeled DNA-strands. In presence of OTA, dehybridization of the complementary strands is expected, resulting in a decrease of fluorescent signal. Different lengths of complementary strands were compared, exhibiting up to 13% signal decrease due to OTA.

Keywords: biochip, aptamer, pathogen, ochratoxin A, hydrosilylation, fluorescence, IR-ATR